DEVELOPMENT OF WRINKLED THIN FILM DEVICES FOR STRETCHABLE ELECTRONICS

DEVELOPMENT OF WRINKLED THIN FILM DEVICES FOR STRETCHABLE ELECTRONICS

By

Xiuping Ding, M. Eng.

A Thesis

Submitted to the School of Graduate Studies in Partial Fulfillment of the Requirements

for the Degree

Doctor of Philosophy in Chemistry

McMaster University

DOCTOR OF PHILOSOPHY (2022) MCMASTER UNIVERSITY

(Chemistry) Hamilton, Ontario

TITLE	Development of wrinkled thin films devices for stretchable electronics
AUTHOR:	Xiuping Ding, M. Eng. (University of Science and Technology Beijing, China)
SUPERVISOR:	Dr. Jose M. Moran-Mirabal
Number of pages:	x, 112

Abstract

Stretchable electronics are soft and light weight. Compared with conventional wafer-based electronics, which are rigid and planar, stretchable electronics can conform to curved surfaces and movable parts. The unique properties of stretchable electronics enable their integration with the human body, and open the door for ever more compelling applications, such as advanced surgical tools, wearable monitoring electronics, implantable prosthesis, and many others. However, the development of stretchable electronics is still at an early stage since their mechanical robustness and electrical performance are still far from satisfying.

In this work, I have developed a method to fabricate thin film stretchable devices by solvent-assisted transfer of wrinkled thin films from rigid polystyrene (PS) substrates to elastomeric polydimethylsiloxane (PDMS) substrates. Using this approach, structured thin films containing multiple materials and hybrid structures could be lifted off simultaneously, facilitating the fabrication of stretchable thin film devices. With this approach, I have built corrosion-resistant stretchable electrodes, stretchable thin film heaters, and stretchable thin film inductors. These applications demonstrate the simplicity and effectiveness of this stretchable electronics fabrication strategy. Finally, I made the first step towards fabricating dye-sensitized solar cells (DSSCs) with room temperature processes, including the preparation of mesoporous TiO_2 layers through mechanical compression and the integration of an interdigitated electrode that was fabricated solely by bench-top patterning, alignment, and sputtering deposition. These steps lay the foundation for the future development of stretchable DSSC. I anticipate that the fabricated stretchable thin films electronic components will contribute to the advancement of wearable and implantable electronics.

Lay Abstract

Electronics that can be deformed and conform to the irregular surfaces are attractive because they can be better integrated with the human body. For example, they could improve disease diagnostics and therapeutic treatments by providing wearable continuous monitoring devices and more advanced surgical tools. In this work, I created wrinkled thin films that could be affixed onto an elastic substrate and stretched. The principle of operation of these wrinkled devices mimics the way that the wrinkled skin on our knuckles and elbows allows us to bend our fingers and elbows. This approach makes wrinkled thin films stretchable and could lead to robust electronic devices. I have showcased this approach building a corrosion-resistant stretchable electrode, thin films heaters that can closely conform to joints, and a spiral-shaped inductor that could be used to wirelessly transfer data or power wearable devices. I believe that this work will contribute to the development of electronics that can be worn or implanted in the human body.

Acknowledgements

I cannot believe that I almost finish my PhD. I cannot help but to thank my supervisor Dr. Jose Moran-Mirabal for mentoring and working with me along the long, hard, yet beautiful journey. I appreciate the professionalism and support that he has been showing as a supervisor from the beginning to the end. He also leads a delightful group for encouraging us to be confident as an individual but be helpful to others in the group. I would like to take this chance to express my gratitude to my committee members Dr. Adrian Kitai and Dr. Gillian Goward, for they are having been patiently and kindly advised my research and helped me to get better. I took a course Dr. Adrian Kitai taught and he has struck me as a real scholar with kindness and knowledge even since. Dr. Gillian Goward not only impresses me with her excellent research, but also her effort for raising the awareness of being inclusive in science and beyond. They are all my role model in many ways.

As an international student, I have been benefiting for being in a supportive and friendly group with many excellent colleagues of undergrads and grads, of whom the humor, uplifting spirit and ambitiousness always make the everyday life fun. I would like to thank Peter for being my most delightful friend, Markus for being my most versatile friend, Ayo for being my most grounded friend and Kevin for being my most capable friend. I will not forget to thank Taylor, who are caring and inspires me to make a difference by acting for what you truly believe. I certainly remember to thank Dr. Babi, with whom most of my PhD was overlapped, for being much smarter than me, otherwise, there is no way that he seems always solve the puzzle and confusion for me with words of wisdom.

I cannot imagine what my PhD would look like without my valuable and excellent friends outside my lab. I would like to thank Juan and tell her that I have been missing all the most appetizing baking goods and delicious meals she prepared since she moved back to China. I want to thank Hao, who is always willing to help me out and be a gentleman. Thanks, Maggie, for our inefficient but fun coffee shop writing (haha), as

well as numerous hangouts. Also, I would like to thank Ethan (and Yujie) for not only made delicious barbecue but also helps me to characterize my devices. I also want to thank some nice guy named Alex at our neighboring lab, for rarely say no to my request for help. Thanks, some nice girl who named Dawn, for our friendship which comes so much easily to understand each other. Finally, thank you for Yujie (Oops, again, just hangout too much) and Fei, for the fun and endless talking we had.

I want to thank my sweet friends back home and beloved families. To my friends: thanks for always backing me up. To my beautiful cousin, Xianjuan: thanks for always being the supportive and sweet cousin. To my dear sister, Xiulan: thanks for accompanying our mum and dad, making me less guilty for being away from them. To my mom and dad: thanks for being so brave in front of hardships, being passionate for what you love, and being my mum and dad.

Table of Content

Abbreviations

AgNWs	silver nanowires
DSSCs	dye-sensitized solar cells
FTO	fluorine tin oxide
ITO	indium tin oxide
PEDOT: PSS	poly(3,4-ethylenedioxythiophene) doped with poly(styrenesulfonate)
SEM	scanning electron microscope
MPTMS	(3-mercaptopropyl)trimethoxysilane
NFC	near filed communication
PDMS	polydimethylsiloxane
PS	polystyrene
RFID	radio-frequency identification
SMP	shape memory polymer
SRF	self-resonance frequency

Mathematical Constants & Symbols

A	area
C_p	parasitic capacitance
ε	applied strain
FF	fill factor
f_0	resonance frequency
f_{sr}	self-resonance frequency
I	current
L	inductance
l	length of inductor
N	numbers of turn of inductor
ρ	electrical resistivity
Q	quality factor
R	resistance
R_s	sheet resistance
ΔR	resistance change
s	adjacent probe spacing
μ	permeability
σ	electrical conductivity
V	voltage
V_{oc}	open voltage
ω	angular frequency
T_f	fixing temperature
T_g	glass transition temperature
η	solar energy conversion efficiency
J_{sc}	short circuit current density

Chapter 1
Introduction

The development of stretchable electronics represents an emerging research direction, which focuses on overcoming the developing materials and devices that can adapt to the curved and soft biology and conform to the demands of movement stretch[1]. Stretchable electronics can reliably maintain high levels of performances while conforming to curved surfaces and integrating with the human body, which could not be achieved by conventional wafer-based technologies. Serious challenges on material science, sensing devices, signal/data processing and applications must be resolved for developing and eventually commercializing stretchable electronics. This thesis will only focus on materials science fabrication of film devices, and more specifically on the mechanical stretchability of patterned thin film electronics.

1.1. Motivation for stretchable electronics development

The desired characteristics for stretchable electronics include being light weight, conformal to curved surfaces, able to change reversibly under applied external stimuli, while maintaining a performance and reliability that matches or supersedes that of well-developed wafer-based systems[1]. The source of external stimuli could range from mechanical forces, such as stretching and compression[2,3], gas pressure[4,5]. to electric field[6,7], among others. Different from the ongoing research that develops smaller and faster devices on the rigid and planar silicon wafer, the research on stretchable electronics has focused more on mechanical property of materials and architectures, integration of components, devices and circuits[8]. Stretchable electronics enable the applications that are hard or impossible to achieve with existing hard and planar integrated circuits. The emerging applications include electronic skin, health monitor

interfaces, advanced and minimally invasive surgical and diagnostic tools, bio-inspired prosthesis, optogenetics and wearable communication devices.

1.2. Fabrication of stretchable electronics

Two conceptually different but complementary approaches have been used to develop stretchable electronics. These can be summarised as "new materials in conventional layouts" and "new structural layouts using conventional materials", respectively. This thesis involves the use of wrinkled conductive films to fabricate conductive elements or stretchable electronics. Therefore, the topic of my work can be categorized as new structural layouts using conventional materials.

1.2.1. New materials in conventional layouts

Most of the literature addressing new conductive materials that are under development for building stretchable electronics refers to intrinsically stretchable materials and composites. Compared with stretchable electronics that are fabricated with rigid components, stretchable electronics made from new stretchable materials have inherent advantages of simple fabrication processes, low cost and intrinsically large mechanical deformability[9]. Here, the new developed materials will be introduced with two major groups, intrinsic conductors, and composite conductors. Intrinsic stretchable conductors include liquid metals, ionic conductors and conducting polymers, while composite inductors are typically achieved by introducing conductive materials, also called conductive fillers, into elastomers.

Intrinsic conductors

Liquid metals. Liquid metals are highly stretchable and conductive but face major challenges on patterning owing to their high ability of flowing[10,11]. Gallium and gallium-based liquid-metal alloys have the combined properties of high electrical conductivity and low toxicity, making them attractive for stretchable electronics. A

stretchable light emitting diode connected with gold-gallium biphasic liquid metal has been reported on an elastomer (Figure 1.1A).

Conducting polymer. Polymer (schematic of the composition is shown inFigure1.1B) based stretchable conductors, derived from molecule-level robust materials, have demonstrated advantages in the fabrication of stretchable electronics that require smooth interfaces. Due to their ability to transport ions and electrons, which decreases

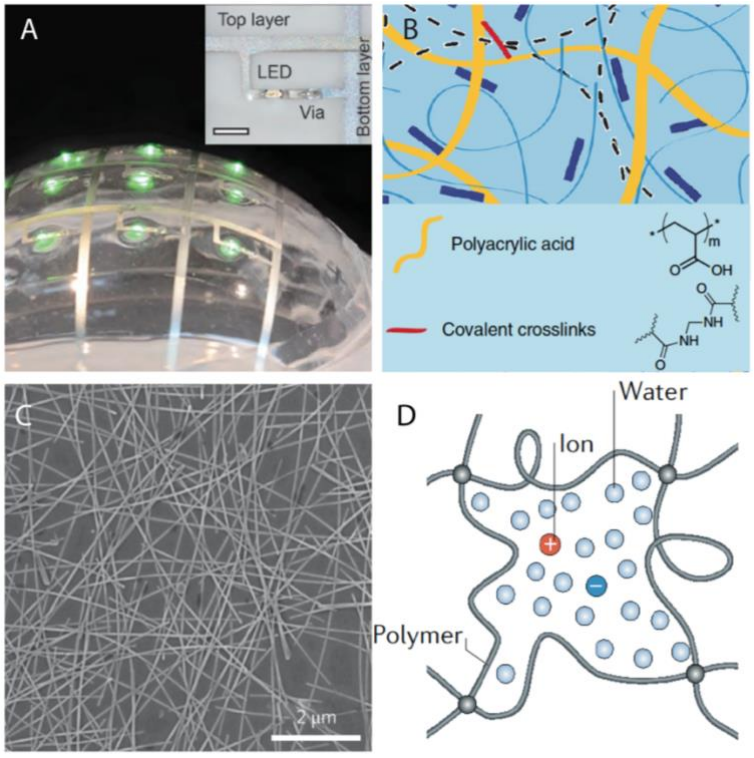

Figure 1.1. Intrinsically conductive materials for stretchable electronics. (**A**) Stretchable light emitting diodes interconnected through biphasic gold-gallium liquid metal conductors. Adapted with permission from reference [12]. Copyright 2016 John Wiley and Sons. (**B**) Compositional illustration for a conducting polymer PEDOT: PSS. Adapted by permission from: Springer Nature, reference [13]. Copyright 2018. (**C**) Scanning electron microscope (SEM) image for AgNWs coating on a glass substrate. Adapted by permission from: Springer Nature, reference [14]. Copyright 2013. (**D**) Schematic for a conductive hydrogel made of polymer networks and ions. Adapted by permission from: Springer Nature, reference [15]. Copyright 2018.

the interfacial impedance, conducting polymers have become a good choice as the interfacial media between electron-transport materials and ion-transport materials. This property can be beneficial for applications targeting biological systems in electrophysiology[16]. For example, poly(3,4-ethylenedioxythiophene) doped with

poly(styrenesulfonate) (PEDOT: PSS) has been used as interface material for recording the potentials from superficial cortical neurons without penetrating the brain surface[17]. However, conducting polymers tend to suffer degradation over time owing to their sensitivity to the environmental conditions[18]. Another challenge is that the performance of devices using conducting polymers is not yet comparable with that of their inorganic counterparts[19].

Hydrogel ionic conductor. Hydrogel ionic stretchable conductor shows exceptional stretchability and transparency while maintaining a minimum change in conductance in response to strain[20]. Many hydrogels, which contain polymer networks and water molecules (Figure 1.1D), are biocompatible and conform easily to living tissues[15]. Hydrogel conductors have been shown to have good potential for the use in highly deformable actuators[20], electroluminescent skin for optical signaling, and tactile sensing[21]. However, hydrogel ionic conductors particularly suffer from issues of bonding with other components and are susceptible to evaporation of the aqueous component[11] because of the high amount of water and sealing challenge.

Composite conductors

Conductive fillers that have attracted significant attention include single-walled carbon nanotubes[22], silver nanowires (AgNWs)[14] (Figure 1.1C), Ag flakes[23,24], and metallic nanoparticles[25]. The resultant conductivity closely relies on the percolation of the conducting fillers. High concentrations of conductive fillers contributes to higher conductivity, but also leads to lower elastic moduli[26]. Therefore, there is a trade-off between conductivity and stretchability for composite conductors. Although high conductivity and stretchability have been demonstrated, composite conductors also suffer from low patterning resolution[9].

1.2.2. New structural layouts with conventional materials

The strategy of exploiting new materials mentioned above could offer solutions for building stretchable electronics, but they either remain at the early stages of development or provide moderate performance, with uncertain reliability and low capacity of integration[27]. An alternative strategy, that of engineering the structure of conventional rigid electronic materials, has demonstrated high electrical performance

and integration capacity, benefitting from the rich history of development for silicon-wafer technology[19]. So far, the emerging structure-based engineering strategies include building rigid device islands linked by stretchable interconnects, serpentine patterns, slits or microcracks, and wrinkles or buckling.

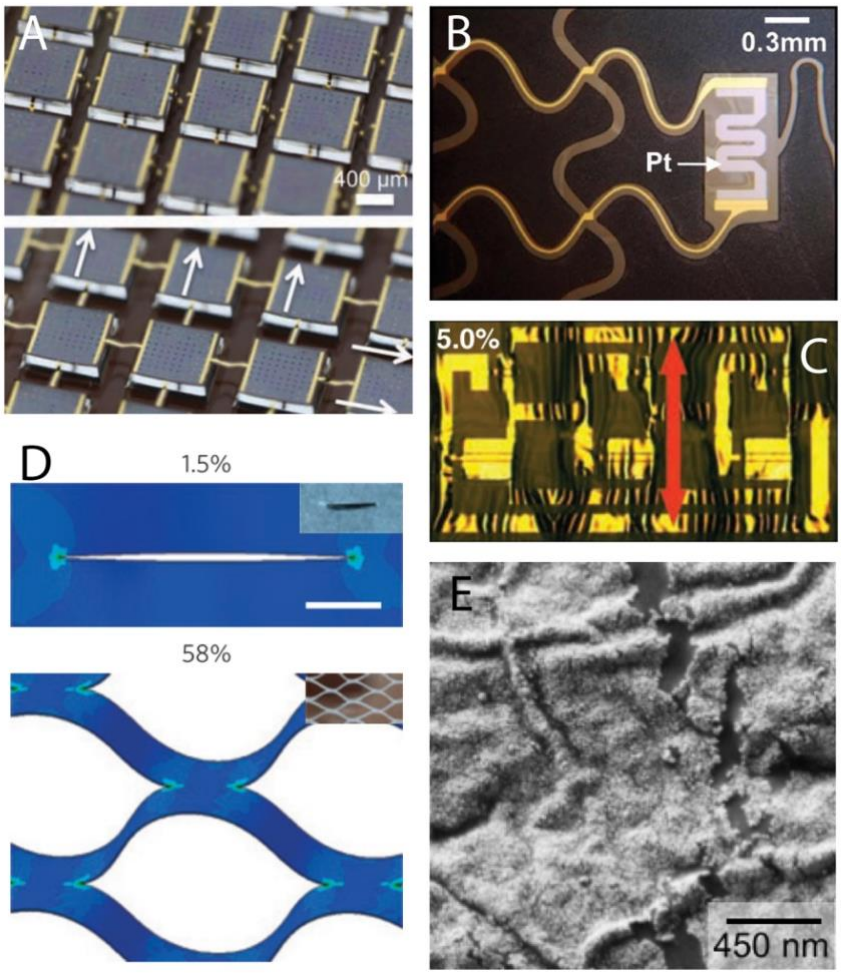

Figure 1.2. Strategies to structure conventional rigid materials for stretchable electronics. (**A**) Stretchable GaAs photovoltaic modules made of cells (rigid island) and connected with buckled interconnects. Adapted with permission from reference [28]. Copyright 2011 John Wiley and Sons. (**B**) Optical micrograph of a temperature sensor made of Pt with serpentine layout and interconnects with filament serpentine layout. From reference [29]. Adapted with permission from AAAS. (**C**) Optical micrograph of a wavy oscillator under 5% strain oriented along the direction of the red arrow. From reference [30]. Adapted with permission from AAAS. (**D**) Schematic illustration of how a kirigami patterned design changes under applied strain. Adapted by permission from: Springer Nature reference [31]. Copyright 2015. (**E**) A SEM image of gold film on PDMS with micro-scale cracks under 30% strain. Adapted with permission from reference [32]. Copyright 2019 American Chemical Society.

Out-of-plane island layout. The stretchable island layout (Figure 1.2A), where rigid active devices or elements are bridged by stretchable interconnects, has the

advantages of simple design and being applicable to most of the emerging stretchable devices[28]. The interconnects are buckled by pre-straining the elastomeric substrate, patterning and releasing the strain. The stretchability of the device can be improved by increasing the pre-strain and by the design of the serpentine configuration of the interconnections. A ring of oscillators fabricated with this method showed resilience up to 70% strain[33]. This system could withstand complex deformations, such as stretching, shearing and twisting. However, the interconnects could experience substantially increased strains near the edges of the device islands, which would lead to failure of the system.

In-plane serpentine layout. An in-plane serpentine layout has been exploited to increase the stretchability of intrinsically rigid materials (Figure 1.2B). This approach is highly compatible with conventional flexible printed circuit board technology and can achieve exceptional conformal contact with tissue or skin. Research shows that optimization of the geometry of gold wires embedded in a polydimethylsiloxane (PDMS) substrate can improve the stretchability to 54% compared to straight gold wires, which fail at the strain of 2.4 ± 2.5 %[34]. Geometry parameters such as a sinusoidal pattern, higher amplitude-to-wavelength ratios, thinner wires, smaller tortuous wires, fewer cross junctions, and deeper embedding within the elastomer substrate, have proven effective in improving the robustness of stretchable electronics. Epidermal electronics (with a 30 μm polyester substrate and a 0.5 μm Au/polyimide wire) built by using a "filament serpentine" layout showed remarkable conformal contact on pig skin and adequate adhesion only relying on van der Waals interaction[29]. The epidermal electronics incorporating serpentine pattern designs include different classes of semiconductor devices (amplifiers made of transistors, photovoltaic cells, light-emitting diodes, and oscillators) and sensors (temperature sensor built with serpentine Pt wires, and strain gauge based on carbon-black-doped silicone). One of limitations of the in-plane serpentine configuration design for achieving robustness is their relatively limited stretchability. That is because the film will totally fail beyond 54 % strain.

Kirigami design. The emerging approaches of creating slits or microcracks, borrowing from the concept of kirigami, have proven effective for the construction of wearable electronic devices (Figure 1.2D). kirigami is an art of paper cutting, where the

repetitive cut patterns on paper sheets that lead to a three-dimensional (3D) deformation can be borrowed to achieve robustness for intrinsically rigid materials[31]. Microscale slits or notches can be created by photolithography on metal films or/and elastomer substrates, such as Au on paper[31] and Pt on Parylene[35], to mimic the slits cut by scissors. When a tensile force is applied and exceeds a critical buckling force, the planar sheets begin to buckle and rotate to align with the applied load at the sites of the kirigami cuts. As a result, the kirigami patterned sheets display out-of-plane deflection, which accommodates the strain, making the devices stretchable. Except for a high mechanical stretchability demonstrated by this approach, the electronics created by kirigami patterned is also capable of maintaining a strain-invariant electrical conductance.

Microcracks. Stéphanie P. Lacour et al.[36] investigated the reversibility of flat gold films deposited by electron-beam evaporation on elastomeric substrates, and have observed that that the tri-branched microcrack patterns on the films deform by deflecting and twisting out-of-plane. The deformation of the microcracks results in a reduction in the energy at tips of the microcracks and inhibits the microcracks growth cross the metal film. Using the same principle, Yuting Chen et al.[32] have imparted mechanical robustness to gold films on an elastomeric substrate of PDMS by a solution-based electroless plating deposition. The unique deposition forms gold film with a heterogeneous crystalline surface texture, where the misaligned grains act as strong barriers to the dislocation progress and prevent failure of the film under cyclic strain.

1.2.3. Wrinkles that stretch

A recently developed strategy to produce stretchable elements for wearable electronic devices involves the use of wrinkled thin films[30] (Figure 1.2C). The fundamental theory underlying this strategy is that any material in considerably thin form becomes mechanically flexible because the bending strain decreases linearly with thickness. Particularly, a film has a critical strain (a minimum compressive strain at which it buckles), an equilibrium wavelength and amplitude[37]. The wavy shapes, the wavelength and amplitude, change to accommodate applied strains, and the underlying PDMS substrate provides an elastic restoring force, which behaves similarly to the mechanics of an accordion bellows[38].

Wrinkled thin films fabrication and transfer

Polystyrene (PS) is a thermoplastic polymer that can be softened and molded upon by heating it above its glass transition temperature ($T_g \approx 90$ °C). PS is a shape memory polymer (SMP), a class of materials that can return to an original shape when triggered by an external stimulus such as heat, electric or magnetic fields, and irradiation[39]. Typically, a heat active SMP is a rigid plastic at room temperature. Upon heating above its shape memory transition temperature (T_{trans}), commonly the glass transition temperature, the SMP material exists in a rubbery state and can be deformed. The deformation can be fixed and maintained by cooling the SMP below the transition temperature, even after removing the stress. This temperature is termed the shape fixing temperature (T_f), under which the polymer chains are immobilized. The shape memory behaviour can then be achieved by heating the material above the transition temperature with no applied constraints. At the molecular level, two basic structures, the net points and the switch segments, are required for SMP behaviour [40]. The net points (Figure 1.3, black dots) could be either covalent bonds or physical interactions and can define the permanent shape of the SMP only if they can endure the thermomechanical stimuli and if the bonds do not break during the shape memory process. Switch segments (Figure 1.3, blue and red lines) refer to segments along the chain where the chain mobility can be activated or depressed. Since switch segments are commonly associated to reversible thermal phase transitions, such as the glass transition or melting-crystallization transition, these are the main considerations in SMP design.

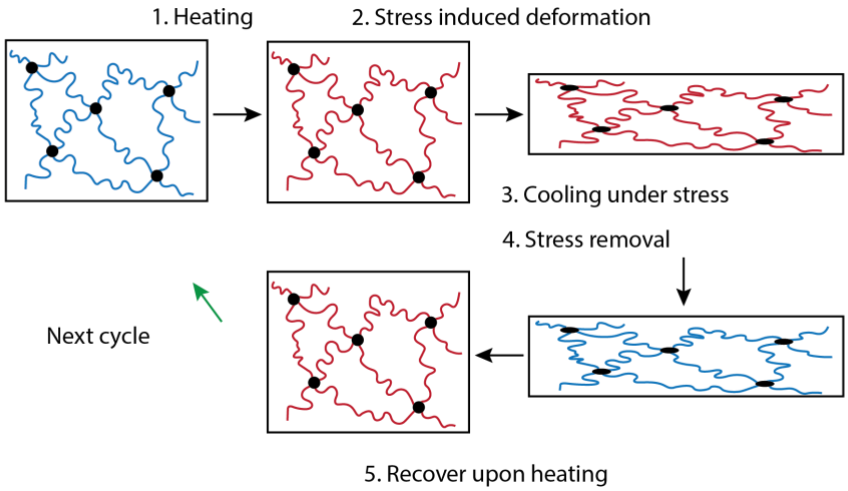

Figure 1.3. The molecular mechanism for a cycle of a shape memory process. Black dots: net points; blue lines: low mobility polymer chains; red lines: high mobility polymer chains.

The shape memory property of a biaxially pre-stressed PS film substrate was first reported as a strategy for reducing the feature size of thin metallic films formed by electroless deposition[41]. The miniaturization of the features was achieved by patterning the pre-stressed PS with a catalyst, then annealing the PS at a temperature slightly above its glass transition temperature. The shrinkage led to a size reduction of the patterned catalyst, and eventually to the miniaturization of the metallic film features. Later, the deposition of thin metallic films on a commercially available pre-stressed PS substrate, followed by shrinking was reported as a method for the rapid creation of tunable gold nano-wrinkles[42].

A series of transfer techniques have been developed to translate wrinkled thin films into materials for stretchable electronics. Generally, wrinkles on thin films can be created before or after the transfer process. Combining the simple and inexpensive thermal shrinking wrinkle fabrication with a structured thin film lift-off technique, the groups of Khine[43, 45] and the group of Moran-Mirabal[44] have transferred the wrinkled films onto elastomeric substrates to construct stretchable electrodes capable of conforming to curved surfaces and withstanding repeated external stimuli. A reversibly foldable and stretchable single-crystal silicon complementary metal-oxide semiconductor integrated circuit was demonstrated by forming wrinkles after a sacrificial layer-assisted transfer process[30]. The fabricated integrated circuits were

transferred onto a biaxially pre-strained PDMS substrate, and wavy structures were formed during the buckling process induced through the relaxation of the pre-strain. Wrinkled and wavy electrodes like those described above could contribute to the development of wearable electronics for applications in the healthcare and medical fields.

1.3. Characterization of stretchable electronics

The development of stretchable electrodes is crucial for the emerging field of wearable and implantable devices. The performances of conductivity and mechanical stretchability remain vital factors of evaluation. In addition, the corrosion resistance of the stretchable thin film will be discussed in the following content because of the potential applications in corrosive environment, such as ionic electrolytes in dye sensitized solar cells and body fluid environments.

1.3.1. Resistance and gauge factor

Gauge factor (GF) reflects the change in resistance over strain, and it is defined as the ratio of relative change in electrical resistance to the mechanical strain, i.e., $GF = \Delta R/(R \cdot \varepsilon)$, where $\Delta R/R$ is the relative change in resistance and ε is the applied strain. Therefore, brittle materials generally show higher gauge factors while materials with stretchability have smaller gauge factors[45].

1.3.2. Sheet resistance and four-point probe measurement

Electrical resistivity is one of the most important physical properties for the characterization of conductive materials and complex conductive device structures. Electrical resistivity is an intrinsic property of a conductive material that measures how strong it opposes the flow of electrical current. The symbol of electrical resistivity is the lower Greek letter ρ, and its SI unit is Ohm- meter ($\Omega \cdot m$). While electrical conductivity is the reciprocal of electrical resistivity, and it is a measure of a material's ability to

conduct electricity. The symbol of conductivity is the lower Greek letter σ, and the corresponding SI unit is Siemens/meter (S/m).

For two-dimensional (2D) isotropic thin films, sheet resistance is usually used to characterize the resistivity of the material. Sheet resistance can be directly measured through a four-point probe measurement. Sheet resistance varies with the materials and film thicknesses; thus, it is convenient to compare films with different thicknesses. Sheet resistance of a homogeneous thin film is defined as $R_s = \rho/t$, where ρ is the resistivity and t is the thickness of the film. According to this definition, in the case of a uniform thin film with fixed thickness, the sheet resistance could be assumed constant. The unit of sheet resistance is Ohm (Ω) but is often denoted as Ohm per square (Ω/sq) to differentiate it from bulk or volumetric resistance. The unit of sheet resistance (Ω/sq) indicates that the sheet resistance of a thin square film is independent with the size of the square.

The sheet resistance of a material can be calculated from the resistance measured by the four-point probe technique, which was developed to avoid the parasitic contact resistance encountered in two-point probe measurement. A four-point configuration to measure the sheet resistance of semiconductors was established in the microelectronics industry in 1975[46]. The configuration of collinear four-point probe is shown in Figure 1.4, where the current I is supplied through the outer two probes, and the voltage drop V is measured between the two inner probes[47].

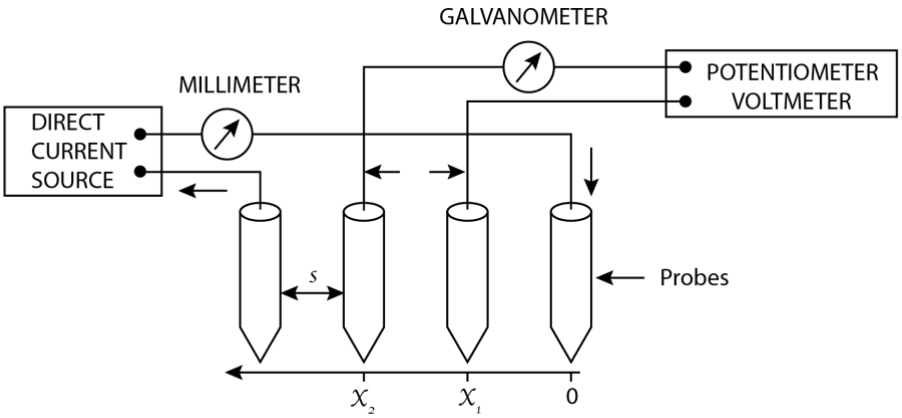

Figure 1.4. Schematic of the four-point probe configuration.

Compared with a bulk 3D material where a source of current is emanated from the probes, the current from the probes in a thin sheet material is assumed to spread cylindrically[48]. The comparison of current density for 3D bulk materials and 2D thin sheet is shown in Figure 1.5. For a very thin sheet of materials, it could be assumed that the thickness t is far smaller than the adjacent probe spacing s.

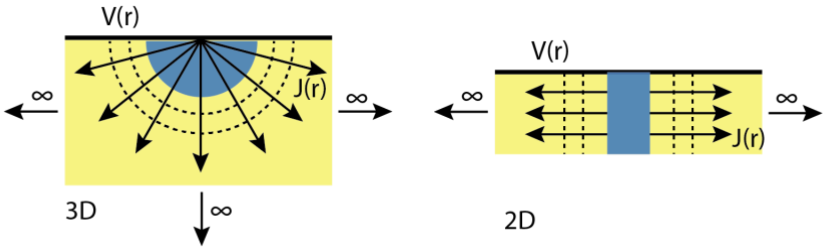

Figure 1.5. Profiles of current density $J(r)$ for a semi-infinite 3D material and an infinite 2D sheet.

To build the connection between the sheet resistance and the measured resistance, the difference between the two outer probes is calculated based on the following formula:

$$\Delta R = \rho \frac{dx}{A}$$

Where x is the distance along the direction of current flow (seen Figure 1.4), and A refer to the area of current spread. For thin sheets, the ring area of the current spread is given as:

$$A = 2\,\pi\,x\,t$$

Also, from Figure 1.4, it can be seen that:

$$x_2 = 2\,x_1 = 2s$$

The integration between the two inner probe tips is given as follows:

$$R = \int_{x_1}^{x_2} \rho \frac{dx}{A} = \int_{x_1}^{x_2} \rho \frac{dx}{2\pi t x} = \frac{\rho}{2\pi t} (\ln x)\Big|_{x_1}^{x_2} = \frac{\rho}{2\pi t} \ln 2$$

As the result of the superposition of the current at the two outer probe tips, the R can also be written as:

$$R = V/2I.$$

The resistivity of the thin sheet is thus obtained as follows:

$$\rho = \frac{2\pi t}{In\ 2} R = \frac{\pi t}{In\ 2} \left(\frac{V}{I}\right)$$

According to the expression of sheet resistance $R_s = \rho/t$, the sheet resistance R_s could be obtained as:

$R_S = \frac{\pi}{In\ 2}\ (\frac{V}{I})$

1.3.3. Corrosion resistance

For reliable and long-lasting human-machine interfaces such as implantable electronic devices and surgical tools, corrosion in body fluid environments is a challenge[49]. A similar situation where corrosion resistance is important is when an electrode is exposed to a liquid electrolyte that serves as the medium to transfer electrons from counter electrode to the oxidized dye in a dye-sensitized solar cell. The main composition of the liquid electrolyte is ~90 wt% of 3-methoxypropiononitrile and ~10 wt% of iodide/triiodide redox couple[50]. One of the drawbacks for the liquid electrolyte is the corrosion of noble metal counter electrodes, such as those made from Pt and Au[51]. Therefore, it is vitally important to develop stretchable conductive electrodes with corrosion resistant for wearable electronics. Typically, accelerated-lifetime soak testing is performed in saline (0.9 % NaCl solution at PH =7) at elevated temperatures (37 ˚C) to study the passivation performance of thin films[52,53]. In our research, films will be tested under voltage bias with the electrolyte solution containing I^-/I^{3-} redox couple, which is extremely corrosive to Au. We believe this method will be more stringent and faster compared to the accelerated-lifetime soak testing[54].

1.3.4. Inductive properties

Stretchable inductors are key components for oscillator circuits and for power transfer through inductive coupling. An inductor, consisting of a coil of conducting wire, is a passive electrical component used to store energy in a magnetic field. Inductors are widely used in electronics and power systems such as power supplies, transformers, radios, TVs, radars and electric motors[55]. When current passes through an inductor, the voltage across to the inductor is proportional to the time change rate of the current. This proportionality can be written as:

$$V = L \frac{di}{dt}$$

Where L, the proportionality constant, is called the inductance of inductor. The SI unit of inductance is the Henry (H), which is equal to 1 volt-second per Ampere (V·s/A). The inductance is strongly dependent on the geometry of the inductor. For example, the inductance of a solenoid inductor is:

$$L = \frac{N^2 \mu A}{l}$$

Where N is number of turns, l is the length, A is the cross-sectional area, and μ is the permeability of the core.

Another important figure of merit of inductors is the quality factor (Q), a measure of the efficiency of an inductor, which can be expressed as:

$$Q = \frac{\omega L}{R}$$

Where ω is the angular frequency of operation, and R is the resistance of the inductor.

The frequency, where parasitic capacitance of the inductor resonates with the inductance of the inductor, leading to an extremely high impedance, is called self-resonance frequency (SRF). SRF is an important parameter for inductors. An inductor is inductive at the frequency range below the SRF but is capacitive at the frequency range above it[56]. Therefore, the SRF restricts the frequency range of operation of an inductor. The SRF can be expressed as:

$$f_{SR} = \frac{1}{2\pi\sqrt{L C_p}}$$

Where L is the inductance of the inductor, and C_p is the parasitic capacitance of the inductor.

1.4 Applications and status of stretchable electronics

1.4.1. Electronic skin/user-interactive interfaces

Inspired by human skin, electronic skin (sensitive skin or smart skin) is a large-area, stretchable network of electronic devices, which could be used to cover the surface

of a machine or even a part of the human body[19,59]. Electronic skin should enable carriers to feel and respond to their surroundings by proximity, tactile, pressure, temperature, chemical or other sensors. Equipped with multiplexed sensing capabilities, machines or robots could work more effectively in unpredictable and complex environments. The machines or robotics could care for the disabled and the elderly, bringing drastic changes to the service industry. Electronic skin could also open the door for applications in medical and biological fields, such as improving the sensitivity of limb prosthetics and restoring damaged skin. The advanced sensing ability of electronic skin could also contribute to defense systems such as active camouflage.

An example towards the development of electronic skin, demonstrated the fabrication of an array of 16 × 16 pixels (size ~3 × 3.5 cm^2) on polyimide that could act as a set of conformal sensors and a display[60] (Figure 1.6). This system-on-plastic contained three distinct electronic components, a thin-film transistor, a pressure sensor, and an organic light-emitting diode and was designed for pressure visualization and sensing. Although the electronic skin functioned properly within a minimal radius of 4 mm, mechanical stretchability has not been achieved because the materials and structures used were mostly rigid electronics. For example, the back-gate electrodes for the thin-film transistor were flat Ti/Au films and the contact pads connecting the drain of each a thin-film transistor and organic light-emitting diode were made of sputtered indium tin oxide (ITO). Nevertheless, this work showcased a vision of electronic skin as a user-interactive interface. However, this is where we can see that the development of intrinsically stretchable devices will benefit the development of electronic skins.

Figure 1.6. Different colored (green, blue, and red) interactive e-skins were used to spatially map and display the pressure applied with "C", "A" and "L" shaped PDMS slabs, respectively. Adapted by permission from: Springer Nature, reference [60]. Copyright 2013.

1.4.2. Health monitoring/therapeutic devices

The integration of electronic skin on health monitoring devices could greatly improve the of physiological signal resolution because of its ability of being conformal to curvilinear skin and tissue[61,62]. Combined with wireless sensing and the use of soft and lightweight materials, it could make continuous health monitoring and tracking more accessible.

Near-field communication (NFC) can be used for contactless data exchange over short distances. Although its working range (about 20 cm) is small, NFC gives high level of security because of limited access to data beyond this distance. NFC is also compatible with mobile electronic devices, which is why it is widely used to process mobile payments. The group of Rogers has fabricated an ultra-thin, soft, and wireless epidermal electronic system for neonatal intensive care units, which relays biological information that is essential to clinical care[63,64]. Hard-wired connections of conventional rigid sensing systems can complicate basic bedside tasks, emergency interventions, and the therapeutic skin-to-skin contact between parents and their infants. Wireless wearable alternatives bypass those limitations and can offer functionality equivalent to that of existing clinical standards. Figure 1.7A, B shows a photograph and a schematic illustration of the epidermal electronic system used for recording electrocardiograms. The main components of the system include skin-interfaced electrodes made of metal mesh microstructures, multiple chip-scale integrated circuits, and a magnetic loop antenna. The magnetic loop is made of serpentine Cu traces with widths of 50-100 μm and thickness of 5 μm and is tuned to comply with NFC protocols for simultaneous wireless data transmission and power delivery. It was reported that the epidermal electronic system could be uniaxially stretched up to a strain of 20% in the long axis direction, while the changes in the inductance, quality factor, and resonant frequency of the antennas were minimal (< 5%).

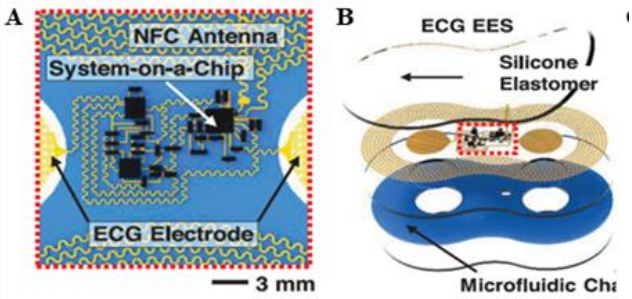

Figure 1.7. Schematic illustration of a wireless, battery-free module for recording electrocardiogram, photoplethysmogram data and skin temperature. The ionic liquid in the microfluidic channel contains blue dye for visualization purposes. From reference [67]. Adapted with permission of AAAS.

Thermal therapy is one of the most common physiotherapies, especially in orthopedics. It is known to have positive effects on alleviating joint pain and stiffness caused by injuries, obesity or aging[65]. Heat therapy is also beneficial to reduce athletic injuries by increasing muscular and ligament flexibility[66]. The existing thermal therapy packs are not only lacking precise temperature control, but also heavy and bulky. Although thermal wraps have improved some of these properties, they are mechanically rigid and cannot closely conform to the irregular surface of human joints. Thus, an important development would be the production of stretchable heaters with better wearability, which could be conformally integrated to the complex shape of joints and achieve improved point-of-care treatment.

The stretchable elements that rely on joule heating, need to be electrically and thermally conductive, mechanically robust, and chemically stable[67]. Many materials have been investigated for use as conductive elements of stretchable heaters, such as graphene fibers, AgNWs[68], and nano-trough network of metallic glasses[67], among others, and different approaches have shown unique advantages on fabrication, performance and stability. Suji Choi et al.[65] reported a stretchable heater using a nanocomposite containing AgNWs and a thermoplastic styrene-butadiene-styrene elastomer. The AgNWs surface was chemically modified[69] to facilitate its dispersion in the thermoplastic elastomer. The heating layer was soft and thin and was patterned into a serpentine-mesh to accommodate strain and provide conformality to a curved surface. To fabricate the stretchable heater, the heating layer was encapsulated between two insulation layers (Figure 1.8A). The serpentine patterned heater was integrated into an

electronic band consisting of a power supply and a microcontroller unit and exhibited good wearability upon upward and downward movements of the wrist. The heater showed the best stretchability when the mixing ratio of AgNWs/SBS was 18/82, where the loading of AgNWs approached saturation. The temperature of the stretchable heater could reach ~40°C when the applied voltage was 1V.

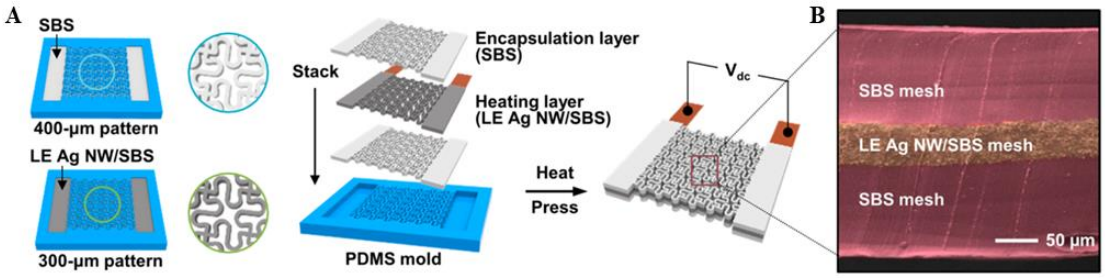

Figure 1.8. A stretchable and wearable heater for thermal therapeutic applications. (**A**) Schematic of the fabrication process for the mesh heater. (**B**) SEM images showing the bonded interfaces. Adapted with permission of reference [70]. Copyright 2015 American Chemical Society.

1.4.3. Minimally invasive surgical and diagnostic electronic bio-interfaces

One of the most intensively developing areas is that focused on surgical and diagnostic implements that can integrate with the human body to provide advanced therapeutic capabilities. A well demonstrated example is the multifunctional balloon catheter (Figure 1.9) which has the ability to provide electrophysiological mapping of the heart and ablation therapy, and can be used to diagnose and resolve complex arrhythmia heart diseases[3]. Conventional catheters are powerful tools for delivering therapeutic treatments and facilitating diagnosis of biological tissues. They enable minimal invasive insertion and can be configured to provide controlled inflation. Based on existing catheters, multifunctional catheters could be directly equipped with stretchable electronic materials and devices. The integrated catheters, a platform combined with actuators, sensors, and radio frequency ablation electrodes, could provide versatile operation modes and dynamic information (e.g., electrical, tactile, temperature and flow rate) in real time during the surgical work. Catheters could help decrease morbidity and facilitate the operation by providing vital information to the

time-intensive surgical work. The key to incorporate electrically conductive materials and achieve high level of stretchability to adapt to the inflation and deflation of the catheter has been the use of mesh layouts. These have incorporated thin Au films in serpentine geometries as interconnections and high modulus nodes. This example reveals a technology foundation for advanced, minimally invasive surgical and diagnostic tools.

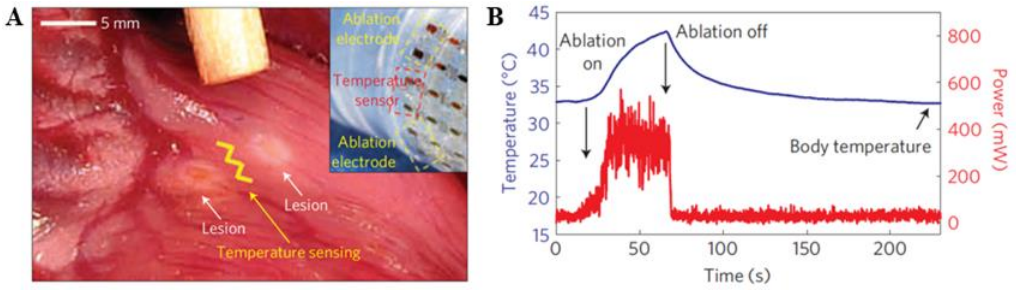

Figure 1.9. ***In vivo*** **epicardial recordings of cardiac electrophysiological, temperature data and RF ablation in a rabbit heart.** (**A**) Optical image of epicardial ablation lesion. The yellow line denotes the area of temperature sensing. (**B**) An image of representative RF electrodes collocated with temperature sensors. Adapted by permission from: Springer Nature, reference [3]. Copyright 2011.

1.4.4. Integration of wireless technology in stretchable electronics

Wireless sensing design

The integration of wireless sensing in stretchable electronics could enable the continuous detection of signals when attached or implanted into a user body without disrupting their daily activities[72]. Wireless sensing could be used for sensing under harsh environments[71], but it is especially useful for monitoring biological signals in healthcare and diagnosing diseases. For example, wearable smart contact lenses for measuring intraocular pressure and glucose[73], physiological monitoring devices like arterial pulse sensors for wireless monitoring of blood flow[74], and retinal prosthesis for vision restoration[75].

In addition to improving user comfort, safety, and convenience of electronics, the design of wearable electronics should also address the continuous tracking of biological signals. From the design perspective, there are two ways to develop wireless

functionality for stretchable sensors: integrating wireless power supply and data communication circuits within the stretchable sensors; developing stretchable sensors to transduce radiofrequency signals. The technologies of wireless integration, which primarily involve integrating wireless power supply and wireless data communication into stretchable electronic devices, are key to achieving continuous signal monitoring[72].

In general, wireless power supply can be achieved through energy harvesting technologies or wireless power transfer. Energy harvesting technologies could directly generate sustainable power through the devices within the wearable electronic systems. For example, Chao Li et al.[76] have reported a wearable strain sensor powered by a flexible perovskite solar cell-driven lithium-ion rechargeable capacitor.

In the case of wireless power transfer, the delivered power could be used for charging integrated batteries or directly operating wearable sensors. Battery-free power systems could miniaturize the size sensors and avoid some safety issues such as battery explosion and electrolyte leakage[77]. Wireless power transfer could be achieved by inductive coupling, where electromagnetic fields are used to transfer radiofrequency power via induction from a transmitting antenna to a receiving antenna.

Inductive coupling includes the modalities of resonant and non-resonant inductive coupling. Resonant coupling tunes the resonance frequency of the transmitting antenna and the receiving antenna to a predetermined range. By resonance matching, resonant inductive coupling can achieve high power transfer efficiency and allow relatively long-distance transfer. In the case of non-resonant inductive coupling, it is more suitable for short-distance transfer, but has the advantage of simpler structural components.

Wireless data communication refers to the data transfer between two or more points without using a conductor as the transfer medium. The most widely used wireless data communication method adopted for wearable electronics are radiofrequency identification (RFID), bluetooth, NFC, resonant antenna, and optical communication. These wireless data communication technologies differ on power source (battery-free, battery-assisted, or battery powered), operating frequency, data rate, working range and power consumption. Although different wireless data communication technologies are integrated according to the specific applications, the work on this thesis encompasses

the development of stretchable inductors, which can be used primarily for RFID, NFC and resonant antenna implementations.

Wireless stretchable electronics

RFID uses electromagnetic fields to identify or track tags, which consist of transceivers and chips, within a short range. Sensors integrated with RFID could be classified into three categories: passive, active or semi-active, according to the function or the power source. The operating frequencies of RFID are 120-140 kHz (low-frequency identification), 13.56 MHz (high-frequency identification), and 868-956 MHz (ultrahigh-frequency identification). The working distance depends on the operating frequency. Recent work has demonstrated the incorporation of a fully stretchable on-skin sensor and a flexible on-textile readout circuit to gather physiological information and tracking of human movement wirelessly *via* RFID technology (Figure 1.10)[78]. The device consisted of a reader and a stretchable sensor free of batteries or rigid integrated circuits. The stretchable on-skin sensor comprised an inductor, a capacitor, and a resistive strain sensor, which were made of stretchable conductive ink, styrene thermoplastic elastomers, and carbon nanotubes. The electronic sensor tags could record a person's pulse, breath, and body movement simultaneously and continuously in a hand-free fashion. The highlight of this research was achieving a battery- and chip-free stretchable on-skin interface with wireless power and data transfer. One of the drawbacks was the low resolution of the sensors due to the large target size.

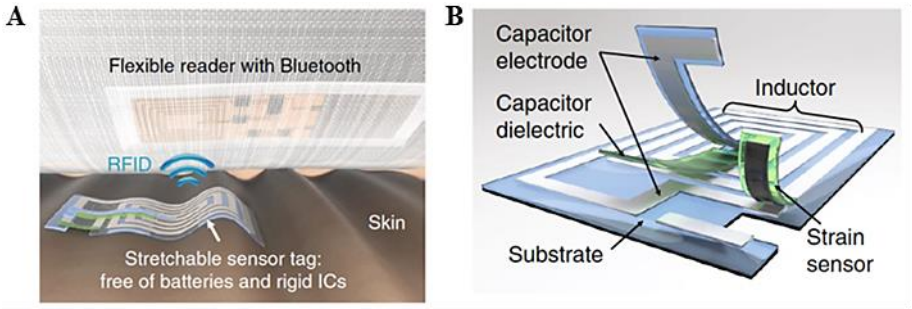

Figure 1.10. Design of the stretchable sensor target and flexible initiator. (**A**) A stretchable sensor is conformally attached on skin. (**B**) Information is wirelessly read out by a flexible

printed circuit board (FPCB) initiator on clothing. Adapted by permission from: Springer Nature, reference [78]. Copyright 2019.

In the work shown in Figure 1.11, the group of Rogers developed a stretchable sensor used for epidermal analysis of biofluids[79]. The sensor was an LC resonator, where the inductor was made of 6 μm Cu serpentine traces and the capacitor of 200 nm Au traces with an interdigitated configuration. The capacitor itself acted as a capacitive sensor, where it was designed to characterize the volume of absorbed sweat through the dielectric change of the soft sponge substrate. The capacitance change altered the radio frequency characteristics of the antenna, which acted as the resonance frequency (f_0) of the sensor. The resonance frequency could be measured by the shift of phase peak of a primary coil placed in proximity to the device as shown in Figure 1.11B, and determined by the frequency of a phase dip in the phase frequency spectrum of the primary coil[80–83]. The resonance frequency decreased as the volume of the absorbed buffer solution (sweat) increased (Figure 1.11C). The fact that the biaxial stretching had negligible effect on f_0 up to 27% strain made the characterization possible. The LC resonator has potential compatibility with the NFC systems for wireless sensing.

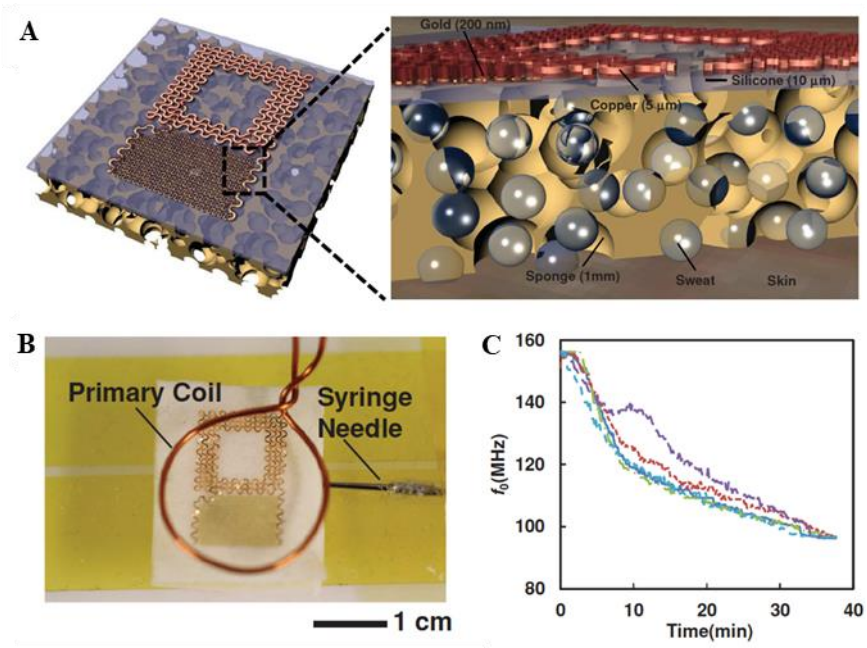

Figure 1.11. A passive wireless capacitive sensor. (**A**) Schematic illustration of a passive wireless capacitive sensor designed for sensing of sweat from the surface of skin. (**B**) Picture of a sweat sensor underneath a primary coil. A syringe needle inserted into the sensor delivers

controlled amounts of a buffer solution through a syringe pump, and (**C**) Change in resonance frequency of a sweat sensor on a cellulose paper substrate as a function of time during controlled injection of buffer solution. Adapted with permission from reference of [79]. Copyright 2014 John Wiley and Sons.

With the role that wireless sensing playing in the stretchable electronics for continuous monitoring, we believe it is essential to work on the wireless sensing devices and apply the approach that we have developed to contribute to the integration of wireless sensing into stretchable electronics.

1.4.5. Stretchable electronics for dye-sensitized solar cells

Working principle of dye-sensitized solar cells

Dye-sensitized solar cells (DSSCs) belong to the group of thin film solar cells. They offer the prospect of low-cost fabrication, ease of being shaped and tinted for applications on domestic devices and architectures, and using flexible substrates[84]. Different from conventional p-n junction photovoltaics where semiconductors are responsible for light absorption and charge separation, DSSCs contain a sensitizer to absorb light and the charge separation happens when the photo-induced electron is injected into the conducting band of the semiconductor (Figure 1.12). One of the key components of DSSCs is a mesoporous oxide layer, which is typically made of nanocrystalline TiO_2 (band gap ~3.2 eV). The mesoporous TiO_2 layer provides a large internal surface area for the dye to adsorb onto, which greatly facilitates the absorption of incident light. A mesoporous 10 μm-thick film made of 15 nm spherical TiO_2 particles is expected to have 2000× the surface area of a smooth surface[85]. To form a percolating network and facilitate the electronic contact between TiO_2 nanoparticles, the mesoporous film is sintered at high temperatures (~450°C).

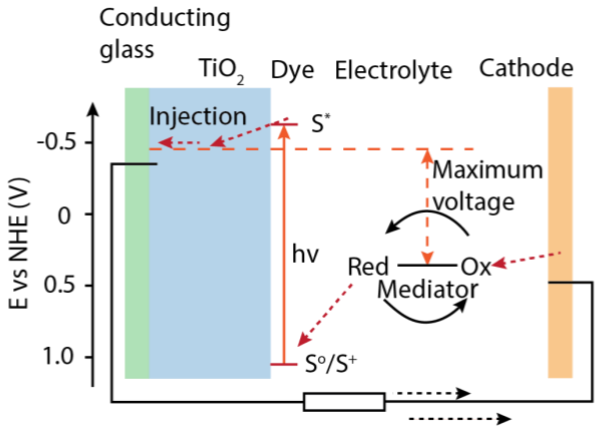

Figure 1.12. Schematic diagram showing the operation of a DSSC.

The dye on the surface of the semiconductor layer absorbs light and injects electrons into conducting band of the oxide and regains electrons from the electrolyte. The electrolyte is usually an organic solvent containing a redox couple, typically iodide/triiodide. Electrons from external load also migrate to the electrolyte from the cathode electrode. The voltage generated by the cell equals the difference between the Fermi level of the TiO_2 under illumination and the Nernst potential of the redox couple in the electrolyte[86].

Back-contact DSSCs

Back-contact solar cells refer to designs where both positive and negative external contact pads are positioned on the back (non-illuminated) surface of the cell. Depending on the structural properties, back-contact solar cells can be classified as metallisation wrap-through, emitter wrap-through, and back-junction devices[87]. Although the structural designs are different, the aim is to reach an optimal balance between having low coverage of the metal grid to reduce optical losses and having high coverage to minimize resistive losses. Because back-contact solar cells have the junction and

contact pads at the rear surface, there is no metallization pattern on the front surface that blocks incident light. Back-contact solar cells typically use a set of interdigitated finger electrodes. In addition to improving incident light transmission, the back-contact configuration offers flexibility on material choices, such as using more conductive electrode materials without transparency concerns and the ability to use opaque materials as the substrate. The configuration also provides a platform that could host the wiring and the interconnections on a common substrate, which would be beneficial to the fabrication and integration of an interconnected solar cell into the electronic circuitry.

Figure 1.13 shows a comparison between the configurations of a conventional sandwiched DSSC and a back-contact DSSC[88]. The sandwiched DSSC consists of two transparent fluorine-doped tin oxide (FTO) electrodes, which are located on opposite sides of the junction. The one at the bottom is a photoelectrode coated with mesoporous TiO_2, and the one on the top is the platinized counter electrode. These two electrodes need to be conductive and at least one of them must be transparent to allow the incident light to pass through. For the back-contact DSSC, a set of two interdigitated finger electrodes, *i.e.*, the photoelectrode and the counter electrode, are positioned at the bottom. To provide a pathway for the incident light to pass through, back-contact DSSC only needs the top sealing layer to be transparent.

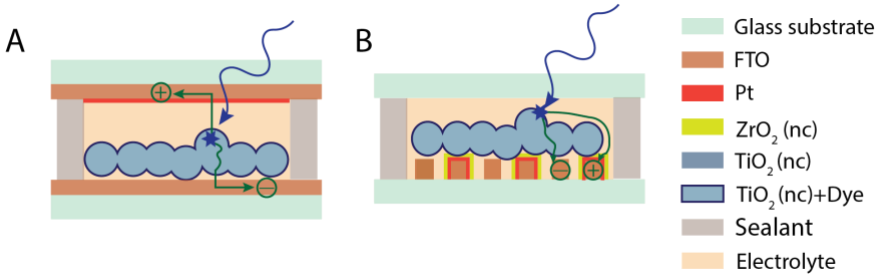

Figure 1.13. **Schematic DSSC configuration.** (**A**) A conventional sandwiched DSSC. (**B**) A back-contact DSSC.

Room temperature fabrication of mesopororus TiO_2 layers

A key step in the fabrication of conventional DSSC is to sinter the deposited TiO_2 nanoparticle layer at 450°C. The purpose is to remove the organic binder and solvent, and to improve the electrical contact between the network of particles.

A strategy to be able to compete with existing photovoltaic technologies is to enhance the solar energy conversion efficiency of DSSCs and produce them at low-cost via roll-to-roll processes[89]. A prerequisite for roll-to-roll manufacturing is the use of flexible substrates, which are not usually compatible with high temperature sintering. The use of room-temperature TiO_2 compression to replace high-temperature TiO_2 sintering has been a promising route to address this challenge. Under the same fabrication conditions, the efficiency of DSSC with compressed TiO_2 film on glass has reached ~4.5% under 0.1 sun condition, which is comparable to the efficiency of DSSC with sintered TiO_2 film on glass[89]. An energy conversion efficiency of 1.66% has been achieved for a DSSC fabricated on a flexible ITO-polyethylene naphthalate substrate with a TiO_2 film fabricated by compression after electrophoretic deposition[90]. An efficiency of 7.4% has been reached for a DSSC on ITO-polyethylene naphthalate substrate with compression and a light confinement effect of TiO_2 film[91].

Given the success of building DSSCs through compressing mesoporous TiO_2 at room temperature and fabricating DSSCs with back-contact configuration, we have worked by adding these two concepts together. Along with introducing with an interdigitated electrode fabricated with simplified methods, we have developed a route for the development of stretchable solar cells.

1.5 The coming chapters

In the following chapters, four research chapters will be introduced. Firstly, it will be focusing on the wrinkled stretchable multilayer electrodes technique development, which will illustrate two solvent-assisted structured films transfer approaches and offer the advantages and disadvantages of each approach. In this chapter, stretchable thin film

heaters made of Au and ITO/Au/ITO will also be demonstrating to show the effectiveness of the method in developing stretchable electronics. Secondly, a corrosion resistant stretchable multilayer electrode will be illustrated. Within this chapter, I will introduce a new concept of building electrode by adjusting the thickness of the insulation layer, and the flexibility of the transfer method. Thirdly, you will see a spiral-shaped stretchable inductor fabricated with the wrinkled film transfer approach. The wrinkled stretchable inductors possess lower resistance than the flat ones, which will benefit for the inductive efficiency. This is an obvious advantage over most of the existing methods that achieves stretchability at the expense of increasing resistance. Finally, it is a preliminary work of developing stretchable DSSCs. A back-contact DSSCs with an interdigitated electrode and mesoporous TiO_2 layer compressed at room temperature are demonstrated for the first time. Although the efficiency is relatively low, it offers some insight and provides a viable route for the next step stretchable DSSCs development. With all these works, I hope it will contribute to the advancement of stretchable electronics development and accelerate the implantation of stretchable electronics in human health care, therapeutic treatment, and communication.

References

1. Rogers, J.A.; Someya, T.; Huang, Y. Materials and mechanics for stretchable electronics. *Science* **2010**, *327*, 1603-1607.
2. Wang, S. *et al.* Skin electronics from scalable fabrication of an intrinsically stretchable transistor array. *Nature* **2018**, *555*, 83-88.
3. Kim, D. H. *et al.* Materials for multifunctional balloon catheters with capabilities in cardiac electrophysiological mapping and ablation therapy. *Nat. Mater.* **2011**, *10*, 316-323.
4. Ilievski, F.; Mazzeo, A. D.; Shepherd, R. F.; Chen, X. & Whitesides, G. M. Soft robotics for chemists. *Angew. Chemie* **2011**, *123*, 1930-1935.
5. Altmüller, R.; Schwödiauer, R.; Kaltseis, R.; Bauer, S. & Graz, I. M. Large area expansion of a soft dielectric membrane triggered by a liquid gaseous phase change. *Appl. Phys. A Mater. Sci. Process.* **2011**, *105*, 1-3.
6. Pelrine, R.; Kornbluh, R.; Pei, Q. & Joseph, J. High-speed electrically actuated elastomers with strain greater than 100%. *Science* **2000**, *287*, 836-839.
7. Carpi, F.; Bauer, S.; Rossi, D. D. Stretching dielectric elastomer performance. *Science* **2010**, *330*, 1759-1761.
8. Wagner, S. & Bauer, S. Materials for stretchable electronics. *MRS Bull.* **2012**, *37*, 207-213.
9. Trung, T. Q. & Lee, N. E. Recent progress on stretchable electronic devices with intrinsically stretchable components. *Adv. Mater.* **2017**, *29*, 1603167.
10. Dickey, M. D. Stretchable and soft electronics using liquid metals. *Adv. Mater.* **2017,** *29*, 1606425.
11. Matsuhisa, N.; Chen, X.; Bao, Z. & Someya, T. Materials and structural designs of stretchable conductors. *Chem. Soc. Rev.* **2019**, *48*, 2946-2966.
12. Hirsch, A.; Michaud, H. O.; Gerratt, A. P.;Mulatier, S. & Lacour, S. P. Intrinsically stretchable biphasic (solid-liquid) thin metal films. *Adv. Mater.* **2016,** *28*, 4507-4512.
13. Feig, V. R.; Tran, H.; Lee M. & Bao, Z. Mechanically tunable conductive interpenetrating network hydrogels that mimic the elastic moduli of biological tissue. *Nat. Commun.***2018,** *9*, 1-9.
14. Liang, J.; Li, L.; Niu, X.; Yu, Z. & Pei, Q. Elastomeric polymer light-emitting devices and displays. *Nat. Photonics* **2013,** *7*, 817-824.
15. Yang, C. & Suo, Z. Hydrogel ionotronics. *Nat. Rev. Mater.* **2018,** *3*, 125-142.
16. Rivnay, J. *et al.* Structural control of mixed ionic and electronic transport in conducting polymers. *Nat. Commun.* **2016,** *7*, 1-9.
17. Khodagholy, D. *et al.* NeuroGrid: Recording action potentials from the surface of the brain. *Nat. Neurosci.* **2015,** *18*, 310-315.
18. Hansen, T. S.; West, K.; Hassager, O. & Larsen, N. B. Highly stretchable and conductive polymer material made from poly(3,4-ethylenedioxythiophene) and polyurethane elastomers. *Adv. Funct. Mater.* **2007,** *17*, 3069-3073.
19. Hammock, M. L.; Chortos, A.; Tee, B. C. K.; Tok, J. B. H. & Bao, Z. 25th anniversary article: The evolution of electronic skin (E-Skin): A brief history, design considerations, and recent progress. *Adv. Mater.* **2013,** *25*, 5997-6038.
20. Keplinger, C. *et al.* Stretchable, transparent, ionic conductors. **2013,** *341*, 984-

987.
21. Larson, C. *et al.* Highly stretchable electroluminescent skin for optical signaling and tactile sensing. *Science* **2016,** *351*, 1071-1074.
22. Sekitani, T. *et al.* A rubberlike stretchable active matrix using elastic conductors. **2008**, *321*, 1468-1472.
23. Matsuhisa, N. *et al.* Printable elastic conductors with a high conductivity for electronic textile applications. *Nat. Commun.* **2015,** *6*, 1-11.
24. Matsuhisa, N. *et al.* Printable elastic conductors by in situ formation of silver nanoparticles from silver flakes. *Nat. Mater.* **2017,** *16*, 834-840.
25. Kim, Y. *et al.* Stretchable nanoparticle conductors with self-organized conductive pathways. *Nature* **2013,** *500*, 59-63.
26. Stoyanov, H.; Kollosche, M.; Risse, S.; Waché, R. & Kofod, G. Soft conductive elastomer materials for stretchable electronics and voltage controlled artificial muscles. *Adv. Mater.* **2013,** *25*, 578-583.
27. Kim, D. H.; Ghaffari, R.; Lu, N. & Rogers, J. A. Flexible and stretchable electronics for biointegrated devices. *Annu. Rev. Biomed. Eng.* **2012,** *14*, 113-128.
28. Lee, J. *et al.* Stretchable GaAs photovoltaics with designs that enable high areal coverage. *Adv. Mater.* **2011,** *23*, 986-991.
29. Kim, D. *et al.* Epidermal Electronics. **2011,** *333*, 838-843.
30. Kim, D. H. *et al.* Stretchable and foldable silicon integrated circuits. *Nature* **2008,** *320*, 507-511.
31. Shyu, T. C. *et al.* A kirigami approach to engineering elasticity in nanocomposites through patterned defects. *Nat. Mater.* **2015,** *14*, 785-789.
32. Chen, Y.; Wu, Y.; Mechael, S. S. & Carmichael, T. B. Heterogeneous surface orientation of solution-deposited gold films enables retention of conductivity with high strain - a new strategy for stretchable electronics. *Chem. Mater.* **2019,** *31*, 1920-1927.
33. Kim, D. H. *et al.* Materials and noncoplanar mesh designs for integrated circuits with linear elastic responses to extreme mechanical deformations. *Proc. Natl. Acad. Sci.***2008,** *105*, 18675-18680.
34. Gray, D. S.; Tien, J. & Chen, C. S. High-conductivity elastomeric electronics. *Adv. Mater.* **2004,** *16*, 393-397.
35. Morikawa, Y. *et al.* Ultrastretchable kirigami bioprobes. *Adv. Healthc. Mater.* **2018,** ***7***, 1702100.
36. Lacour, S. P.; Chan, D.; Wagner, S.; Li, T. & Suo, Z. Mechanisms of reversible stretchability of thin metal films on elastomeric substrates. *Appl. Phys. Lett.* **2006,** *88*, 2004-2007.
37. Lacour, S. P.; Wagner, S.; Huang, Z. & Suo, Z. Stretchable gold conductors on elastomeric substrates. *Appl. Phys. Lett.* **2003,** *82*, 2404-2406.
38. Jiang, H. *et al.* Finite deformation mechanics in buckled thin films on compliant supports. *Proc. Natl. Acad. Sci.* **2007,** *104*, 15607-15612.
39. Mather, P. T.; Luo, X. & Rousseau, I. A. Shape memory polymer research. *Annu. Rev. Mater. Res.* **2009,** *39*, 445-471.
40. Zhao, Q.; Qi, H. J. & Xie, T. Recent progress in shape memory polymer: New behavior, enabling materials, and mechanistic understanding. *Prog. Polym. Sci.*

2015, *49*, 79-120.
41. Hidber, P. C.; Nealey, P. F.; Helbig, W. & Whitesides, G. M. New strategy for controlling the size and shape of metallic features formed by electroless deposition of copper: microcontact printing of catalysts on oriented polymers, followed by thermal shrinkage. *Langmuir* **1996,** *12*, 5209-5215.
42. Fu, C. C. *et al.* Tunable nanowrinkles on shape memory polymer sheets. *Adv. Mater.* **2009,** *21*, 4472-4476.
43. Kim, J. *et al.* Highly stretchable wrinkled gold thin film wires. *Appl. Phys. Lett.* **2016,** *108*, 061901.
44. Zhu, Y. & Moran-Mirabal, J. Highly bendable and stretchable electrodes based on micro/nanostructured gold films for flexible sensors and electronics. *Adv. Electron. Mater.* **2016,** *2*, 1-6.
45. Liu, Z. *et al.* Thickness-gradient films for high gauge factor stretchable strain sensors. *Adv. Mater.* **2015,** *27*, 6230-6237.
46. Miccoli, I.; Edler, F.; Pfnür, H. & Tegenkamp, C. The 100th anniversary of the four-point probe technique: The role of probe geometries in isotropic and anisotropic systems. *J. Phys. Condens. Matter* **2015,** *27*, 223201.
47. Valdes, L. B. Resistivity measurements on germanium for transistors. *Proc. IRE* **1954,** *42*, 420-427.
48. Chen, J.; Friedberg, P. Four-point probe manual. *University of California, Berkeley* **1994**.
49. Xian, H. *et al.* Development of stretchable metallic glass electrodes. *Nanoscale* **2021,** *13*, 1800-1806.
50. Safety data sheet for EL-HSE high stability electrolyte. **2020**. Available at: https://www.sigmaaldrich.com/CA/en/sds/aldrich/791466.
51. Ye, M. *et al.* Recent advances in dye-sensitized solar cells: From photoanodes, sensitizers and electrolytes to counter electrodes. *Mater. Today* **2015,** *18*, 155-162.
52. Li, W. *et al.* Wafer-level parylene packaging with integrated rf electronics for wireless retinal prostheses. *J. Microelectromechanical Syst.* **2010,** *19*, 735-742.
53. Kim, B. J. & Meng, E. Micromachining of Parylene C for bioMEMS. *Polym. Adv. Technol.* **2016,** *27*, 564-576.
54. Miettunen, K.; Vapaavuori, J.; Poskela, A.; Tiihonen, A. & Lund, P. D. Recent progress in flexible dye solar cells. *Wiley Interdiscip. Rev. Energy Environ.* **2018**, ***7***, 1-11.
55. Alexander, C. K. *Electricity: Electric Circuits*. **2000,** *135*, 4-5
56. Kuhn, W. B. & Ibrahim, N. M. Analysis of current crowding effects in multiturn spiral inductors. *IEEE Trans. Microw. Theory Tech.* **2001,** *49*, 31-38.
57. Wang, Y. & Li, Z. Group-cross symmetrical inductor (GCSI): a new inductor structure with higher self-resonance frequency and Q factor. *IEEE transactions on magnetics* **2006,** *42*, 1681-1686.
58. Capacitance, H.; Srf, A.; Resonance, S.; Effects, F. & Measurements, S. R. F. measuring self resonant frequency. **2002,** 1-3.
59. Misery, L. Sensitive skin. *Pruritus Second Ed.* **2016,** *1*, 127-129.
60. Wang, C. *et al.* User-interactive electronic skin for instantaneous pressure visualization. *Nat. Mater.* **2013,** *12*, 899-904.

61. Mukhopadhyay, S. C. Wearable sensors for human activity monitoring: A review. *IEEE Sens. J.* **2015,** *15*, 1321-1330.
62. Yang, S. *et al.* 'cut-and-paste' manufacture of multiparametric epidermal sensor systems. *Adv. Mater.* **2015,** *27*, 6423-6430.
63. Chung, H. U. *et al.* Binodal, wireless epidermal electronic systems with in-sensor analytics for neonatal intensive care. *Science* **2019,** *363*, eaau0780.
64. Ma, Y. *et al.* Soft elastomers with ionic liquid-filled cavities assStrain isolating substrates for wearable electronics. *Small* **2017,** *13*, 1-10.
65. Choi, S. *et al.* Stretchable heater using ligand-exchanged silver nanowire nanocomposite for wearable articular thermotherapy. *ACS Nano* **2015,** *9*, 6626-6633.
66. Petrofsky, J. S.; Laymon, M. & Lee, H. Effect of heat and cold on tendon flexibility and force to flex the human knee. *Med. Sci. Monit.* 2013, **19**, 661-667.
67. An, B. W. *et al.* Stretchable, Transparent electrodes as wearable heaters using nanotrough networks of metallic glasses with superior mechanical properties and thermal stability. *Nano Lett.* **2016,** *16*, 471-478.
68. Hong, S. *et al.* Highly stretchable and transparent metal nanowire heater for wearable electronics applications. *Adv. Mater.* **2015,** ***27***, 4744-4751.
69. Dong, A. *et al.* A generalized ligand-exchange strategy enabling sequential surface functionalization of colloidal nanocrystals. *J. Am. Chem. Soc.* **2011,** *133*, 998-1006.
70. Choi S.*et al.* Stretchable heater using ligand- exchanged silver nanowire nanocomposite for wearable articular thermotherapy. *ACS nano*, **2015,** *9*, 6626-6633.
71. Huang, Q. A.; Dong, L. & Wang, L. F. LC Passive wireless sensors toward a wireless sensing platform: status, prospects, and challenges. *J. Microelectromechanical Syst.* **2016,** *25*, 822-841.
72. Park, Y. G.; Lee, S. & Park, J. U. Recent progress in wireless sensors for wearable electronics. *Sensors (Switzerland)* **2019,** *19*, 1-34.
73. Kim, J. *et al.* Wearable smart sensor systems integrated on soft contact lenses for wireless ocular diagnostics. *Nat. Commun.* **2017,** *8*, 1-8.
74. Boutry, C. M. *et al.* Biodegradable and flexible arterial-pulse sensor for the wireless monitoring of blood flow. *Nat. Biomed. Eng.* **2019,** *3*, 47-57.
75. Lorach, H. *et al.* Photovoltaic restoration of sight with high visual acuity. *Nat. Med.* **2015,** *21*, 476-482.
76. Li, C. *et al.* Flexible perovskite solar cell-driven photo-rechargeable lithium-ion capacitor for self-powered wearable strain sensors. *Nano Energy* **2019,** *60*, 247-256.
77. Bocan, K. N. & Sejdić, E. Adaptive transcutaneous power transfer to implantable devices: A state of the art review. *Sensors (Switzerland)* **2016,** *16*, 393.
78. Niu, S. *et al.* A wireless body area sensor network based on stretchable passive tags. *Nat. Electron.* **2019,** *2*, 361-368.
79. Huang, X. *et al.* Stretchable, wireless sensors and functional substrates for epidermal characterization of sweat. *Small* **2014,** *10*, 3083-3090.
80. Bhadra, S.; Bridges, G. E.; Thomson, D. J. & Freund, M. S. Wireless passive sensor for remote pH monitoring. *J. Nanotechnol. Eng. Med.* **2011,** *2*, 2-5.

81. Fonseca, M. A.; English, J. M.; Von Arx, M. & Allen, M. G. Wireless micromachined ceramic pressure sensor for high-temperature applications. *J. Microelectromechanical Syst.* **2002,** *11*, 337-343.
82. Harpster, T. J.; Stark, B. & Najafi, K. A passive wireless integrated humidity sensor. *Sensors Actuators, A Phys.* **2002,** *95*, 100107.
83. Nopper, R.; Has, R. & Reindl, L. A wireless sensor readout system-circuit concept, simulation, and accuracy. *IEEE Trans. Instrum. Meas.* **2011,** *60*, 2976-2983.
84. Grätzel, M. Photoelectrochemical Cells. *Nature* **2001,** *414*, 338-344.
85. O'regan, B., & Grätzel, M. A low-cost, high-efficiency solar cell based on dye-sensitized colloidal TiO_2 films. *Nature* **1991,** *353*, 737-739.
86. Grätzel, M. Dye-sensitized solar cells. *J. Photochem. Photobiol. C Photochem. Rev.* **2003,** *4*, 145-153.
87. Van Kerschaver, E. & Beaucarne, G. Back-contact solar cells: A review. *Prog. Photovoltaics Res. Appl.* **14**, 107–123 (2006).
88. Fu, D.; Li Zhang, X.; Barber, R. L. & Bach, U. Dye-sensitized back-contact solar cells. *Adv. Mater.* **2010,** *22*, 4270-4274.
89. Lindström, H.; Holmberg, A.; Magnusson, E.; Malmqvist, L. & Hagfeldt, A. A new method to make dye-sensitized nanocrystalline solar cells at room temperature. *J. Photochem. Photobiol. A Chem.* **2001,** *145*, 107-112.
90. Yum, J. H.; Kim, S. S.; Kim, D. Y. & Sung, Y. E. Electrophoretically deposited TiO_2 photo-electrodes for use in flexible dye-sensitized solar cells. *J. Photochem. Photobiol. A Chem.* 2005, **173**, 1-6.
91. Yamaguchi, T.; Tobe, N.; Matsumoto, D. & Arakawa, H. Highly efficient plastic substrate dye-sensitized solar cells using a compression method for preparation of TiO_2 photoelectrodes. *Chem. Commun.* **2007,** *45*, 4767–4769.

Chapter 2

Efficient multi-material structured thin film transfer to elastomers for stretchable electronic devices

Reprinted from
Xiuping Ding and Jose M. Moran-Mirabal. "Efficient Multi-Material Structured Thin Film Transfer to Elastomers for Stretchable Electronic Devices." *Micromachines* 13.2 (2022): 334.

Abstract: Stretchable electronic devices must conform to curved surfaces and display highly reproducible and predictable performance over a range of mechanical deformations. Mechanical resilience in stretchable devices arises from the inherent robustness and stretchability of each component, as well as from good adhesive contact between functional and structural components. In this work, we combine bench-top thin film structuring with solvent assisted lift-off transfer to produce flexible and stretchable multi-material thin film devices. Patterned wrinkled thin films made of gold (Au), silicon dioxide (SiO_2), or indium tin oxide (ITO) were produced through thermal shrinking of pre-stressed polystyrene (PS) substrates. The wrinkled films were then transferred from the PS to poly(dimethylsiloxane) (PDMS) substrates through covalent bonding and solvent-assisted dissolution of the PS. Using this approach, different materials and hybrid structures could be lifted off simultaneously from the PS, simplifying the fabrication of multi-material stretchable thin film electronic devices. As proof-of-concept, we used this structuring and transfer method to fabricate flexible and stretchable thin film heaters. Their characterization at a variety of applied voltages and under cyclic tensile strain showed highly reproducible heating performance. We anticipate this fabrication method can aid in the development of flexible and stretchable electronic devices.

Keywords: flexible electronics; wrinkling; shape-memory polymer; lift-off; hybrid structure; multilayer conductive films; wearable electronics

2.1. Introduction

The implementation of stretchable electronics can enable new types of devices for a range of applications, like devices that can integrate with the human body for advanced therapeutic treatment, sensory skins for robotics, and wearable communication devices, which are impossible to achieve with conventional rigid electronics [1]. Flexible and stretchable components are key to the development of such devices for biomedicine, as has been shown in devices for intracardial and neural monitoring as well as human/machine interface integrated circuits [2]. Stretchable electronic devices should be mechanically robust to make it possible to conformally span curved surfaces and movable parts [3,4], and should be able to withstand large strains with no fracture or substantial degradation of their electrical properties [5]. For example, in a humanoid robot, areas covering the shoulders, elbows, and knees should be able to deform to 130–160% of their original dimensions [6]. Thin films have been used to implement stretchable electronic components because when the thickness of a thin film becomes 1/1000 of the desired radii of curvature, the tensile and compressive strains on the film during bending are small and the film becomes flexible and rollable [3,7].

Wrinkled structures, arising from the buckling mechanics of thin films, have been used to fabricate heterogeneous metal-elastomer stretchable electronic devices. The basis of this approach is that a supported thin film responds to an applied strain by buckling due to the stiffness mismatch between the rigid film and the compliant substrate. In such buckled materials, changes in amplitude and wavelength can occur reversibly when they are stretched or compressed [8]. For example, buckles with uniform 20–50 μm wavelengths have been created by thermally expanding a PDMS substrate, depositing a gold film by e-beam evaporation, and cooling down the system after gold deposition [9]. Similarly, stretchable, and foldable silicon circuits have been fabricated by transferring the circuits from silicon-on-insulator wafer carrier substrates onto PDMS. In this approach, poly(methyl methacrylate) was spin coated as a sacrificial layer before the fabrication of the circuit arrays, and this layer was subsequently dissolved to release the ultrathin, flexible circuits during the transfer process [10].

The wrinkling of gold films by shrinking shape memory polymer substrates has been shown as an alternative cost-effective and simple method to make highly conductive stretchable electrodes. In this fabrication approach, thin gold films are deposited onto a shape-memory polymer substrate (e.g., polystyrene—PS) that is subsequently thermally shrunk [11], resulting in wrinkled thin films that can then be transferred from the rigid substrate to an elastomer like PDMS or Ecoflex [12,13]. In one example of this approach, the thin film transfer was done by dissolving a sacrificial photoresist layer under the gold film, manually lifting off the wrinkled film from the substrate, and depositing it onto partially cured PDMS. The advantage of a lift-off approach is that the photoresist layer can be quickly dissolved using acetone leaving behind minimal residues. A limitation of this method was the size of the transferred devices, as smaller, more fragile thin structures or thin films are difficult to transfer by hand without damage. A second method has been reported that avoids the use of a sacrificial layer and can faithfully transfer thin films patterned into complex shapes with small dimensions [12]. In this approach, the surface of a wrinkled gold film is treated with a solution of (3-mercaptopropyl)trimethoxysilane (MPTMS) to form a self-assembled monolayer that can covalently bond the film with a silicone elastomer mixture that is poured directly on top of it and cured. Through this method, highly stretchable wrinkled gold thin film electrodes were successfully fabricated. However, only a single layer gold film transfer was demonstrated, which limits the application of this method to more complex electronic devices and arrays, as many electronic devices are made in the form of multilayer composites.

In this work, we present two solvent-assisted lift-off methods for the transfer of various wrinkled thin film materials and multilayer structures from rigid PS substrates to elastomeric substrates. The process begins with the fabrication of structured thin films by shrinking thin films deposited onto pre-stressed PS sheets. The wrinkled films are then treated by plasma oxidation or through the formation of a self-assembled monolayer, which promotes the covalent binding of the thin films to a PDMS elastomer that is cast on top and cured. Finally, either the sacrificial layer is dissolved, or the PS substrate is swelled and partially dissolved to remove the film/PDMS from the rigid PS

substrate. These methods are simple and effective ways of fabricating composite structures for stretchable electronic devices. They can reliably transfer complex patterns of materials, and different architectures with varied dimensions. The ability to transfer complex multi-material composites can open the door to applications that require stretchable electrodes, dielectric, and semiconductor components. It can also solve interconnect problems, which are one of the key challenges for wearable electronic devices and arrays [14].

As proof-of-concept of this fabrication approach, we have implemented Au and ITO/Au/ITO stretchable resistive heaters and characterized their response to applied voltage and strain. Both types of heaters show fast heating response, high robustness, and remarkable resilience through stretching and relaxation cycles. This type of stretchable heater can address the need for portable, comfortable, functional materials for physiotherapy, where thermal therapy is frequently used to alleviate joint pain caused by obesity, aging, or workplace injuries [15]. Thin film wearable heaters with high mechanical robustness and good Joule heating performance can be used to overcome the mechanical rigidity and weight of current heat packs or wraps used for this method of therapeutic care. We anticipate that the fabrication of stretchable electronic devices through solvent-assisted lift-off and transfer of composite wrinkled thin films can be a simple and cost-effective way to producing highly stable and stretchable wearable electronics. The films of Au, ITO, SiO2 were made by the fabrication procedure described and transferred with no sacrificial layer.

2.2. Materials and Methods

2.2.1. Wrinkled Thin Film Fabrication

PS sheets (Graphix shrink film, Graphix, Maple Heights, OH, USA) were cut to desired sizes and cleaned by immersing them in isopropanol, ethanol, and 18.2 MΩ cm water (obtained from a Milli-Q Reference A+ Water Purification System, Millipore, Molsheim, France, subsequently referred to simply as “water”) bath sequentially and washing them on an orbital shaker (MAXQ 2000, Thermo Fisher Scientific, Waltham, MA, USA), for 5 min for each solvent. The PS sheets (shape memory polymer) used in

this work are commercially available and biaxially pre-stressed. As a result, the side length of a PS sheet can be shrunken to 40% of its original size by simply heating the substrate above the glass transition temperature. Mask stencils were created by cutting self-adhesive vinyl (FDC-4300, FDC graphic films, South Bend, IN, USA) with a Robo Pro CE5000-40-CRP cutter (Graphtec America Inc., Irvine, CA, USA) to create the desired patterns for different devices. The self-adhesive vinyl stencil was then applied onto the clean PS substrates. For the samples lifted off with a sacrificial layer, positive photoresist (Microposit S1805, Shipley, Marlborough, MA, USA) was spin coated onto the masked PS substrate at 3000 RPM for 30 s and baked at 90 °C for 3 min to remove the solvent in the photoresist. The thickness of the spin-coated photoresist was measured with a surface profilometer (Tencor Alpha Step 200, KLA Corp., Milpitas, CA, USA). Thin films were deposited onto masked PS substrates by sputtering using a Torr Compact Research Coater CRC-600 manual planar magnetron sputtering system (New Windsor, NY, USA). A 99.999% purity gold target (LTS Chemical Inc., Chestnut Ridge, NY, USA), SiO_2 target (Bayville Chemical Supply Company Inc., Deer Park, NY, USA), and ITO target (LTS Research Laboratories, Inc., Orangeburg, NY, USA) were used to deposit thin films of the respective materials. Gold films were sputtered using a DC (direct current) gun, and SiO_2 and ITO films were deposited by RF (radio frequency) gun. After peeling off the vinyl mask, the PS substrate with deposited films were heated in an oven at 130 °C for 5 min to induce biaxial shrinking and flatted on a silicon wafer by annealing at 160 °C for 10 min.

2.2.2. Lift-Off of Wrinkled Films from PS to PDMS

All samples with a gold film as the interface to be transferred to the elastomer were immersed in 5 mM (3-Mercaptopropyl) trimethoxysilane (MPTMS) (95% MPTMS, Sigma-Aldrich, MO, USA) aqueous solution for 1 h, rinsed with water and dried with nitrogen gas. Samples with SiO_2/ITO films interfacing the elastomer were treated using a Harrick High Power Plasma Cleaner (PDC, Harrick Plasma Inc., Ithaca, NY, USA) for 1 min at high power (30 W). At the same time, the base of PDMS and curing agent (Sylgard 184 silicone elastomer kit, Dow Corning Corporation, Corning, NY, USA) were fully mixed in a 10:1 mass ratio and degassed in a desiccator with a mechanical

vacuum pump until air bubbles were removed. The degassed PDMS was cast onto the surface-treated structured films, then put in an oven at 60 °C for 4 h to be cured.

The cured PDMS was cut with a blade to expose the edges of PS substrate. Samples with and without photoresist were put into crystallization dishes with acetone and washed on an orbital shaker at 100 RPM. The photoresist was dissolved in acetone for approximately 1 h, at which point the PS substrate detached from the film/PDMS. For samples without a photoresist layer, the PS substrate was detached by swelling and softening PS in acetone for approximately 6 h, at which point the wrinkled thin films could be manually detached from the softened PS due to the strong chemical bonding between film and PDMS. However, a small amount of PS residue was visible on the surface of transferred films using this direct transfer method without photoresist. The PS residue was then removed by gently rinsing with toluene. The samples were then placed in the vacuum to extract excess solvent. Although toluene is effective at removing PS residues, the PDMS also swelled significantly in this solvent and PS residues were observed via SEM on samples with short toluene rinsing times.

2.2.3. Fabrication of Stretchable Thin Film Heaters

The stretchable heater is comprised of conductive pads made of 50 nm-thick Au films, and heating elements made of 50 nm-thick Au films or 5 nm-thick ITO/50 nm-thick Au/5 nm-thick ITO composite films. Single deposition was conducted for the Au heater; for the ITO/Au/ITO heaters, both ITO layers were deposited on the heating element area, and Au was deposited on the whole area. The thin films were deposited onto pre-stressed PS substrates, and subsequently heated in an oven to shrink the sample and produce wrinkled films as described in Section 2.1. The transfer process used was the same as the procedure described in Section 2.2.

2.2.4. Characterization of Stretchable Thin Film Heaters

To characterize the thermal and mechanical properties of the two types of thin film heaters, voltage was supplied by a source meter (2450 Source Meter, Keithley, Tektronix Inc., Solon, OH, USA). Thermal compound (ARCTIC MX-4, ARCTIC Ltd.,

Brunswick, Germany) was placed onto the heating element to absorb the heat and a thermocouple (T1 thermocouple, MS-6514 Thermometer, MASTECH-Group, Dongguan, China) was used to measure the temperature of the thermal compound. A home-built stretcher with the ability to control the stretch step and stretch distance was used to apply the external strain. The wires of the thermocouple were fixed onto a lab jack to ensure that the thermocouple would be reliably inserted into the thermal paste.

The morphology of the thin films was characterized by scanning electron microscopy (SEM) imaging (JSM-7000F, JEOL Ltd., Tokyo, Japan), with a 10.0 kV acceleration voltage.

2.3. Results and Discussion

2.3.1. Thin Film Transfer with and without a Sacrificial Layer

Two solvent-assisted methods to transfer wrinkled thin films onto elastomeric substrates, one with a sacrificial layer and another without, were compared to evaluate the advantages and disadvantages of each approach. Figure 2.1 shows a schematic representation of the two processes tested to transfer wrinkled thin films (A and B) as well as a photo of sample patterned films transferred onto PDMS (C). Figure 2.1A shows the transfer process with a sacrificial layer of photoresist. To transfer the film with a sacrificial layer, a 400 nm-thick photoresist layer was spin-coated onto vinyl-masked PS prior to gold film deposition. The addition of the photoresist layer increased the wrinkle size compared to wrinkles formed on 20 nm-thick gold films deposited directly onto the PS substrate. This is because the wavelength of the wrinkles is proportional to the combined thickness of the stiff film and the sacrificial layer, and because the sacrificial layer can soften and flow during the shrinking process [11,16,17].

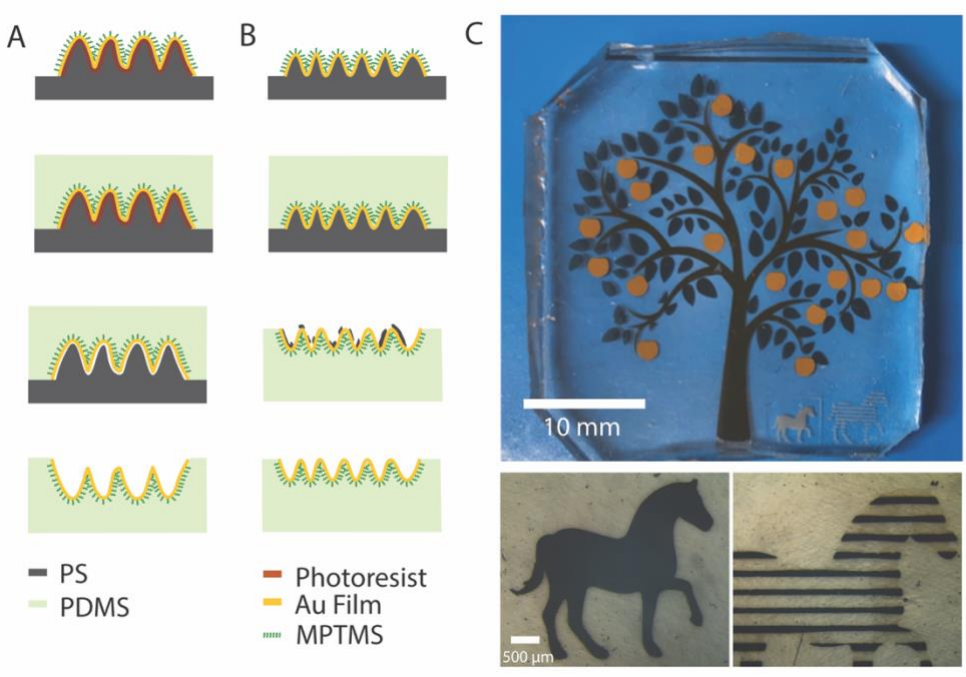

Figure 2.1. Schematic of two solvent-assisted processes to transfer wrinkled films from PS to PDMS. (**A**) Shrunken electrode with photoresist underneath as sacrificial layer. The surface of the wrinkled thin film was treated with MPTMS, and PDMS was cast onto the treated films and cured. The sacrificial layer was dissolved in acetone, completing the transfer of the wrinkled thin film to PDMS. (**B**) Shrunken electrode with no sacrificial layer on PS substrate. The surface of the wrinkled thin film was treated with MPTMS and PDMS was cast onto the treated films and cured. Incubation in acetone was used to swell and partially remove the PS, unavoidably leaving some residues on the wrinkled surface. Washing with toluene was then used to remove the residues. (**C**) Thin films transferred onto PDMS with different compositions and thicknesses form an apple tree and horse scene: trunk-5 nm ITO/5 nm Au/5 nm ITO, leaves-1.3 nm ITO/1.3 nm Au/1.3 nm ITO, apples-50 nm Au, horses-20 nm SiO_2.

A strong bond between the thin films and the elastomeric substrates is essential to impart the robustness and reliability needed for stretchable electronics. However, the bare gold film interacts very weakly with PDMS. To ensure strong adhesion between the wrinkled thin film and the elastomer, MPTMS was used to functionalize the gold surface. MPTMS is a molecular adhesion promoter that can form self-assembled monolayers and has two types of terminal groups with different functionalities. The

three methoxy (-OCH3) groups can covalently bind to the surface of PDMS and the thiol (-SH) can bond to the gold surface. Thus, when a PDMS base and crosslinker mixture was cast onto the functionalized surface of the shrunken electrode and cured at 60 °C for 4 h, the two materials became strongly bonded. Once the elastomer was cured, it was cut along the edge of the PS to expose the PS/PDMS interface. The PS with cured PDMS was then immersed in an acetone bath to dissolve the photoresist between the wrinkled Au film and the PS. The wrinkled films could be fully lifted off from the PS after only 1 h in acetone, while remaining adhered to the PDMS.

Figure 2.1B illustrates the transfer process that involves no sacrificial layer. In this example, a 20 nm-thick Au film was directly sputtered onto a PS substrate. In contrast to Figure 2.1A, the wavelength of the bare Au film (<1 μm) is much smaller than that of the 20 nm-thick Au film with a layer of photoresist (~4 μm). The wrinkled Au surface was also functionalized with MPTMS and PDMS was cast and cut using the same procedure as above. The cured sample of PS/Au/PDMS was put in an acetone bath for ~6 h. During this time, the PS substrate softened and swelled, and could be removed from the PDMS substrate. However, because of the softening of the PS, residue was left on the surface of the Au film. Since PS is more readily solubilized in toluene than acetone, as a last step, toluene was used to remove residue on the surface of the wrinkled film. Many toluene rinsing steps (~40) were needed to ensure that the rough wrinkled surface was devoid of any PS residue. Although toluene is useful to remove residual PS from the Au films, it causes swelling of PDMS by ~30% [18]. Swelled PDMS is, however, capable of shrinking back to its original dimensions by being extracted the solvent in a vacuum oven at 60 °C. The swelling introduced about 5% strain onto the wrinkled film and no cracks or delamination were observed on the transferred films.

To showcase the potential of transferring electronic devices with complexity by one of the methods described above, a pattern comprised of various materials in different shapes and layout was transferred. Figure 2.1C shows structured films transferred to PDMS made from various material layers and with different thicknesses: trunk of the apple tree-5 nm ITO/5 nm Au/5 nm ITO, leaves-1.3 nm ITO/1.3 nm Au/1.3 nm ITO, apples-50 nm Au, horses-20 nm SiO_2. In addition to different film thicknesses

and compositions, the pattern transferred is complex and shows dimensions across different scales, from the base of the tree representing a couple millimeters and the stripes of the horse being ~120 μm in width. These films were transferred simultaneously and with no sacrificial layer, demonstrating the ability of this method to transfer different materials, hybrid structures, and multiscale complex patterns. This method is thus straightforward and high-fidelity, enabling the fabrication of stretchable thin film devices comprised of different materials and hybrid structures.

Both transfer methods have advantages and disadvantages based on the simplicity of the process and fidelity of the transferred patterns. The method using a sacrificial photoresist layer is simpler and more efficient, involving only the direct dissolution of photoresist with acetone, with no PS residue observed via SEM. However, the wavelength of the wrinkles is much larger compared to that of samples with similar Au film thickness transferred with the method devoid of photoresist. Figure 2.2A shows the surface topography of a 20 nm-thick gold wrinkled film transferred onto PDMS with a sacrificial layer. The increase in wrinkle size arises primarily from the greater combined film thickness (~400 nm for Au + photoresist versus 20 nm for Au only) as previously mentioned. The transfer process without sacrificial layer is longer and requires an extra toluene rinsing step to remove PS residue after the acetone bath. The residue, which can be seen in Figure 2.2B, fills the valleys on the wrinkled surface after removing the softened PS, but can be effectively eliminated with toluene (Figure 2.2C shows the same sample as Figure 2.2B after toluene rinsing). Therefore, the transfer method can be selected depending on the material requirements and the desired application. With the sacrificial layer, the transfer is fast and requires less post-transfer cleanup, but produces larger wrinkles whereas without the sacrificial layer, the transfer requires more time and an extra toluene rinsing stage, however the result is smaller wrinkled features. Each transfer method could prove useful depending on the requirements of roughness (wrinkle size), tolerance to PS residue and swelling, and compatibility with toluene for the stretchable electronic device.

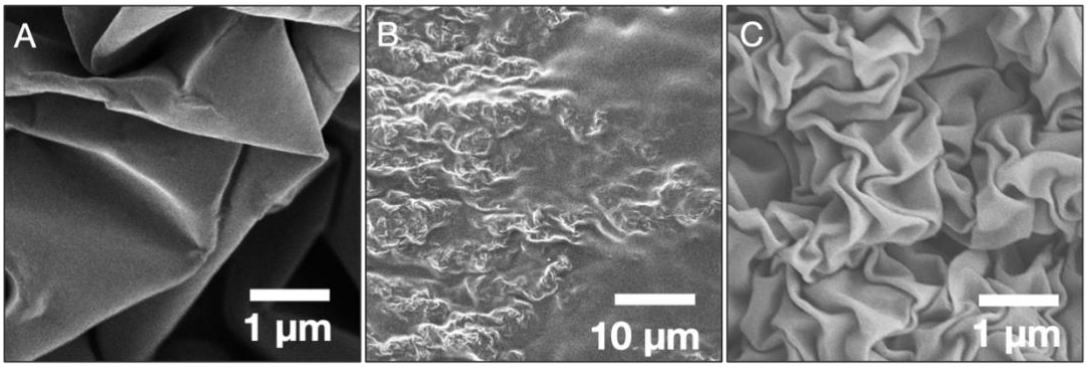

Figure 2.2. SEM images show the differences arising from of the two transferring methods. (**A**) Topography of a 20 nm-thick Au wrinkled film transferred onto PDMS using a sacrificial photoresist layer. Topography of a 20 nm-thick wrinkled gold film transferred without photoresist onto PDMS (**B**) with polystyrene residue after the acetone bath step and (**C**) after rinsing with toluene.

2.3.2. Multi-Material Thin Film Transfer

Most stretchable thin film devices or integrated circuits require the incorporation of multiple materials into layers with dimensions going from the macro to the microscale and functions ranging from conductor to dielectric. Therefore, it is essential that transfer methods can accommodate different materials and structures simultaneously. This would significantly simplify stretchable electronic device fabrication, achieve better adhesion between the different layers, and solve interconnection problems between different parts of the device, as well as prove useful for the fabrication of large area wearable electronic arrays.

To this end, we tested the ability of the direct transfer method to transfer composite layered thin films. SEM images of flat and wrinkled 5 nm ITO/5 nm Au/5 nm ITO film on PS substrates are shown in Figures 2.3A and 3C, respectively. The same films transferred onto PDMS are shown in Figures 2.3B and 3D, respectively. When measuring the resistance of transferred films, wrinkled films on PDMS showed the same values as on the rigid PS substrate. On the other hand, the transferred flat films (Figure 2.3B) were not electrically conductive due to extensive cracking. Both the morphology and electrical measurements suggest that the wrinkled structures make the thin film

more tolerant to the strain applied during the transfer process. Figure 2.3C, D (ITO/Au/ITO films), along with Figure 2.3E, F (20 nm-thick SiO_2 on PS and PDMS), highlight the potential of this method for transferring multilayer, high modulus, and low fracture toughness wrinkled films from PS to PDMS. This will bring real benefit to the development of stretchable thin film electronic devices because most devices incorporate specific architectures composed of conductor, dielectric, and insulator materials. The one-time transfer will simplify the fabrication of stretchable devices and circuits, and significantly improve the bonding between different films. Moreover, the wrinkles increase the tolerance of modulus films to external strain during the fabrication, as shown by the comparison between Figure 2.3B, D.

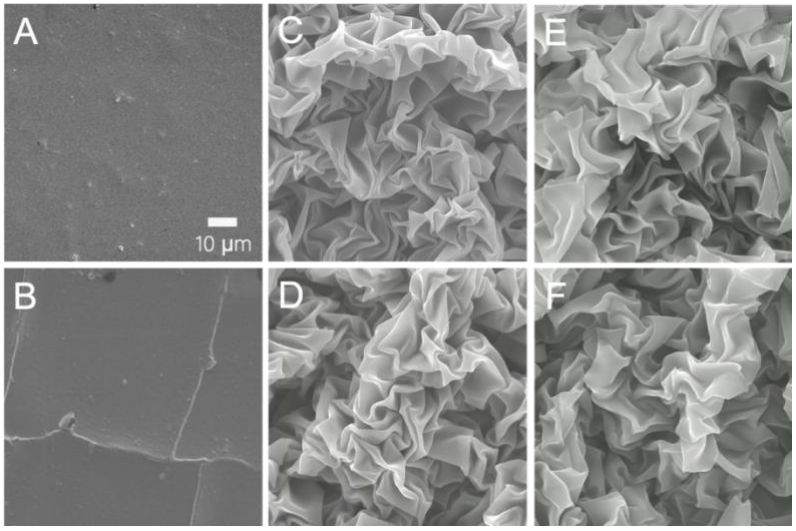

Figure 2.3. Surface topography of 5 nm ITO/5 nm Au/5 nm ITO multilayer films and 20 nm SiO_2 films on PS and PDMS substrates. (**A**) Flat ITO/Au/ITO film on PS. (**B**) Flat ITO/Au/ITO film transferred onto PDMS. (**C**) Wrinkled ITO/Au/ITO film on PS. (**D**) Wrinkled ITO/Au/ITO film on PDMS. (**E**) Wrinkled 20 nm SiO_2 on PS. (**F**) Wrinkled 20 nm SiO_2 on PDMS.

2.3.3. Stretchable Thin-Film Heaters

As proof-of-concept of the fabrication of stretchable devices through solvent-assisted transfer of structured thin films, stretchable thin film heaters were fabricated.

Two types of heaters were built: heaters with a single layer of Au and heaters with multiple layers, composed of ITO/Au/ITO. The heaters were made containing a resistive heating pad (3 × 1.5 cm) and two small contact pads (0.5 × 0.5 cm). To characterize the mechanical and thermal properties of the stretchable heaters, thermal paste was applied on the surface of the resistive heating element, and the temperature of the thermal paste was monitored for various applied input voltages (Figure S2.1). The temperature vs. time profile for Au heaters under various applied voltages (0.2–1.7 V) over 420 s is shown in Figure 2.4A. At first the temperature of the thermal paste increases rapidly, especially during the first 60 s, then slows down and reaches a plateau (or stable temperature) within 100–200 s. Within the first 60 s, the temperature increases almost linearly, with heating rates for Au heaters of 0.25 °C/s and 0.70 °C/s under a bias of 1.0 V and 1.7 V, respectively. When the input voltage is below 1 V, the plateau temperature is reached faster than with higher applied voltages, as expected from the smaller change in temperature from room temperature. From the temperature-time profile the temperature of the heater could reach and maintain a stable temperature within minutes.

To investigate the stretchability of the structured Au film resistive elements, the heater was operated under various applied tensile strains at constant voltage and the plateau temperatures were measured. This was repeated for various applied voltages and the results are summarized in Figure 2.4B, C. The plot of temperature vs. strain (Figure 2.4B) shows mostly uniform horizontal lines for every applied voltage, indicating that Joule heating is stable when the heater is stretched. Figure 2.4B was plotted by obtaining the plateau temperature under different voltages, while the thin film heaters were stretched at different strains. For example, the temperature at 0 % strain was recorded by performing the measurement as shown in Figure 2.4A and measuring the temperature at 420 s. Figure 2.4C shows the same data, but now presented as a temperature vs. voltage plot. In this plot, it can be clearly observed that the heater presents a non-linear, quadratic (Figure S2.2), response to voltage. This functional dependence is maintained even at different applied strains, although higher voltages (higher temperatures) produce higher variability. This is expected as the heat can be

quickly dissipated and small changes in the conductivity of the heating element can have a strong influence on the recorded temperature. It is worth noting that the temperatures recorded for strains at 5% show a slightly higher temperature compared to the temperature recorded under no applied strain. This can be explained by the way the stretchable heater is fixed in the stretching setup; when the thin film on the PDMS substrate was fixed on the stretcher and the screws that clamped the substrates were tightened, the PDMS substrate was squeezed, causing the film to undergo a small amount of compressive bending. The film was subsequently flattened during stretching, which means that the 0% strain state resulted in a slightly bent film and 5% strain state more accurately represented a relaxed "0% strain" state. To further check the temperature reproducibility, on-off cycles were applied to the heaters every 60 s under an applied voltage of 1.5 V (Figure 2.4D). The thin film heaters showed highly reproducible behavior, reliable performance, and fast heating response as indicated by the uniformity of the on/off response curve.

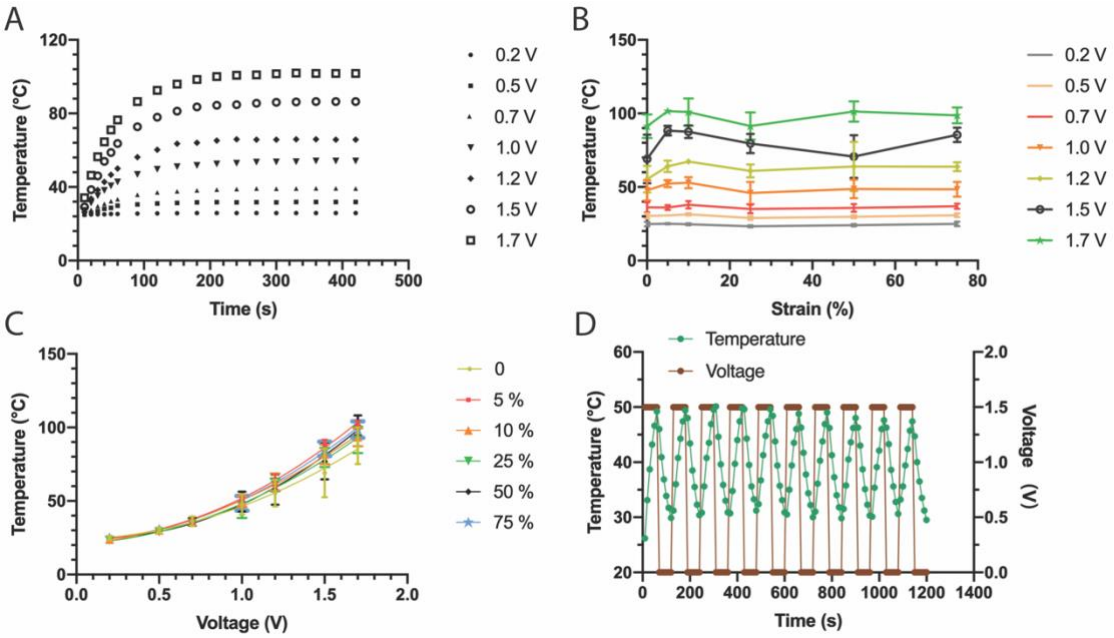

Figure 2.4. Characterization of stretchable Au heaters. (**A**) Temperature profiles under varying applied voltage (0.2–1.7 V). (**B**) The plateau temperature changes with various voltages but remains similar for any given voltage under different strains. (**C**) Changes in temperature vs. voltage for various applied strains (each series corresponds to an applied strain). (**D**) Cycling

on/off response under an applied voltage of 1.5 V shows the reproducibility of the heating and cooling cycles.

To investigate the applicability of our solvent-assisted transfer fabrication of resistive heaters to composite ceramic/metal multilayered films, ITO/Au/ITO thin film heaters were fabricated and characterized. Although the heating element is comprised of ITO/Au/ITO multilayers, the contact pads were directly connected to the central Au heating layer. This fabrication step is very important to prevent the heater from burning because of a high contact resistance that could lead to overheating of the contact area. The composite thin film heaters were characterized in the same way as the Au heaters described above. Overall, similar thermal and mechanical characteristics were observed as with the Au heaters (Figure 2.5): fast and reproducible heating kinetics, excellent stretchability, and no noticeable deterioration over on/off cycling. However, some minor differences were observed between the two types of heaters. The temperature-time profile of composite heaters (Figure 2.5A) shows a slightly lower stable temperature and slower heating rate for each applied voltage. The temperature increases at a rate of 0.20 °C/s and 0.55 °C/s under 1.0 V and 1.7 V, respectively. This difference is attributed to the difference in heat transfer between the central Au resistive layer and the 5 nm ITO layer, which ultimately limits heat transfer to the thermal paste. The temperature versus strain profiles (Figure 2.5B, C) indicate that the multilayer thin film heaters have slightly less reproducibility as evidenced by the larger error bars obtained from replicate devices, especially at higher applied voltages. The lower reproducibility of the multilayer heaters at higher voltages could be caused by the two 5 nm ITO layers that are more brittle and could lead to some cracking during the stretching process.

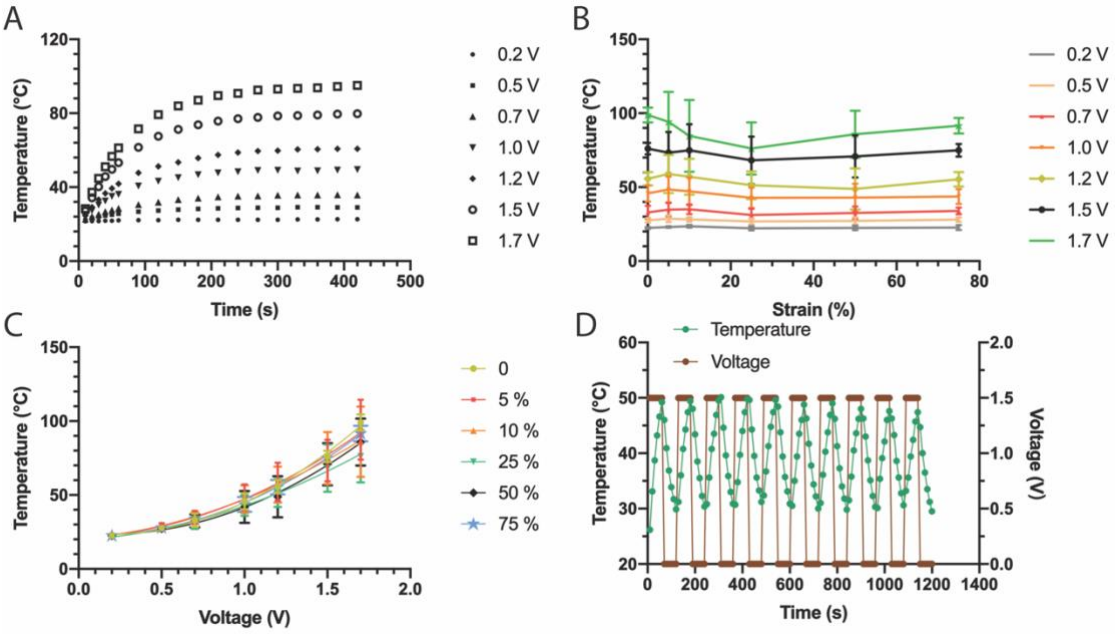

Figure 2.5. Characterization of stretchable ITO/Au/ITO heaters. (**A**) Temperature profiles under varying applied voltage (0.2–1.7 V). (**B**) The plateau temperature changes with various voltages but remains similar for any given voltage under different strains. (**C**) Changes in temperature vs. voltage for various applied strains (each series represents a given strain value). (**D**) Cycling on/off response under an applied voltage of 1.5 V shows the reproducibility of the temperature reached at the plateau.

It is worth mentioning that the ITO/Au/ITO multilayer heater is representative of an electronic device with a hybrid structure incorporating various materials (metal and ceramic); together with the contact pads which interconnect with other components, they comprise a unit cell that can be integrated into an array or a more complex circuit. This fabrication approach can be further extended to encompass other device components like resistors, capacitors, inductors, transistors, and even a hybrid network of them can be realized. The simultaneous transfer of multiple device components would also address interconnection issues that arise for stretchable electronic arrays, leading to improved long-term stability.

2.4. Conclusions

This work demonstrates a method for the fabrication of thin film stretchable devices by solvent-assisted transfer of wrinkled thin films from rigid substrates to elastomeric PDMS. Wrinkled thin films were obtained by shrinking flat films patterned on and supported by a shape memory polymer. The transfer process involves modifying the surface of the wrinkled film with an adhesion promoter that forms a chemical bond between PDMS and the film, and the subsequent release of the structured film through dissolution of a sacrificial layer or softening of the PS substrate. Structured films transferred using these two approaches were characterized and compared. The solvent-assisted transfer process ensures the faithful transfer of the wrinkled structures with millimeter to micrometer dimensions in the stretchable devices.

A proof-of-concept application was demonstrated by fabricating and characterizing stretchable thin film Au and ITO/Au/ITO multilayer stretchable heaters. The fabrication of highly stretchable heaters is simple, and since the connection pads and the heating elements were already overlayed, the transfer approach results in very strong adhesion between all elements of the heater. To measure thermal properties and stretchability of the heaters, the temperature of thermal paste in contact with the heaters was monitored at various applied strains and voltages. The results show that both types of stretchable thin films have rapid Joule heating kinetics, and the temperature can reach more than 50 °C with only 1 V of applied voltage. The heaters also displayed high stretchability with nearly constant performance even at 75% applied strain, and high reproducibility when subjected to on/off duty cycles. Overall, the transfer process is a simple and effective method for fabricating hybrid materials and structures for stretchable electronic devices.

Funding: X.D. was partially supported through a China Scholarship Council doctoral award. J.M.-M. is the Tier 2 Canada Research Chair in Micro and Nanostructured Materials and the recipient of an Early Researcher Award from the Ontario Ministry of Research and Innovation. This work was supported by funding through a Discovery Grant from NSERC and a Canadian Foundation for Innovation J.E.L.F. instrumentation grant to J. M.-M. (RGPIN-2019-06433). This research made use of instrumentation within McMaster's Canadian Centre for Electron Microscopy.

Acknowledgments: The authors thank Yujie Zhu for instrument training and Zhilin Peng for help with SEM imaging.

References

1. Rogers, J.A.; Someya, T.; Huang, Y. Materials and mechanics for stretchable electronics. *Science* **2010**, *327*, 1603–1607.
2. Rogers, J.A.; Huang, Y. A curvy, stretchy future for electronics. *Proc. Natl. Acad. Sci. USA* **2009**, *106*, 10875–10876.
3. Wagner, S.; Bauer, S. Materials for stretchable electronics. *MRS Bull.* **2012**, *37*, 207–213.
4. Sekitani, T.; Someya, T. Stretchable organic integrated circuits for large-area electronic skin surfaces. *MRS Bull.* **2012**, *37*, 236–245.
5. Kim, D.H.; Rogers, J.A. Stretchable electronics: Materials strategies and devices. *Adv. Mater.* **2008**, *20*, 4887–4892.
6. Silvera-Tawil, D.; Rye, D.; Velonaki, M. Artificial skin and tactile sensing for socially interactive robots: A review. *Rob. Auton. Syst.* **2015**, *63*, 230–243.
7. Suo, Z.; Ma, E.Y.; Gleskova, H.; Wagner, S. Mechanics of rollable and foldable film-on-foil electronics. *Appl. Phys. Lett.* **1999**, *74*, 1177–1179.
8. Jiang, H.; Khang, D.-Y.; Song, J.; Sun, Y.; Huang, Y.; Rogers, J.A. Finite deformation mechanics in buckled thin films on compliant supports. *Proc. Natl. Acad. Sci. USA* **2007**, *104*, 15607–15612.
9. Bowden, N.; Brittain, S.; Evans, A.G.; Hutchinson, J.W.; Whitesides, G.M. Spontaneous formation of ordered structures in thin films of metals supported on an elastomeric polymer. *Nature* **1998**, *393*, 146–149.
10. Kim, D.H.; Ahn, J.-H.; Choi, W.M.; Kim, H.-S.; Kim, T.-H.; Song, J.; Huang, Y.Y.; Liu, Z.; Lu, C.; Rogers, J.A. Stretchable and foldable silicon integrated circuits. *Nature* **2008**, *320*, 507–511.
11. Fu, C.C.; Grimes, A.; Long, M.; Ferri, C.G.L.; Rich, B.D.; Ghosh, S.; Ghosh, S.; Lee, P.; Gopinathan, A.; Khine, M. Tunable nanowrinkles on shape memory polymer sheets. *Adv. Mater.* **2009**, *21*, 4472–4476.
12. Kim, J.; Park, S.-J.; Nguyen, T.; Chu, M.; Pegan, J.D.; Khine, M. Highly stretchable wrinkled gold thin film wires. *Appl. Phys. Lett.* **2016**, *108*, 061901.
13. Zhu, Y.; Moran-Mirabal, J. Highly bendable and stretchable electrodes based on micro/nanostructured gold films for flexible sensors and electronics. *Adv. Electron. Mater.* **2016**, *2*, 1500345.
14. Lacour, S.P.; Jones, J.; Wagner, S.; Li, T.; Suo, Z. Stretchable interconnects for elastic electronic surfaces. *Proc. IEEE* **2005**, *93*, 1459–1467.
15. Choi, S.J.; Park, J.K.; Hyun, W.; Kim, J.; Kim, J.; Lee, Y.B.; Song, C.; Hwang, H.J.; Kim, J.H.; Hyeon, T.; et al. Stretchable heater using ligand-exchanged silver nanowire nanocomposite for wearable articular thermotherapy. *ACS Nano* **2015**, *9*, 6626–6633 .
16. Genzer, J.; Groenewold, J. Soft matter with hard skin: From skin wrinkles to templating and material characterization. *Soft Matter* **2006**, *2*, 310–323.
17. Stimpson, T.C.; Osorio, D.A.; Cranston, E.D.; Moran-Mirabal, J.M. Direct comparison of three buckling-based methods to measure the elastic modulus of nanobiocomposite thin films. *ACS Appl. Mater. Interfaces* **2021**, *13*, 29187–29198.
18. Lee, J.N.; Park, C.; Whitesides, G.M. Solvent compatibility of poly(dimethylsiloxane)-based microfluidic devices. *Anal. Chem.* **2003**, *75*, 6544–6554.

Appendix A: Chapter 2 Supplementary Information

Efficient Multi-Material Structured Thin Film Transfer to Elastomers for Stretchable Devices

Xiuping Ding, Jose Moran-Mirabal

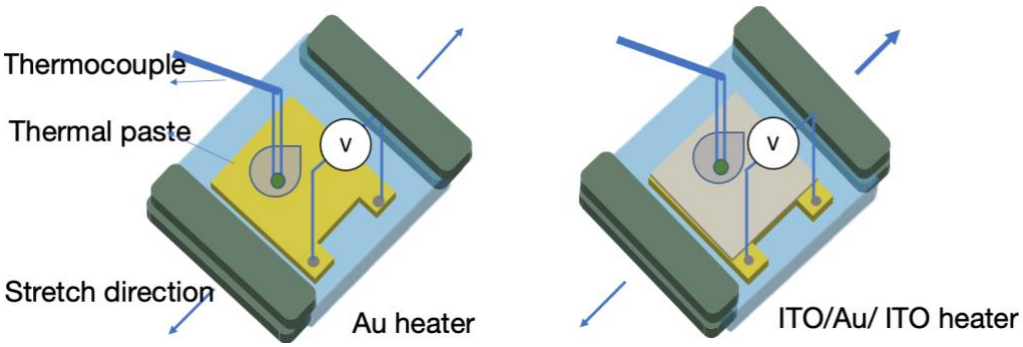

Figure S2.1. Schematic of the characterization of stretchable Au heaters and ITO/Au/ITO heaters

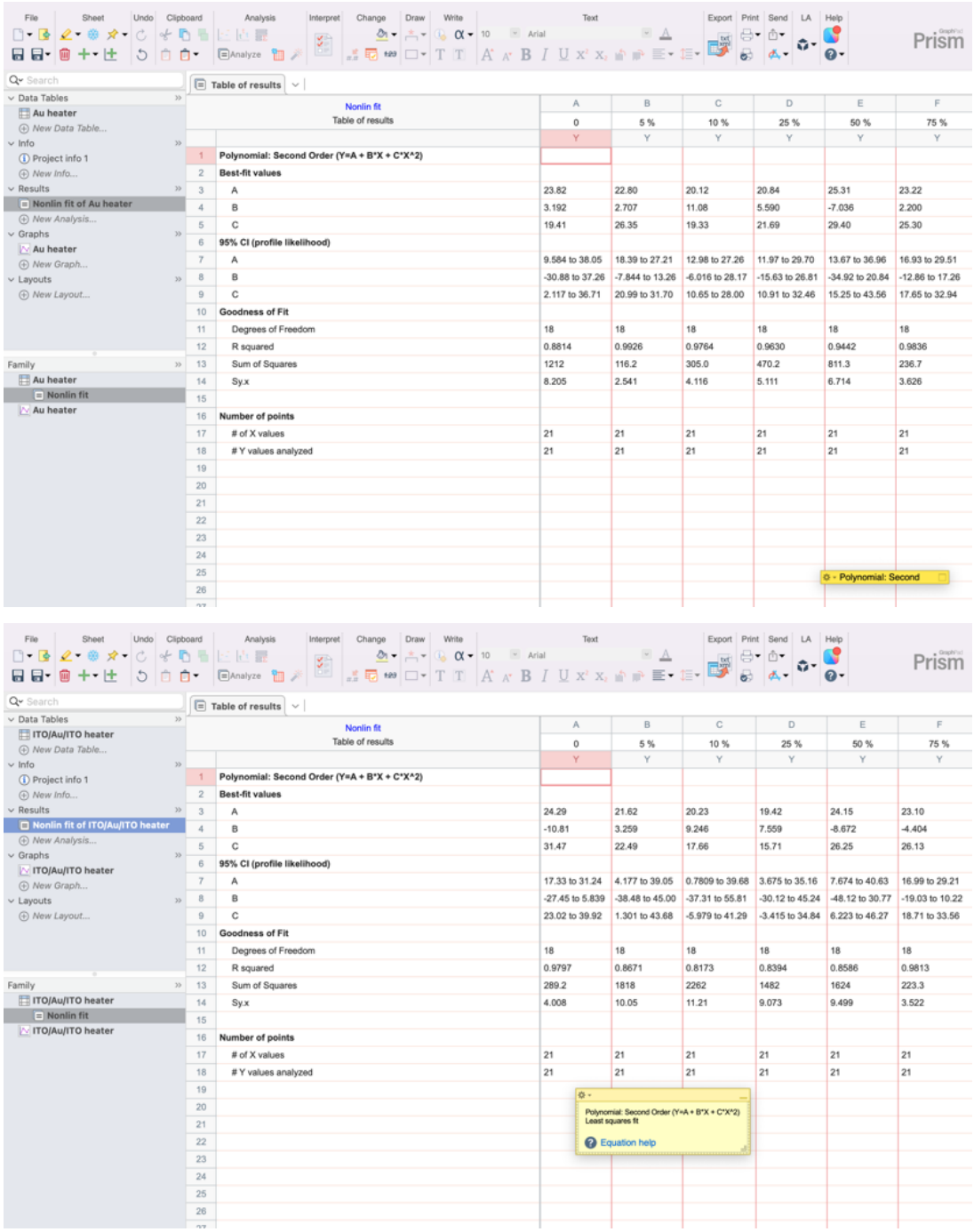

Figure S2.2. Non-linear regression performed shows quadratic fit in figure 4c and figure 5c for stretchable Au heaters and ITO/Au/ITO heaters

Chapter 3

Fabrication of corrosion resistant stretchable multilayer electrodes

Xiuping Ding, Jose M. Moran-Mirabal

Abstract: Stretchable thin film electronics are attractive because they offer a path to wearable biombiomedical devices. Soft, stretchable electronics should conform to the curved surfaces of biological skin and tissue and offer robust mechanical and electrical performance when strained. Conventional flat, rigid electronics cannot satisfy these requirements. A further complication when implementing thin film stretchable electronics *in vivo* is that active sensing electrodes can be constantly exposed to biofluids and environments that can corrode metal electrodes. While some electronics can be encapsulated to avoid electrode damage, other applications require direct contact and transfer of electrons between the sensing electrodes and the *in vivo* environment, like the surface of a tissue. In this work, we present a fabrication approach to create corrosion-resistant stretchable electrodes that integrates indium tin oxide (ITO) or Parylene with wrinkled Au electrodes on soft and stretchable elastomer substrates. Preliminary corrosion-resistance tests showed that flat multilayered Au/ITO and Au/Parylene provided adequate protection while still providing high conductivity, but that wrinkled Au/ITO electrodes were not suitable due to cracking. Therefore, Au/Parylene electrodes were chosen as candidates to produce stretchable electrodes. Au wrinkled electrodes were first fabricated on a pre-stressed polystyrene substrate using a thermal shrinking approach followed by Parylene coating and solvent-assisted thin film device transfer to a receiving PDMS elastomer. The fabrication conditions were carefully optimized by tuning the thickness of Parylene and the deposition/shrinking order to maintain a high level of conductivity through the coating layer while being corrosion resistant. The resulting electrodes exhibited high stretchability (up to 75 %

strain) and excellent corrosion-resistance during operation when exposed to a solution containing I^-/I^{3-} redox couple. This research provides a unique approach for the fabrication of stretchable electrodes that need to be in in contact with corrosive environments, such as tissue and biofluids *in vivo*.

Keywords: Stretchable electronics; Parylene; wrinkles; *in vivo* electrode; biomedical device

3.1. Introduction

The intrinsic mechanical properties of traditional electronic devices, which are rigid and planar, fundamentally hinder their integration with soft and curved biological surfaces, such as those of skin or tissue [1]. As a result, flexible and stretchable electronics that can reliably maintain high levels of performance while conforming to complex surfaces and integrating with the human body are in great demand. With the advent of stretchable electronics, significant advances are expected in disease diagnostics and therapeutics, health monitoring, as well as human-machine interfaces. The potential of stretchable electronics has been shown in works addressing advanced surgical tools [2], implantable sensors [3], retinal prostheses [4,5], and brain-machine interfaces [6,7]. Not only are the soft, light weight properties of stretchable electronics more friendly to tissue and users, but they also offer better coverage and contact with tissue that can enhance the spatial resolution of wearable sensors and devices [8].

An issue that arises with the more intimate contact of wearable devices with a living body is the corrosion that can occur when they come in contact with biofluids, which contain water, anions (e.g., Cl^-, PO_4^{3-}, HCO_3^-), cations (e.g., Na^+, K^+, Ca^{2+}), proteins, and dissolved oxygen. Although under normal physiological conditions the pH in the human body is maintained at 7.4, it can also fluctuate between values of 3 and 9 when biological imbalances develop (such as when the body is subjected to diseases, infections, and surgeries) [9]. In such environments, the uncoated conducting materials of interconnects and electrodes within a stretchable device are susceptible to common

forms of metal corrosion, including uniform corrosion, intergranular, galvanic and stress corrosion cracking, pitting and fatigue corrosion [9]. The application of a voltage bias or current pulse can further increase the risk corrosion, significantly lowering the reliability and shortening usable lifetime of the device [5]. In the case of prostheses and implantable electronics for in vivo use, device failure due to corrosion could mean another invasive surgery on the patient.

A solution to the issue of metal corrosion is to encapsulate the device in an insulating layer that protects it from the biological environment. Encapsulated flexible organic transistors, circuits [10,11], and ultralight weight stretchable organic field-effect transistors [12] have been reported, which were coated using organic/metal/organic or purely organic passivation layers. In these cases, the organic encapsulation layer has been used as a barrier against the diffusion of oxygen and water. Many active conducting components, however, require close contact with the tissue or the fluid physiological environment to effectively record or elicit neural potential or other electrical signals [6,13]. For example, the UTAH electrode array [14], designed to restore neural function and conduct basic neuroscience research, consists of electrode needles encapsulated in a 4.5 μm layer of Parylene. This insulating layer needs to be removed from the active tips of the electrode needles for effective neural recording and stimulation [15]. There is an unmet need to develop stretchable electrodes that can conformally contact biological tissue and maintain a high level of electrical conductivity while being resistant to corrosion and able to endure the biological environment.

In this work, we have combined wrinkled electrodes on polymethylsiloxane (PDMS) elastomer [16–18] with multilayer electrode coatings to address the problem of protecting a stretchable electrode against corrosive environments while maintaining high conductivity through the protecting layer. First, we tested multilayer electrodes composed of a thin metal film sandwiched between transparent indium tin oxide layers (ITO/Au/ITO), a concept originally explored in low-emittance coatings for energy conserving windows [19] that is now being used to develop transparent and flexible electronic devices [20–23]. Within the framework of the multilayer electrode layout, Parylene coatings were introduced to replace the ITO and their thickness was carefully

optimized to ensure high conductivity and corrosion resistance. The order in which the Parylene coating is introduced, and the transfer process were adapted to accommodate the thermal and coating properties of Parylene. The resulting multilayered wrinkled electrodes exhibited strong interlayer adhesion, excellent corrosion-resistance, and high stretchability of up to 75% strain. The method developed to fabricate corrosion-resistant stretchable electrodes has the potential to accelerate the development of stretchable electronics by improving the useful lifetime and the accuracy of the sensing devices designed for implantation in the human body.

3.2. Materials and Methods

3.2.1 Multilayer electrode fabrication

Samples for sheet resistance measurements. Flat multilayered thin film samples for sheet resistance measurements were fabricated on 25 mm × 25 mm microscope cover glass substrates (Fisher Scientific, Pittsburgh, PA, USA) that were first cleaned by successive washing with acetone, isopropanol and 18.2 MΩ cm water (obtained from a Milli-Q Reference A+ Water Purification System, Millipore, Molsheim, France, subsequently referred to simply as "water") and then dried under a dry nitrogen stream. Self-adhesive vinyl stencils (FDC-4300, FDC graphic films, South Bend, IN, USA) patterned by a cutter (Robo Pro CE5000- 40-CRP, Graphtec America Inc., Irvine, CA, USA) were used to mask the cover glass leaving a 15 mm × 15 mm area exposed for film deposition. Cr, Au, and ITO layers were deposited through sputtering with a manual planar magnetron sputtering system (Torr Compact Research Coater CRC-600, Torr international services LLC, New Windsor, NY). A 99.99 % purity of chromium metal target (LTS Research Laboratories, Inc., Orangeburg, NY, USA), a 99.999 % purity gold metal target (LTS Chemical Inc., Chestnut Ridge, NY, USA) and an ITO target (LTS Research Laboratories, Inc., Orangeburg, NY) were used to deposit the Cr, Au, and ITO films, respectively. Cr and ITO films were sputtered using a RF (radio frequency) gun and the Au film was deposited using a DC (direct current) gun. Parylene C was deposited using a chemical vapor deposition coating system (PDS 2010, Specialty Coating System. Inc, Indianapolis, IN, USA). The thickness of Parylene C

films deposited from dimer loadings of 10, 25, and 50 mg were measured using a Variable Angle Spectroscopic Ellipsometer (M-2000UI, J. A. Woollam. Co., Inc., NE, USA) to be ~20, 50, and 100 nm, respectively. For the last step, four contact pads (5 mm × 5 mm) made of 50-nm thick Au were sputtered at the four corners of the square.

Samples for corrosion resistance tests. All multilayer thin films were patterned and deposited as described above, but in addition to glass substrates the films were also deposited onto pre-stressed polystyrene substrates. The shape of the patterned multilayer thin films was bone-shape as shown in Supplementary Information Figure S3.1. The multilayer thin films were wrinkled through thermal shrinking of the underlying polystyrene substrate and transferred onto PDMS as previously described [18]. The samples were shrunken at 130 ˚C, flattened at 160 ˚C, and transferred onto PDMS by solvent-assisted method after functionalizing their surface with MPTMS (3-mercaptopropyl) trimethoxysilane. Depending on the application, the transfer can be done with or without sacrificial layers. Electrodes with 5 nm-thick Au were transferred directly from the PS substrate, while those with 200-nm thick Au were transferred using photoresist as a sacrificial layer.

Samples for stretchability tests. All the samples for mechanical testing were prepared on PS substrates, wrinkled, and transferred to PDMS substrate as describe above. The shape of the patterned multilayer thin films was rectangular, with dimensions 40 mm × 16 mm as deposited, and 16 mm × 6 mm after shrinking.

3.2.2 Sheet resistance measurements

Sheet resistance was measured using a four-point probe arrangement with a source meter (2450 Source Meter, Keithley, Tektronix Inc., Solon, OH, USA). The four probes were connected to the film aided by EGaIn droplets that were placed on the four contacts pads. The four probes were shifted clockwise and four resistances (R1, R2, R3, R4) were obtained. In this case, the film is uniform and square, so the four resistances are equivalent. The sheet resistance and resistivity were the calculated with the formulas:

$$R_s = \frac{\pi}{In2} \times \frac{R_1+R_2+R_3+R_4}{4}, \rho = R_s \times t$$

Where, R_1, R_2, R_3, R_4 are resistances measured for the four sides of the square,

R_s is the sheet resistance in Ω/sq,

ρ is the resistivity in Ω/m,

t is the thickness of the film.

3.2.3 Evaluation of corrosion resistance

Samples were tested for corrosion resistance as shown in Figure S3.1 (Supplementary Information). To conduct the corrosion resistance tests, gaskets were used to confine a volume of I^-/I^{3-} electrolyte (EL-HSE high stable electrolyte, Dyesol, Queanbeyan, NSW, Australia). All flat electrodes and wrinkled electrodes were masked using vinyl stencil gaskets, except for wrinkled electrodes with a 200 nm-thick Au layer, which were masked with PDMS gaskets. The dimensions for the gasket opening where the electrolyte was confined was 5.5 mm × 1 mm for flat electrodes and 2 mm × 1 mm for shrunken wrinkled electrodes. The corrosion resistance tests were carried out under 0.1 V voltage bias applied using the same a source meter (2450 Source Meter, Keithley, Tektronix Inc., Solon, OH, USA), with two probes contacting the EGaIn on the films as shown in the Supplementary Information, Figure S3.1B), and the current was monitored over the duration of the experiment (120-240 s). In all experiments, the droplet of electrolyte (7 µl for flat samples and 3 µl for wrinkled samples) was placed within the gasket at the 15 s mark.

3.2.4 Electrode performance under tensile strain.

Stretching tests were carried out with a homemade stretcher, equipped with a micrometer screw gauge with a resolution of 0.01 mm. Strain was applied at 5% intervals and the sheet resistance of the electrodes was measured using a co-linear four-point probe arrangement. The four-point probe measurement was carried out with a

source meter (2450 Source Meter, Keithley, Tektronix Inc., Solon, OH, USA) using 3 mm spacing between neighboring probes. The probes were rearranged after each strain increase at the center of the sample as shown in Figure S3.3B (Supplementary Information).

3.3. Results and discussion

3.3.1 Evaluation of conductive behaviour of multilayered thin films on glass substrate

The conductivity of the multilayer electrodes was first assessed through sheet resistance measurements to determine their viability as conductive elements. Three groups of samples were fabricated on glass substrates, bare Au films, Au with ITO layers, and Au with Parylene C layers, and their sheet resistance was measured. Four contact pads were evaporated on top of the corners of the thin film stacks (Figure 3.1A) so that the sensing probe did not directly touch the surface of the tested films, avoiding any potential damage from the probe, and to ensure that the measurement was done across the top surface of the multilayered films. All films were labeled as $ITO_y/Au_x/ITO_y$ or $Au_x/(ITO \text{ or } P)_y$, where the subscript of *x* or *y* represents the thickness of the respective layer in nm, *P* represents Parylene, and the topmost layer is presented on the right. A typical procedure to fabricate an Au_5/ITO_5 film is illustrated in Figure 3.1A.

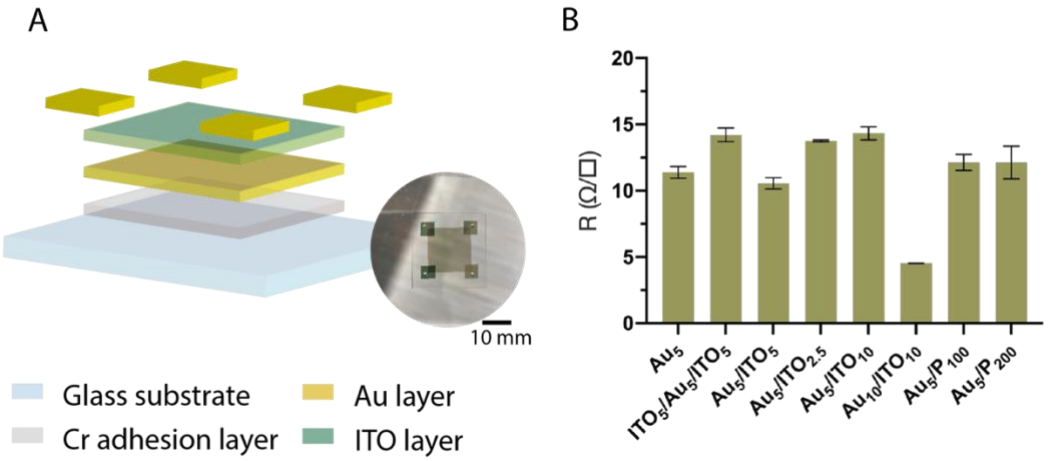

Figure 3.1. Four-point probe sheet resistance measurements on multilayer electrodes. (**A**) Schematic of sample fabrication for four-point probe measurement. The materials were deposited layer-by-layer on glass coverslips: 5 nm-thick Cr as adhesion layer; 5 nm-thick Au layer; 5 nm-thick ITO layer; four 50 nm-thick Au contact pads at the corners of the film. The inset is a photo of the fabricated sample, with the dots on the contact pads showing a droplet of EGaIn used to ensure good contact between the tip of the probe and the pad. (**B**) Sheet resistance measured from films fabricated on glass. Bars represent the average of sheet resistance measured from three independent samples (N = 3) and the error is the standard deviation.

All electrodes fabricated on glass substrates exhibited excellent conductivity, as shown by the measured sheet resistance (Figure 3.1B, resistivity graph can be found in Supplementary Information, Figure S3.2). Several interesting trends were observed from this data. First, there is an overall trend where the sheet resistance of a multilayer electrode is determined by the thickness of the Au layers, in agreement with previous reports [22,24,25]. All films containing a 5 nm-thick Au layer show sheet resistance that is comparable to that of the bare 5 nm Au film (~10 Ω/sq), whereas the films containing a 10 nm-thick Au layer displayed approximately half this value. This implies that the conductivity of a multilayer stack electrode can be tuned by changing the thickness of the Au layer. Furthermore, changing the ITO thickness from 2.5 to 10 nm or the Parylene thickness from 100 to 200 nm did not affect the sheet resistance to an appreciable degree, which implies that so long as the passivating layer allows the

transfer of electrons into the gold layer, the electrode remains conductive. To our knowledge, this is the first time that Parylene is used in a multilayer conductive electrode at thicknesses that allow it to be a conductive rather than an insulating coating. Finally, we observed that electrodes with an ITO/Au/ITO configuration showed similar sheet resistance to ones with Au/ITO configuration. These results show that ITO/Au/ITO and Au/(ITO or P) film configurations are conductive and potential candidates for the fabrication of corrosion resistant and stretchable electrodes.

3.3.2 Conductivity of wrinkled films on PS and PDMS

Next, we fabricated multilayered electrodes on pre-stressed PS substrates and compared their electrical properties as deposited (flat), after thermal shrinking (wrinkled on PS) and after transfer to a receiving elastomer (wrinkled on PDMS). The flat electrodes on flexible PS were conductive and displayed sheet resistances that compared favourably with those fabricated on rigid glass substrates (Figure 3.2A). Thermally shrinking the underlying PS substrate and wrinkling the multilayered electrodes caused a marginal increase in sheet resistance. This is in contrast with the behavior previously observed for bare Au, where the sheet resistance was seen to decrease after shrinking [26]. This can be explained by the fact that the wrinkling process does not create additional conductive paths for electrons, since the passivating film prevents different parts of the gold film from coming into contact as it gets folded. By comparing the sheet resistance of the films in Figure 3.2A, we observed that a change in thickness of the ITO layer did not impact the sheet resistance of the wrinkled multilayer electrodes, and that an increase in the thickness of the Au layer significantly decreased the sheet resistance. These trends are in line with those observed for electrodes fabricated on glass substrates, indicating that the fabrication on PS and subsequent wrinkling did not alter the electrical properties of the multilayered electrodes.

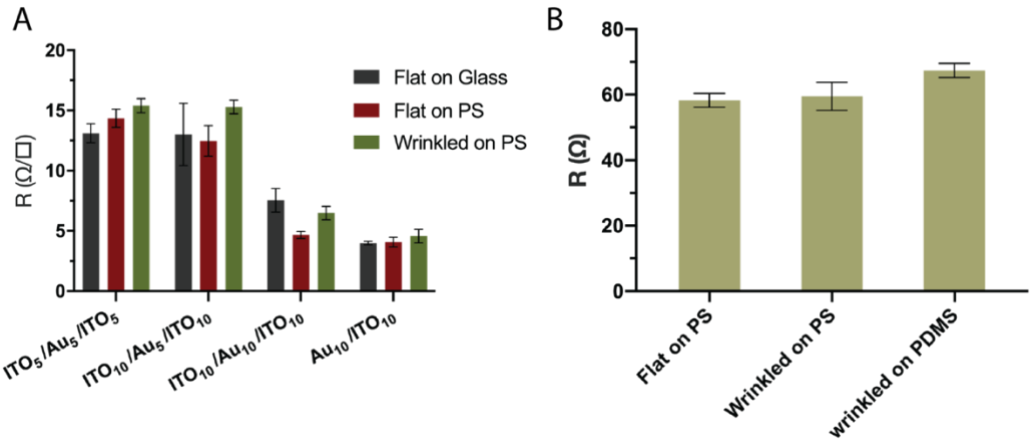

Figure 3.2. Comparison of the electrical properties of flat, wrinkled and transferred electrodes. (**A**) Sheet resistance of multilayered flat electrodes fabricated on glass and PS substrates, and of wrinkled (shrunken) films on PS substrates. (**B**) Resistance of a bone shaped multilayered ITO5/Au5/ITO5 electrode: flat on PS substrate, wrinkled (shrunken) on PS substrate, and wrinkled (shrunken) transferred onto PDMS substrate. Bars represent the average of sheet resistance or resistance measured from three independent samples (N = 3) and the error is the standard deviation.

We observed that electrodes with Au/ITO and ITO/Au/ITO configurations showed similar sheet resistances regardless of whether they were on a rigid glass substrate or wrinkled on a shrunken PS substrate. Previous work has justified the use of a bottom layer of ITO to increase the surface energy of the receiving substrate [24,25,27], facilitating the Au deposition into a uniform layer. These studies have also suggested that the Au layer itself serves as a crystalline template for the crystalline growth of the top ITO layer, which could greatly enhance its conductivity. In this work, we did not observe any improved conductivity in the multilayered film as a function of deposition order or the inclusion of an underlying layer of ITO. We first studied the effect of the inclusion of a bottom layer of ITO on the conductivity of a multilayered film by testing the sheet resistance of an Au/ITO film on polystyrene and comparing it to that of the ITO/Au/ITO configuration. These measurements (Figure 3.2A) did not show statistically significant differences. Next, we measured the resistance of the wrinkled $ITO_5/Au_5/ITO_5$ films transferred onto PDMS and compared it to the wrinkled films on PS to evaluate whether establishing a connection through the first or last deposited layer

within the stack had a significant impact on the conductivity. Figure 3.2B shows resistance of the three $ITO_5/Au_5/ITO_5$ samples, flat films on PS substrate, wrinkled films on PS substrate and wrinkled films transferred onto PDMS. These results show that the wrinkled films on PDMS had a marginally higher resistance, which can be attributed to the formation of a small number of cracks in the film during the transfer process, where the films are subjected to tensile strains due to the swelling of the PDMS substrate during the toluene rinsing step. We therefore conclude that the bottom layer of ITO does not significantly enhance the sheet resistance. In this sense, two-layer Au/ITO electrodes would be better suited for building stretchable electrodes on PDMS, since they are more pliable and less prone to crack formation but retain the conductive properties of their 3-layer counterparts.

3.3.3 Evaluation of corrosion-resistance of multilayered electrodes

Multilayered conductive films containing an oxide or polymer as the top layer are attractive for applications where the electrodes are exposed to corrosive environments. To assess the corrosion resistance of our multilayered electrodes, they were exposed to an electrolyte solution containing the redox couple I^-/I^{3-} while a voltage bias was applied, and the resulting current was monitored (setup shown in Supplementary Information, Figure S3.1). This I^-/I^{3-} system is known to be corrosive to most noble metal electrodes, including Au, which has prevented their use in dye-sensitized solar cells [28]. Thus, in this test current flowing through the electrode would decrease if the electrode was corroded by direct contact with the electrolyte. Figure 3 shows the results obtained from Au films coated with ITO of different thicknesses, where the normalized current (I/I_0) is plotted over time. In all samples containing a bare 5-nm-thick Au electrode (Figure 3 yellow lines), the current rapidly dropped to zero as soon as the electrolyte was applied at the 15 s mark. For Au/ITO films fabricated on glass substrates (Figure 3.3A), a 2.5 nm ITO layer delayed electrode failure until ~60 s where the current dropped by half. In contrast, 5 and 10 nm ITO layers provided complete protection against corrosion over the recorded time (up to 1000 s). These results suggest that the

lower thickness of ITO could not form a complete protective layer, so that the electrolyte could seep through and corrode the Au, and that a minimum of 5 nm of ITO was needed to passivate the Au layer. Flat electrodes prepared on flexible PS substrates (Figure 3.3B) showed a similar trend, with 2.5 nm partially protecting the Au layer against corrosion, albeit with slower kinetics than those observed on glass, and the thicker ITO layers fully protecting it. The Au_5/ITO_{10} was seen to start to deteriorate at longer recorded times, possibly because thick ITO films are brittle and can form small cracks when the flexible substrate is handled during experimentation. In contrast to the flat samples, all wrinkled Au/ITO electrodes on PS were corroded (Figure 3.3C), although there was an improvement in corrosion resistance with thicker films. This is explained by the presence of some cracks in the wrinkled electrodes (highlighted by the green square in Figure 3.3D), which allows the electrolyte to seep in and corrode the Au layer, leading to the eventual failure of the entire film. Based on these observations, Au/ITO electrodes are suitable against corrosive environments if prepared flat, but are not good candidates for wrinkled, stretchable electrodes.

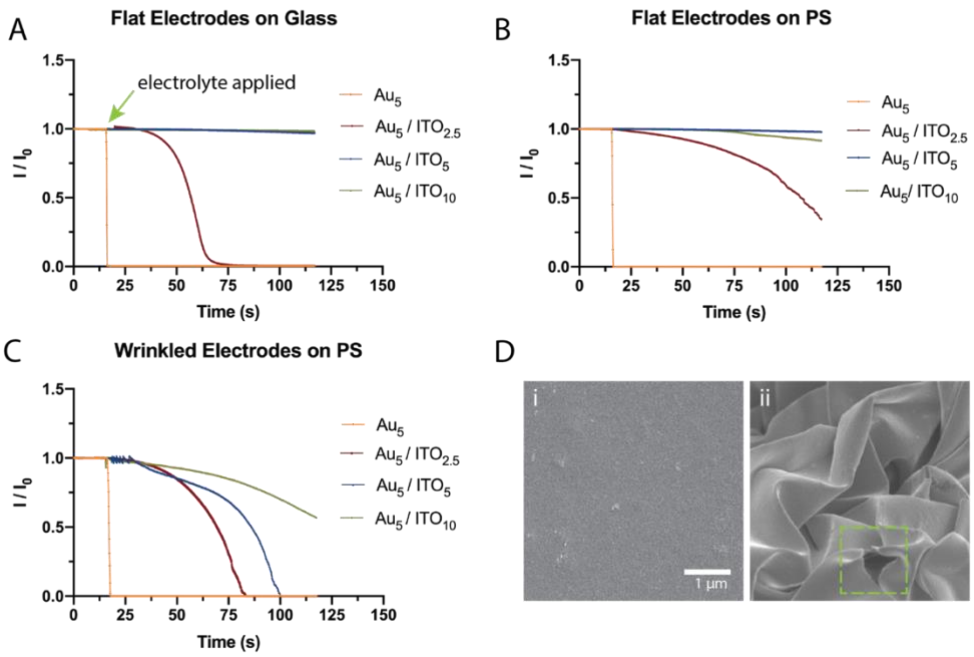

Figure 3.3. Corrosion-resistance of Au/ITO films. Normalized current (I/I0) vs. time plots for (**A**) flat Au5/ITOx on glass substrate, (**B**) flat Au/ITOx on PS substrate, and (**C**) wrinkled Au/ITOx on PS substrate. In all cases x = (0, 2.5, 5.0, and 10.0 nm) and the corrosive electrolyte

was applied at the 15 s mark. (**D**) Topography of Au5 /ITO5 visualized under SEM: **i**) flat film on PS; **ii**) wrinkled film on PS. A visible crack on the wrinkled film is labeled with a dashed square.

While flat Au/ITO electrodes showed some promise against corrosion, the low fracture toughness of these films poses an issue during the wrinkling process, suggesting that more flexible films should be considered for this approach. Parylene was chosen as an alternative to overcome the cracking of the multilayered electrodes, due to its lower elastic modulus (4.2-5.1 GPa) [18] compared to ITO (~89 ± 1 GPa) [29]. Thick Parylene films (typically > 1 μm) have been used as passivation layers due to their dielectric properties [14,30,31], but to our knowledge thin layers have not been explored in multilayered conductive electrodes. We observed that Parylene films up to 200 nm thickness allowed current to conduct across this passivating layer and into the gold layer (Figure 3.1B), making the multilayered Au/P electrodes good conductive elements. Preliminary corrosion tests were performed on Au_5/P_y (y = 20, 50, 100 nm) stacks on rigid glass substrates (Figure 3.4A). Due to incomplete coverage, Parylene layers with thickness of 20 and 50 nm failed to protect the gold film from corrosion, as can be seen by the dramatic drop in current after exposure to the electrolyte. Au_5/P_{100} electrodes, on the other hand, showed excellent corrosion resistance while still being conductive, making them good candidates for wrinkled stretchable electrodes.

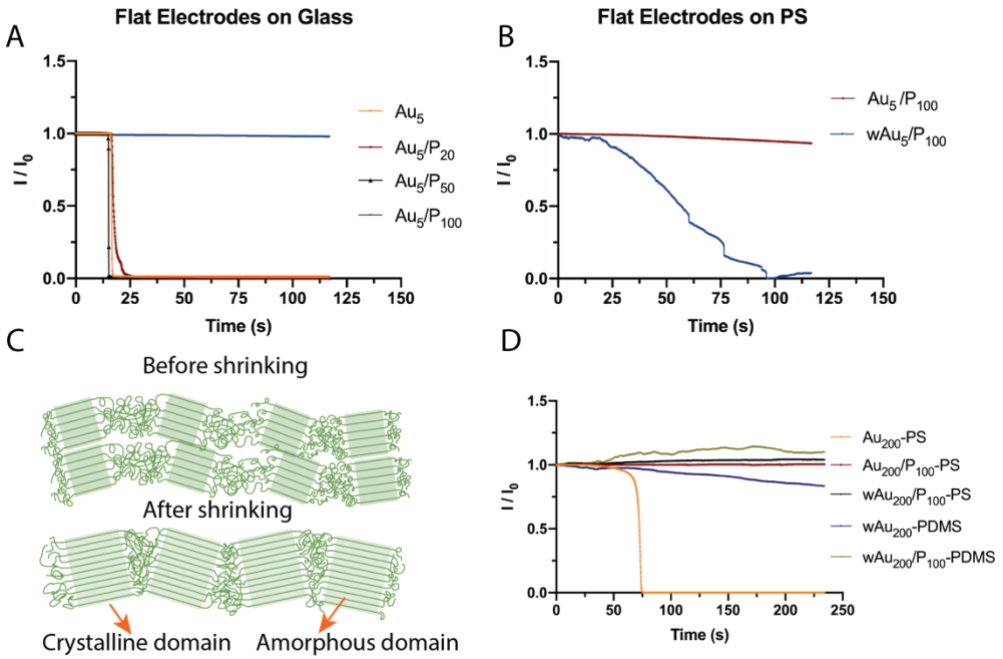

Figure 3.4. The corrosion resistance of multilayered films was evaluated. (A) Au_5/P_x on glass substrates, with x = (20, 50, 100 nm). **(B)** The performance of films on PS substrates was compared for: Au_5/P_{100} flat films, wrinkled Au_5 followed by coating with P_{100} (wAu_5/P_{100}). **(C)** Schematic showing the difference in size of the crystalline domains within Parylene before and after thermal shrinking. **(D)** The performance of films composed of 200 nm Au and 100 nm Parylene layers were compared after different fabrication approaches: Au_{200} on PS substrate (Au_{200}-PS), Au_{200}/P_{100} on PS substrate (Au_{200}/P_{100}-PS), wrinkled Au_{200} followed by coating with P_{100} on PS substrate (wAu_{200}/P_{100}-PS), wrinkled Au_{200} transferred onto PDMS substrate (wAu_{200}-PDMS), wrinkled Au_{200} transferred onto PDMS substrate and coated with P_{100} (wAu_{200}/P_{100}-PDMS).

We next investigated the effect of shrinking on the corrosion resistance for Au_5/P_{100} electrodes fabricated on PS substrates. The flat electrodes on PS (Au_5/P_{100}, Figure 3.4B) behaved the same as those on glass substrates (Figure 3.4A), providing excellent corrosion resistance. However, films that were wrinkled as a stack after fabrication on PS ($Au_5/P_{100}w$) were found to be completely insulating and unable to conduct significant current under the applied bias (no data could be recorded from these devices). This is likely caused by the PS shrinking process, where the electrodes are

subjected to temperatures of 130˚-160 ˚C for 10-20 mins (including shrinking and flattening) [18]. Given that these temperatures are above the glass transition temperature of Parylene (40-80˚C) [32], the shrinking process acts as an annealing treatment that induces the growth of crystalline domains (Figure 3.4C), as previously reported [32–34]. A higher density of crystalline domains results in lower water permeability and higher dielectric properties, making a thermally annealed Parylene film more insulating than an untreated one [32]. To overcome the loss of conductivity of the Parylene layer due to the shrinking process, the 5 nm-thick Au films, were first wrinkled and then coated with a 100 nm-thick Parylene layer (wAu_5/P_{100}). Electrodes fabricated under these conditions failed the corrosion test (Figure 3.4C), which is attributed to the inability of this thickness film to fully cover the nanowrinkled surfaces and folds produced by such thin gold films.

So far, the lessons learned are that the thermal shrinking process will make the Parylene more insulating and that it is hard to fully passivate highly complex nano-wrinkles. To overcome these limitations, our strategy was to make wrinkles larger and deposit Parylene on the wrinkled Au film that already been wrinkled. Thicker films, films with a higher modulus, or the presence of a sacrificial layer under the rigid film can make the wavelength of the wrinkles larger [18,35,36]. Therefore, the fabrication process was modified to deposit 100 nm-thick Parylene layers directly onto 200 nm-thick wrinkled Au films fabricated on PS (wAu_{200}/P_{100} -PS) substrates or which had been transferred onto PDMS substrates through a sacrificial layer-assisted process (wAu_{200}/P_{100} -PDMS). As anticipated, flat Au_{200} on PS become instantly corroded when exposed to the electrolyte, while flat Au_{200}/P_{100} are corrosion resistant (Figure 4D). However, in this case the electrodes fabricated on PS where the 200 nm-thick gold film was first wrinkled and then coated (wAu_{200}/P_{100}) showed excellent corrosion resistance. To our surprise, bare Au wrinkled films transferred to PDMS (wAu_{200}-PDMS) showed slow degradation kinetics. This could be a result of the wetting properties of the wrinkled Au films, where small air pockets are entrapped between the wrinkles under the applied electrolyte and lead to wetting in the Cassie-Baxter regime. The wrinkled films transferred onto the PDMS substrate and coated with Parylene (wAu_{200}/P_{100}-

PDMS) were conductive and highly corrosion resistant, making them ideal candidates for stretchable electrodes.

3.3.4 Evaluation of stretchability of multilayered electrodes

Stretchability tests were performed on wAu_5-PDMS, $w(Au_5/ITO_5)$ and wAu_{200}/P_{100}-PDMS by measuring the change in sheet resistance as a function of applied tensile strain. All films were robust, with minor sheet resistance increases up to 75 % strain, after which the resistance increased or the PDMS cohesively failed (Panel A in Figure 3.5). It is worth noting that the sheet resistance of wAu_{200}/P_{100}-PDMS electrodes is in the 0.10 - 0.15 Ω/sq range when subjected to < 50 % strain, which is comparable to that of bulk Au. These results along with the excellent corrosion resistant properties of the wAu_{200}/P_{100}-PDMS electrodes make them attractive as conductive elements for flexible or stretchable devices that are exposed to corrosive environments. A further characterization of the corrosion resistance of the wAu_{200}/P_{100}-PDMS electrodes under different strain was displayed on panel B in Figure 3.5. The electrode was corrosion resistant at 2.5% stain but started to degrade at 5% strain, with major degradation observed under 10% strain, which was much less robust than expected. We predicted a better stretchability and corrosion resistance performance due to the excellent stretchability and corrosion-resistance shown in Figure 3.4 and panel A in Figure 3.5. One possible reason that caused such small strain tolerance is the way the experiment was conducted, where the electrolyte was confined in a corral that was made with nail polish before stretching. Since the nail polish is not stretchable and strongly attached to the electrode, it might cause tearing at the interface between the film and the nail polish. Nevertheless, the unique wrinkled topography of the resulting film also offers a strong adhesion between parylene and the active gold layer [26], providing a solution to the ongoing obstacle of delamination when Parylene is used [31,37].

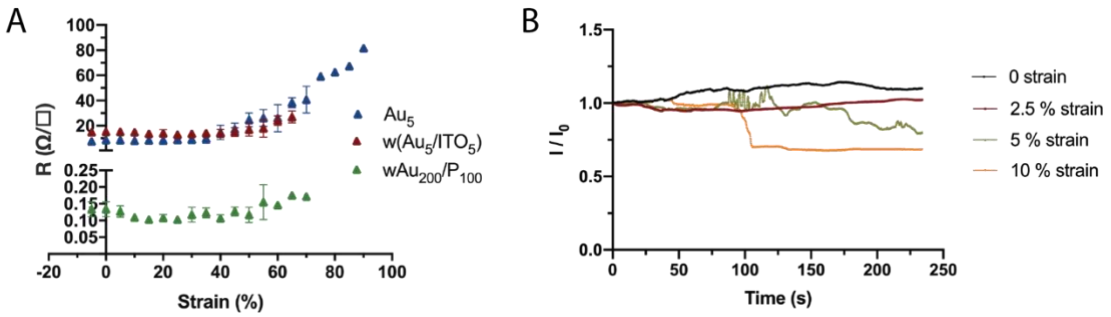

Figure 3.5. (A) Sheet resistance vs. strain carried out for samples transferred onto PDMS substrate. 5 nm-thick Au (Au_5), wrinkled 5 nm-thick and 5 nm-thick ITO transferred onto PDMS ($w(Au_5/ITO_5)$), wrinkled 200 nm-Au transferred onto PDMS and coated with100 nm-thick Parylene (wAu_{200}/P_{100}). **(B)** Corrosion resistance for the electrode of wrinkled 200 nm-Au transferred onto PDMS and coated with100 nm-thick Parylene (wAu_{200}/P_{100}) under different strain: 0, 2.5%, 5% and 10%.

3.4. Conclusion

A new strategy for fabricating stretchable and corrosion resistant electrodes has been presented. Based on a multilayer concept of building conductive electrode, a thin Parylene layer was employed as passivation that allowed the electrode to remain conductive. The material and thickness combinations for the different layers were selected through sheet resistance measurements and corrosion resistance tests. A series of optimizations, which involved the processes of shrinking and transfer, thermal treatment, and coating, were performed to arrive at the optimal multilayered electrode configuration. Electrodes made of 200 nm-thick wrinkled Au on PDMS coated with 100 nm-thick Parylene display high stretchability and excellent corrosion resistance. We anticipate these electrodes will aid in the development of wearable and implantable medical electronic devices.

Funding: X.D. was partially supported through a China Scholarship Council doctoral award. J.M.M.-M. is the Tier 2 Canada Research Chair in Micro and Nanostructured Materials and the recipient of an Early Researcher Award from the Ontario Ministry of Research and Innovation. This work was supported by funding

through a Discovery Grant from NSERC and a Canadian Foundation for Innovation J.E.L.F. instrumentation grant to J. M.-M. (RGPIN-2019-06433). This research made use of instrumentation within McMaster's Canadian Centre for Electron Microscopy.

Acknowledgments: The authors thank Jaana Vapaavuori for kindly providing the electrolyte.

References

1. Rogers, J. A.; Someya, T.; Huang, Y. Materials and mechanics for stretchable electronics. *Science* **2010**, *327*, 1603-1607.
2. Kim, D. H.; Lu N.; Ghaffari R.; Kim Y.S.; Lee S.P.; Xu L. et al. Materials for multifunctional balloon catheters with capabilities in cardiac electrophysiological mapping and ablation therapy. *Nat. Mater.* **2010**, *10*, 316-323.
3. Boutry, C. M.; Beker L.; Kaizawa Y.; Vassos C.; Tran H.; Hinckley A.C. et al. Biodegradable and flexible arterial-pulse sensor for the wireless monitoring of blood flow. *Nat. Biomed. Eng.* **2019**, *3*, 47-57.
4. Weiland J. D.; Humayun, M. S. Intraocular retinal prosthesis. *Trans. Am. Ophthalmol. Soc.* **2006**, *25*, 60-66.
5. Stieglitz, T. Development of a micromachined epiretinal vision prosthesis. *J. Neural Eng.* **2009**, *6*, 065005.
6. Khodagholy, D.; Gelinas J. N.; Thomas T.; Doyle W.; Devinsky O.; Malliaras G. G. et al. NeuroGrid: recording action potentials from the surface of the brain. *Nat. Neurosci.* **2015**, *18*, 310-316.
7. Liu, J.; Kim Y. S.; Richardson C. E.; Tom A.; Ramakrishnan C.; Birey F. et al. Genetically targeted chemical assembly of functional materials in living cells, tissues, and animals. *Science* **2020**. *367*, 1372-1376.
8. Kim, D. H.; Viventi J. Dissolvable films of silk fibroin for ultrathin conformal bio-integrated electronics. *Nat. Mater.* **2010**, *9*, 511-517.
9. Manivasagam, G., Dhinasekaran, D.; Rajamanickam, A. Biomedical implants: corrosion and its prevention-a review. *Recent Patents Corros. Sci.* **2010**, *2*, 40-54.
10. Sekitani, T.; Zschieschang, U.; Klauk, H.; Someya, T. Flexible organic transistors and circuits with extreme bending stability. *Nat. Mater.* **2010**, *9*, 1015-1022.
11. Sekitani, T.; Someya, T. Air-stable operation of organic field-effect transistors on plastic films using organic/metallic hybrid passivation layers. *Japanese J. Appl. Physics* **2007**, *46*, 4300-4306.
12. Kaltenbrunner, M.; Sekitani T.; Reeder J.; Yokota T.; Kuribara K.; Tokuhara T. et al. An ultra-lightweight design for imperceptible plastic electronics. *Nature* **2013**, *499*, 458-463.
13. Bettinger, C. J.; Ecker M.; Kozai T. D. Y.; Malliaras G. G.; Meng E.; Voit W. et al. Recent advances in neural interfaces-Materials chemistry to clinical translation. *MRS Bull.* 2020, *45*, 655-668.
14. Maynard, E. M., Nordhausen, C. T.; Normann, R. A. The Utah intracortical electrode array: a recording structure for potential brain-computer interfaces. *Electroencephalogr. Clin. Neurophysiol.* **1997**, *102*, 228-239.
15. Hsu, J. M.; Rieth, L.; Normann, R. A.; Tathireddy, P.; Solzbacher, F. Encapsulation of an integrated neural interface device with parylene C. *IEEE Trans. Biomed. Eng.* **2009**, *56*, 23-29.
16. Zhu, Y.; Moran-Mirabal, J. M. Highly bendable and stretchable electrodes based on micro/nanostructured gold films for flexible sensors and electronics. *Adv. Electron. Mater.* **2016**, *2*, 1-6.
17. Kim, J.; Park S. J.; Nguyen T.; Chu M.; Pegan J. D.; Khine M. Highly stretchable wrinkled gold thin film wires. *Appl. Phys. Lett.* **2016**, *108*, 061901.

18. Ding, X.; Moran-Mirabal, J. M. Efficient multi-material structured thin film transfer to elastomers for stretchable electronic devices. *Micromachines* **2022**, *13*, 1-12.
19. Hartig, K.; Münz, W. D.; Scherer, M.; Wittwer, V.; Stahl Industrial Realization of low-emittance oxide/metal/oxide films on glass. *Opt. Mater. Process Technol. Energy Effic. Sol. Appl.* **1983**, *0428*, 9-13.
20. Bright, C. I. Review of transparent conductive oxides (TCO). *Society of vacuum coaters* **2007**, 38-45.
21. Bright, C. I. Transparent conductive thin films. *In Optical Thin Films and Coatings: From Materials to Applications,* 2nd eds.; Elsevier Ltd.: Amsterdam, Netherland, 2018; pp. 741-788.
22. Bender, M.; Seelig W.; Daube C.; Frankenberger H.; Ocker B.; Stollenwerk J. Dependence of film composition and thicknesses on optical and electrical properties of ITO-metal-ITO multilayers. *Thin Solid Films* **1998**, *326*, 67-71.
23. Ellmer, K. Past achievements and future challenges in the development of optically transparent electrodes. *Nat. Photonics* **2012**, 6, 809-817.
24. Guillén, C.; Herrero, J. ITO/metal/ITO multilayer structures based on Ag and Cu metal films for high-performance transparent electrodes. *Sol. Energy Mater. Sol. Cells* **2008**, 92, 938-941.
25. Fang, X.; Mak C. L.; Dai J.; Li K.; Ye H.; Leung C. W. ITO/Au/ITO sandwich structure for near-infrared plasmonics. *ACS Appl. Mater. Interfaces* **2014**, *6*, 15743-15752.
26. Ding, X.; Shen, E.; Zhu, Y.; Moran-Mirabal, J. M. Stretchable thin film inductors for wireless sensing electronic devices
27. Kim, Y. S.; Park J. H.; Choi D. H.; Jang H. S.; Lee J. H.; Park H. J. et al. ITO/Au/ITO multilayer thin films for transparent conducting electrode applications. *Appl. Surf. Sci.* **2007**, *254*, 1524-1527.
28. Miettunen, K.; Vapaavuori, J.; Poskela, A.; Tiihonen, A.; Lund, P. D. Recent progress in flexible dye solar cells. *Wiley Interdiscip. Rev. Energy Environ.* **2018**, *7*, 302.
29. Oh, S. J.; Kwon, J. H.; Lee, S.; Choi, K. C.; Kim, T. S. Unveiling the annealing-dependent mechanical properties of freestanding indium tin oxide thin films. *ACS Appl. Mater. Interfaces* **2021**,*13*, 16650-16659.
30. Kim, B. J.; Meng, E. Micromachining of Parylene C for bioMEMS. *Polym. Adv. Technol.* **2016**, *27*, 564-576.
31. Von Metzen, R. P.; Stieglitz, T. The effects of annealing on mechanical, chemical, and physical properties and structural stability of Parylene C. *Biomed. Microdevices* **2013**,*15*, 727-735.
32. Golda-Cepa, M.; Engvall, K.; Hakkarainen, M.; Kotarba, A. Recent progress on parylene C polymer for biomedical applications: A review. *Prog. Org. Coatings* **2020**,*140*, 105493.
33. Fukuda, K.; Suzuki, T.; Kumaki, D.; Tokito, S. Reverse DC bias stress shifts in organic thin-film transistors with gate dielectrics using parylene-C. *Phys. Status Solidi Appl. Mater. Sci.* **2012**, *209*, 2073-2077.
34. Chemistry, P. Crystal structure of poly(2-chloro-p-xylylene). *Bull. Inst. Chem. Res., Kyoto Univ.* **1983**, *61*, 222-228.

35. Stimpson, T. C.; Osorio, D. A., Cranston, E. D.; Moran-Mirabal, J. M. Direct comparison of three buckling-based methods to measure the elastic modulus of nanobiocomposite thin films. *ACS Appl. Mater. Interfaces* **2021**,*13*, 29187-29198.
36. Gill, U.; Sutherland T.; Himbert S.; Zhu Y.; Rheinstädter M. C.; Cranston E. D.; Moran-Mirabal J. M. Beyond buckling: humidity-independent measurement of the mechanical properties of green nanobiocomposite films. *Nanoscale* **2017** *9*, 7781-7790.
37. Li, W.; Rodger D. C.; Meng E.; Weiland J. D.; Humayun M. S.; Tai Y. C. Wafer-level parylene packaging with integrated RF electronics for wireless retinal prostheses. *J. Microelectromechanical Syst.* **2010**, *19*, 735-742.

Appendix B: Chapter 3 Supplementary Information

Fabrication of Corrosion Resistant Stretchable Multilayer Electrodes

Xiuping Ding, Jose M. Moran-Mirabal

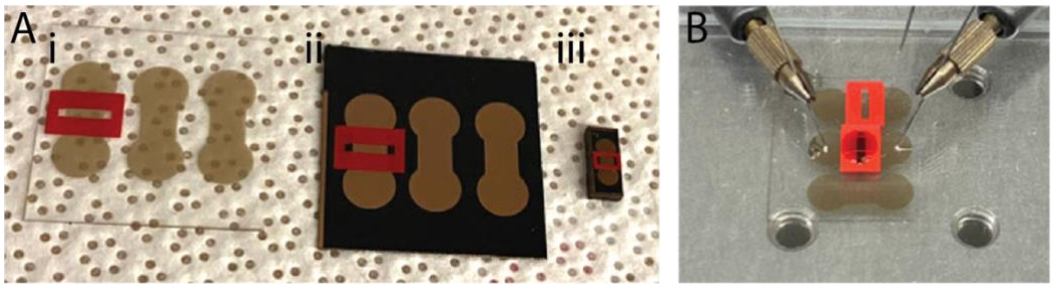

Figure S3.1. Corrosion resistance measurement. (**A**) Bone-shaped Au5/ITO5 samples with gaskets (red vinyl): **i)** Flat on glass; **ii)** Flat on PS; **iii)** Wrinkled on PS. (**B**) Two-point measurement: electrolyte was placed at the 15 s and probes contact the films with EGaIn.

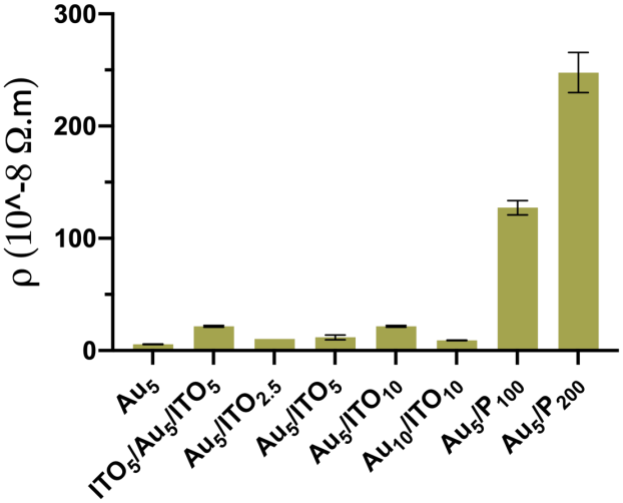

Figure S3.2. Resistivity corresponding to the films in Figure 1B, films fabricated on glass. Bars represent the average of resistivity measured from three independent samples (N = 3) and the error is the standard deviation.

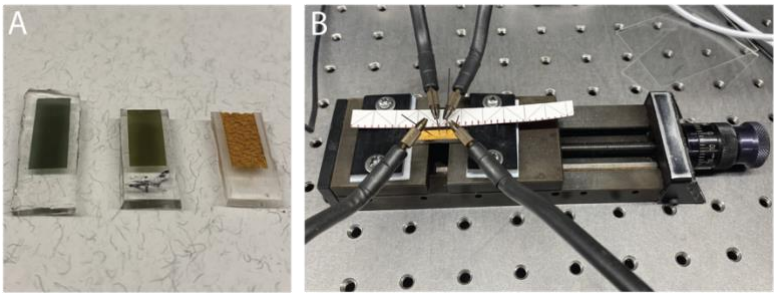

Figure S3.3 Corrosion resistance test samples and setup. (**A**) Wrinkled electrodes after the stretchability measurement. From left to right: Au_5-PDMS, w(Au_5/ITO_5)-PDMS, wAu_{200}/P_{100}-PDMS. (**B**) Sheet resistances were measured with four-point technique with a co-linear probes arrangement. The space between neighbouring two probes are 3 mm.

Chapter 4

Stretchable thin film inductors for wireless sensing in wearable electronic devices

Xiuping Ding, Ethan Shen, Yujie Zhu and Jose M. Moran-Mirabal

Abstract: The unique soft and elastic nature of stretchable electronics has potential to advance wearable devices. The integration of wireless power and data communication technology into stretchable electronics, which could be realised by inductive coupling and oscillator circuits, is key to achieve continuous monitoring of body signals with minimally invasive devices. As one of the main components for inductive coupling and oscillator circuits, the development of stretchable inductors is therefore compelling. The most common strategy to fabricate stretchable inductors is to add periodic waves to a spiral conductor, which provides mechanical robustness but inevitably increases resistance. In this work, we introduce a method to fabricate stretchable inductors, which relies on creating a wrinkled thin film inductor on a polystyrene substrate, functionalizing the inductor surface with an adhesive layer, and then transferring the structure onto a polydimethylsiloxane (PDMS) elastomer. Contrary to inductors created through the addition of periodic wave patterns, the wrinkled inductor features low resistance while providing high stretchability. The wrinkled inductors fabricated using this approach exhibited 30% decrease in resistance compared to their flat counterparts of the same size and geometry. Impedance and inductance under uniaxial stretching remained unchanged up to 45% strain, revealing exceptional electrical and mechanical stability. The strong chemical bonding between the functionalized wrinkled inductor and the PDMS elastomer contributes to the robustness and long-term stability of the device. This method provides an added advantage of miniaturization of the stretchable inductor, as it is shrunk to 16% of its original size during the wrinkling process. This technology has potential for building high performance stretchable inductors for

stretchable wireless electronic devices and can eventually benefit the design of electronics for implants, health care monitoring and wearable communication.

Keywords: thin film transfer, wrinkled film, miniaturized devices, Parylene

4.1. Introduction

The integration of existing electronic platforms into wearable electronics is hindered by their typically rigid and planar nature, as well the necessity to connect through wires to external power and monitoring devices. The stiffness of the devices, mechanical stresses imposed by them, and the wired terminal connections and power supplies all lead to invasive medical diagnostic devices, that pose risks of injury to a patient [1]. Wired connections can also complicate the most basic bedside tasks and interrupt the user's routine activities [2]. When combined with wireless technology, wearable devices can enable non-invasive and comfortable physiological measurements, thus unlocking the potential of stretchable electronics for advanced healthcare applications and further blurring the boundary between electronics and the human body.

The use of wireless technology for electronic devices encompasses primarily wireless power supply [3, 4] and wireless data communication [5, 6]. Wireless power supply can be achieved through inductive coupling, using an electromagnetic field to transfer power from a transmitting antenna, which is connected to an external power source, to the receiving antenna located on the wireless device. The delivered power can then be used, for example, to charge a sensor battery or to directly operate a battery-free sensor. Battery-free sensors convey the advantages that the size of the system can be minimized and they can avoid safety issues, such as battery heating or electrolyte leakage [7]. Wireless data transfer technologies such as radiofrequency identification [8], near-field communication [9], and resonant circuits are the focus of much research aimed at developing wearable wireless devices. Given that inductors are the main

component for both wireless power and data transfer technologies, the fabrication of stretchable inductors is key to the development of wearable electronics [10].

To date, the main strategy for fabricating stretchable inductors has been to add periodic waves to planar thin film structures, which affords stretchability but greatly increases the inductor resistance [10]. Higher resistance inevitably reduces the device quality factor and worsens device performance due to energy dissipation through ohmic losses [11]. Therefore, alternative strategies to fabricate stretchable inductors are needed. In this work, we present a new method for fabricating stretchable inductors with excellent stretchability and low resistance. The fabrication strategy relies patterning a multi-material thin film spiral inductor on a polystyrene (PS) substrate, and wrinkling it through thermal shrinking of the substrate [12, 13]. The wrinkled inductor is then transferred onto a receiving elastomer substrate, such as PDMS. The inductors on the elastomer exhibited the same properties as the flat and wrinkled devices before transfer and showed excellent robustness against delamination as assessed through tape peel tests. The wrinkles on the thin film inductor allowed it to be stretched by up to 45% strains, while maintaining excellent conductivity and a constant inductance and impedance values. The stretchable inductor fabrication approach presented could help accelerate the development of wireless wearable electronics for healthcare applications that show high robustness and long-term stability.

4.2. Materials and Methods

4.2.1 Wrinkled inductor fabrication

A PS sheet (Graphix shrink film, Graphix, Maple Heights, OH, USA) was cut into 70 mm × 70 mm squares using a blade cutter (Robo Pro CE5000- 40-CRP, Graphtec America Inc., Irvine, CA, USA). The PS square substrates were cleaned by immersing them sequentially in isopropanol, ethanol, and 18.2 MW cm water (obtained from a Milli-Q Reference A+ Water Purification System, Millipore, Etobicoke, ON, Canada, subsequently referred to simply as “water”) baths and washing them on an orbital shaker (MAXQ 2000, Thermo Fisher Scientific, Waltham, MA, USA) for 5 min for each solvent. The clean PS substrates are hydrophobic and could be easily dried using

nitrogen gas. Self-adhesive vinyl films (FDC-4300, FDC graphic films, South Bend, IN, USA) were patterned using the blade cutter to make stencils, which were then adhered onto the PS substrates using transfer tape.

Au and SiO_2 thin films were deposited onto the masked substrates by sputtering using a Torr Compact Research Coater CRC-600 manual planar magnetron sputtering system (New Windsor, NY, USA). A 99.999% purity gold target (LTS Chemical Inc., Chestnut Ridge, NY, USA) and SiO_2 target (Bayville Chemical Supply Company Inc., Deer Park, NY, USA) were used to deposit thin films of the materials. Au films and SiO_2 films were sputtered using a DC (direct current) gun and RF (radio frequency) gun, respectively.

Dichloro-(2,2)-paracyclophane (subsequently referred to simply as Parylene) was deposited as an insulating layer on devices masked with a self-adhesive vinyl stencil (containing a 3.6 mm × 16.0 mm window) using a Chemical Vapor Deposition system (PDS 2010, Specialty Coating System. Inc, Indianapolis, IN, USA). One gram of Parylene dimer (Specialty Coating Systems, Indianapolis, IN, USA) was loaded into the CVD system to obtain a 1.5 μm-thick Parylene layer, as measured with a surface profilometer (Tencor Alpha Step 200, KLA Corp., Milpitas, CA, USA). The inductor on PS was then thermally shrunk in an oven at 130 ˚C for 5 minutes and then placed on a silicon wafer heated at 160 ˚C until it was uniformly flat (~15 minutes).

4.2.2 Transfer of wrinkled thin film inductors to PDMS

To facilitate the transfer of the wrinkled thin film inductors to PDMS, an adhesive self-assembled layer was formed on the Au layers through immersion for 1 h in an aqueous solution containing 5 mM (3-mercaptopropyl)trimethoxysilane (MPTMS) (95%, Sigma-Aldrich, MO, USA). After the incubation, the sample was rinsed with water to remove any unbound MPTMS and dried using a nitrogen stream. To ensure that the first and second Au layers connected at the center of the inductor, a small drop of eutectic Gallium-Indium (EGaIn, >= 99.99 % trace metals basis, Sigma-Aldrich, St. Louis, MO, USA) was placed at the interface between Au/Parylene/Au and Au layers. Next, PDMS base and curing agent (Sylgard 184 silicone elastomer kit, Dow Corning

Corporation, Corning, NY, USA) were mixed in 10:1 w/w ratio and the mixture was degassed under vacuum. The pre-cured PDMS mix was cast onto the sample and cured in an oven for 4 h at 70 ˚C. To make the interface between the PS and PDMS more accessible to solvent and facilitate the device lift off, the PDMS was cut along the edge of the PS square substrate. The sample was then immersed in acetone (reagent grade, Caledon Laboratories, Ltd., Georgetown, ON, Canada), where the PS substrate gradually swelled and softened over time. After 24 hours, the soft and sticky PS could be removed manually with tweezers. The PDMS with the transferred wrinkled thin film was then rinsed with toluene (ACS reagent, Sigma-Aldrich, St. Louis, MO, USA) to remove any remaining PS residue. The device was finally placed in a vacuum oven at 60 ˚C overnight to extract the toluene from the PDMS elastomer. Fabricated devices were stored in plastic dishes until further used.

4.2.3 Characterization of thin film stretchable inductors

Morphology. The morphology of flat and wrinkled thin film inductors was characterized through scanning electron microscope imaging (JSM-7000F, JEOL Ltd.,Tokyo, Japan) using a 5.0 kV (flat inductor) and 10.0 kV (wrinkled inductor) acceleration voltage.

Resistance. A commercial multimeter (Mastercraft 52-0055-6, Canadian tire corporation, Ltd., Toronto, ON, CA) was used to measure the resistance of flat and wrinkled inductors on PS and wrinkled inductors on PDMS. The resistance was measured as shown in Figure S1 (Supplementary Information) from one contact pad (marked 0) to eight different points along the spiral (marked 1 through 8) and labeled as R_1-R_8 correspondingly.

Inductance & Impedance. The inductance and impedance of inductors were measured using a vector network analyzer (VNA, Rhode & Schwarz, ZNL6, Columbia, MO, USA) with a SMA connector (SMA(F)RA Jack, Taoglas, Minneapolis, MN, USA) for VNA cable (MRC-265MA-MF-1200, 895-GJe033004, MPI Corporation, San Jose, CA, USA). The VNA was calibrated with a standard calibration kit (open, close, match).

A commercial off-the-shelf 9230 Series Molded Axial Inductor (9230-08-RC, Bourns Inc., Riverside, CA, USA) with an inductance of 330 nH ± 10 % was used as reference. The stretching of the inductor was performed on a homemade stretcher, which could provide strains with a resolution of 0.01 mm.

4.3. Results and Discussion

4.3.1 Device fabrication

Electronic devices typically consist of complex structures and hybrid materials rather than a single layer of one material. This is also true for individual circuit components, like thin film inductors, which can be made from a combination of materials including conductors and insulators, and constructed layer-by-layer. This poses a challenge for the fabrication of stretchable electronics, as all components need to withstand the applied strain and the material layers of the device should remain cohesively bound. The mechanical robustness, when subjected to strain, of multi-material wrinkled thin films transferred from shrunken PS substrate to elastomers has inspired the exploration of new applications for stretchable electronics [14]. Generally, this method includes fabricating a thin film device on a pre-stressed PS substrate, thermal shrinking of the substrate to create wrinkled devices, and transfer of the whole device to PDMS.

Using this approach, we fabricated stretchable spiral inductors (Figure 4.1). The process started with a clean pre-stressed PS sheet, which can be thermally shrunken to 16% of its original footprint (Figure 4.1A). An adhesive vinyl stencil was patterned with a spiral inductor shape (Figure 4.1B) using a benchtop blade cutter able to produce patterned features with a resolution of ~200 µm. The substrate was masked with the adhesive stencil and a 50 nm-thick Au film was deposited. The vinyl stencil was then peeled off to reveal a spiral coil (Figure 4.1C, D). Given the strong adhesion between the Au film and the PS substrate, a second vinyl stencil could be placed directly on the Au film to accurately control the deposition of a 1.5 µm-thick Parylene layer (Figure 4.1E-F). Lifting off the vinyl stencil revealed a rectangular Parylene insulating film

(Figure 4.1G). Parylene was used as an insulation layer due to its ability to form conformal and pinhole free films, and its excellent dielectric strength (220 V/µm) [15]. This layer prevented short circuiting between the spiral inductor Au layer and a second Au layer, added to provide connectivity to the inner end of the inductor. A multilayer stencil was used to define the position and dimensions of the second Au layer while preserving the Parylene layer integrity (Figure 4.1H-I). After a 50 nm-thick Au film was deposited (Figure 4.1J), the multilayer stencil was removed, revealing an Au/Parylene/Au spiral inductor (Figure 4.1K). As a final device fabrication step, a 1 nm-thick SiO2 layer was deposited (Figure 4.1K) to facilitate the chemical bonding between the device and the receiving PDMS elastomer during the transfer step.

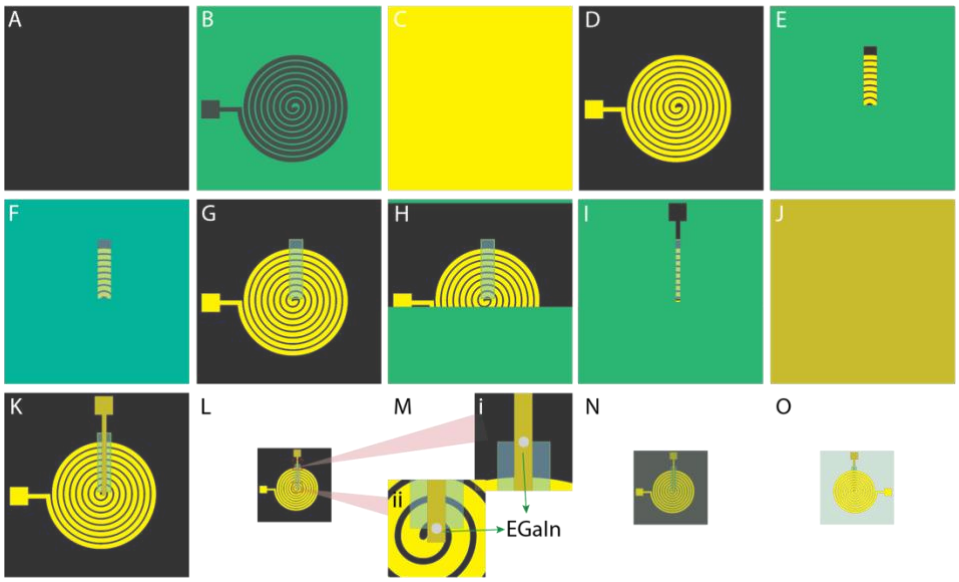

Figure 4.1. Schematic of the stretchable inductor fabrication process. **(A)** Clean pre-stressed PS substrate (black). (**B**) Masking the substrate with an adhesive vinyl stencil (green). **(C**) Sputtering of a 50 nm-thick Au film (yellow). (**D**) Peeling off the stencil. (**E**) Masking of the substrate for insulator layer of Parylene. (**F**) Parylene coating (translucent blue). (**G**) Revealing of the patterned Parylene insulation layer. (**H, I**) Multilayer masking of the substrate for second Au layer deposition. (**J**) Sputtering of 50 nm-thick Au film (mustard). (**K**) Revealing of the second layer of Au and sputtering of 1 nm-thick SiO_2 film (not obviously visible). (**L**) Shrinking the substrate at 130 ˚C, functionalizing the surface with MPTMS and placing a drop of EGaIn (silver) at the interface between top and bottom Au layers. **(M**) Zoom in view where the EGaIn

was sitting: i, located close to contact pad; ii, located at the center. **(N)** Casting PDMS (translucent green) onto the device. **(O)** Final transfer of the inductor onto PDMS.

The multilayer inductor fabricated on the PS was heated to 130 ˚C, inducing biaxial shrinking of the substrate. The compressive stress introduced by the shrinking PS substate created microscale wrinkles on the multilayer inductors due to the Young's modulus mismatch between the multilayer thin film and the substrate. The device shrunk to 16% of its original footprint, effectively miniaturizing the inductor (Figure 4.1L). At this stage, if the two probes of a multimeter were placed on the square contact pads to measure the device resistance, most devices showed resistances between 120-130 Ω. However, there were occasions where current would not flow. This was attributed to a lack of connectivity between the top and bottom Au layers due to the large height difference at their interface, where the thickness of the Parylene insulator (1.5 μm) was 30 times that of the top Au layer (50 nm). We anticipated that this issue with connectivity could be exacerbated if the device were stretched, where the interface would inevitably become a vulnerable spot. To solve this issue, a small drop of EGaIn was placed at the edges of the insulator layer, as indicated in Figure 4.1M-N). The liquid conductor would behave like a flexible conducting joint between the layers when the device was stretched. PDMS elastomer-crosslinker mix was then cast on top of the wrinkled device (Figure 4.1O) and cured at 70 ˚C for 4 h. Using a solvent-assisted transfer method previously reported by our group [14], the PS substrate was partially dissolved with acetone, and the device transferred onto the PDMS. Once the device was set in PDMS, the order of the layers became inverted, where the spiral Au layer now appeared at the top of the multilayer device.

4.3.2 Wrinkled inductor microstructured surface

The surface structuring of the wrinkled inductor at the interface that connects the two Au layers (Figure 4.1M-ii) was characterized through SEM imaging. Figure 4.2 shows representative SEM images of the Au/Parylene/Au and Au/Au interface for the flat inductor as fabricated on the PS substrate (panel A), after the inductor is structured via thermal shrinking (panel B), and after the structured inductor is transferred to PDMS

(panel C). These images show the evolution of the device through the fabrication process. Figure 4.2A shows the interface at the center of the spiral for the flat inductor, as indicated by the dashed square in the inset. Unsurprisingly, a clear edge can be observed since the thickness of the Parylene layer is much greater than that of the single layer of Au. At the same magnification, images of the shrunken inductors on PS and PDMS (Figure 4.2B,C) provide views of the full width of the spiral end because the shrunken devices have much smaller footprints than the flat ones. The shrunken inductor on PS exhibits wrinkles throughout the whole device (Figure 4.2B), with the wrinkles on the upper part of the image being larger than those of the bottom due to the difference in thickness of the Au/Parylene/Au versus Au/Au thin films. It is worth mentioning that shrinking the device was seen to improve the connectivity between the two Au layers, probably due to the irregular curling of the Au/Parylene film edge that leads to better electrical contact. Figure 4.2C shows the wrinkled inductor transferred onto PDMS. In this image, we observe the backside of the inductor that was fabricated on PS, where the curled edge seen in Figure 4.2B has been buried in the PDMS during the transfer process. Layers of Au/Parylene/Au, Au/Parylene, Au/Au, and Au can be identified in the image based on the wrinkle size and contrast. Given the integrity observed in the transferred films, where no breaks were seen in the wrinkled surfaces, it was reasonable to predict that PDMS would provide sufficient stability to the wrinkled inductor device to allow its operation under applied strain.

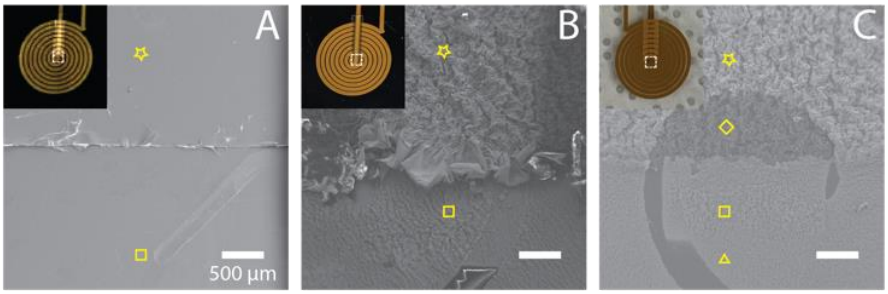

Figure 4.2. Microstructured inductor surface at the interface between Parylene/Au and Au thin films located at the center (indicated by dashed line on the insets) for (A) a flat inductor (diameter = 30 mm), **(B)** a wrinkled inductor on PS (diameter = 12 mm), and **(C)** a

wrinkled inductor after transfer onto PDMS (diameter = 12 mm). Star, rhombus, square and triangle symbols indicate layers of Au/Parylene/Au, Au/Parylene, Au/Au and Au, respectively.

4.3.3 Au/Parylene/Au thin film adhesion

Strong adhesion between a thin film and the substrate, and between the layers in multi-material thin films are essential for the long-term stability of the multilayer stretchable inductor. An adhesive tape peel test was performed to assess the strength of adhesion between the material layers for devices at different stages of fabrication. For flat inductors fabricated on PS (made at identical size as the shrunken ones), the test showed delamination, with part of the film remaining adhered to the tape (Figure 4.3A). The layer peeled off was identified as Parylene/Au, which is explained by the weak adhesion between Parylene and the flat PS substrate. On the other hand, shrunken films were found to be strongly adhered to PS and PDMS substrates, with no delamination or residues observed on the adhesive tape (Figure 4.3B,C). During the thermal shrinking process, the PS substrate and Parylene can soften and flow, while the rigid Au thin films wrinkle and buckle. The combination of these two effects can interlock the layers, resulting in enhanced adhesion, which is consistent with our previous observations [16]. In the case of the shrunken inductor on PDMS, the SiO_2 and MPTMS layers covalently bond the films to the PDMS elastomer during the curing process, promoting strong adhesion to the substrate. Overall, the interlocking of thin film layers during the thermal shrinking process and the chemical bonding due to adhesion promoters produce strong wrinkled device-substrate adhesion, resulting in stretchable devices that are resilient to delamination.

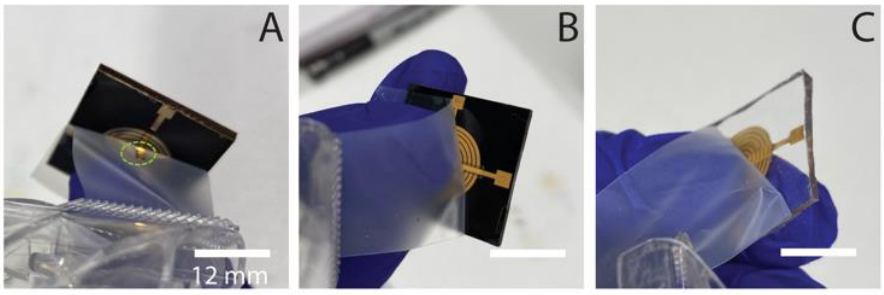

Figure 4.3. An adhesive tape peel test was performed on (A) a flat inductor on PS (green circle highlights delamination and peeled film left on tape), **(B)** a wrinkled inductor on PS, and **(C)** a wrinkled inductor on PDMS.

4.3.4 Electrical performance of wrinkled and stretchable inductors

To investigate the performance of wrinkled spiral inductors on PS and PDMS substrates, we next evaluated their electrical properties. First, we measured the resistance across different parts of the device, placing one probe on the contact pad and then moving the second probe progressively across the different turns on the device (Supplemental Information, Figure S4.1). We observed the expected behavior of increased resistance as the path along the conductor was increased for the three devices: flat inductors on PS, wrinkled inductors on PS, and wrinkled inductors on PDMS (Figure 4.4A). The resistances for the wrinkled inductors were lower than for flat ones, which is expected as the process of shrinking can connect wrinkle folds and provide additional conduction paths, effectively lowering the resistivity, as previously reported [16]. This contrasts with the typically used method of fabricating stretchable inductors using periodic wave patterns, which achieve stretchability but compromises resistance. We also found that the resistance of the wrinkled inductors on PS is identical to that of the ones transferred onto PDMS, indicating that the robustness of wrinkled films leads to stable conductive behavior. Given that low resistance is key for a high efficiency inductor, wrinkled films could provide a significant advantage for fabricating inductors for wearable devices.

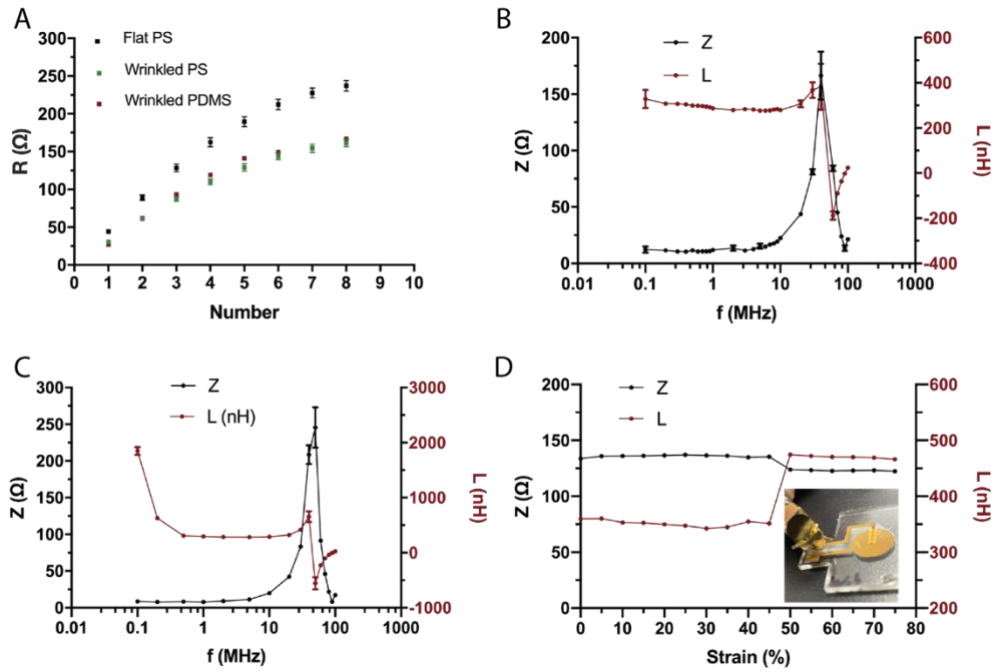

Figure 4.4. Electrical properties of wrinkled inductors. (A) Resistance along different turns of the spiral for flat inductors on shrunken PS (black squares), wrinkled inductors on PS (green squares) and wrinkled inductors on PDMS (red squares). **(B)** Impedance (black) and inductance (red) versus frequency for flat inductors on PS. **(C)** Impedance (black) and inductance (red) versus frequency for wrinkled inductors on PS. **(D)** Impedance (black) and inductance (red) of inductors on PDMS under strains of 0-75 %. Inset: Photo of stretchable inductor.

Next, we evaluated the inductance and impedance values for the fabricated spiral inductors on PS and PDMS within the frequency range of 0.1-100 MHz. As reference, we calculated the theoretical inductance for a spiral inductor [17] with the dimensions of the designed flat inductor and found it to be 340 nH (Supplementary Information, Table S4.1). The flat inductor on PS (Figure 4.4B) exhibits the expected behaviour with constant impedance at low frequencies, increased impedance at ~10 MHz, and peak impedance at a self-resonance frequency (SRF) of ~40 MHz. A corresponding constant inductance was observed between 0.1-10 MHz, with a value of ~290 nH, closely matching the theoretical calculated inductance. Wrinkled inductors on PS (Figure 4.4C) showed very similar impedance and inductance behaviour as the flat ones. The SRF of wrinkled inductors was maintained at ~40 MHZ and the constant inductance was also ~290 nH. However, the frequency range showing a constant inductance (0.4~10 MHz)

is smaller for wrinkled inductors than for flat ones. These results show that the inductance to resistance ratio increases from1.2 nH/Ω for a flat inductor to 1.8 nH/Ω for a wrinkled inductor, which is in contrast to the decrease by a factor of 3.6 reported for other stretchable inductors [10]. The higher inductance to resistance ratio also results in an increase in the peak quality factor from 1.9 to 3.4, indicating an improvement of the inductive efficiency. In the future, the quality factor of the wrinkled inductors could be optimized by increasing the thickness of the Au coil, if needed for the intended application.

Finally, we evaluated the performance of the wrinkled inductors on PDMS as tensile strain was applied from 0-75% in 5% steps (Figure 4.4D). The inductance and impedance remained constant under strains of 0-45%, and showed a jump at 50%, with the inductance increasing 34% and the impedance decreasing 8%. Two reasons that could cause the jump in inductance at 50% strain are: i) the stretching results in geometrical changes where the shrinkage in the direction parallel to the inductance is less than the expansion in the perpendicular direction, ii) the relaxation of the wrinkles leads to a more ordered response to the magnetic field, which lowers the inductance efficiency and increases the inductance. Nevertheless, after this jump, the impedance and inductance remained constant until 75% strain, at which point the PDMS substrate broke. Overall, the fabrication of stretchable inductors using multilayered wrinkled thin films is an effective strategy to obtain devices with excellent mechanical stretchability and performance.

4.4. Conclusions

A new cost-effective method for fabricating stretchable thin film inductors was introduced. The wrinkled multilayer thin film inductors were created by shrinking a pre-stressed PS substrate, and their wrinkled morphology was preserved after being transferred onto a PDMS elastomer, allowing the inductors to become stretchable. Notably, the wrinkled stretchable inductors not only show high stretchability (up to 75% strain) but also lower resistance, which resulted in a 50% increase in the inductance to resistance ratio. Such increase improves the quality factor of wrinkled inductor

compared with flat inductor, which is a distinct advantage over existing methods that provide stretchability at the expense of increasing the resistance. The strong adhesion between thin film inductors and PDMS substrate also ensures the long-term stability of devices subjected to strain.

The development of stretchable inductors, essential components for oscillator circuits and inductive power coupling, will be contribute to the integration of wireless technology to the stretchable electronics. The low cost of the fabrication method and the fact that the inductive properties depend on the geometry of the device, means that the design can be easily tailored to the targeted application by simply changing the stencil design. We believe this strategy of fabricating stretchable inductors through shrinking, and transfer will help accelerate the development of wearable and implantable electronic devices.

Acknowledgements: The authors thanks Dr. Adrian Kitai for helping to initiate the spiral inductor application. X. D. was partially supported through a China Scholarship Council doctoral award. J.M.-M. is the Tier 2 Canada Research Chair in Micro and Nanostructured Materials and the recipient of an Early Researcher Award from the Ontario Ministry of Research and Innovation. This work was supported by funding through a Discovery Grant (RGPIN-2019-06433) from Natural Sciences and Engineering Research Council of Canada and a Canadian Foundation for Innovation J.E.L.F. instrumentation grant to J. M.-M. This research made use of instrumentation within McMaster's Canadian Centre for Electron Microscopy.

References

1. Park J, Kim J, Kim S et al 2019 Soft, smart contact lenses with integrations of wireless circuits, glucose sensors, and displays Sci. Adv. 4 1-12
2. Chung H, Kim B, Lee J et al 2019 Binodal, wireless epidermal electronic systems with in-sensor analytics for neonatal intensive care Science 363 0-13
3. Kim R, Tao H, Kim T et al 2012 Materials and designs for wirelessly powered implantable light-emitting systems Small 8 2812-2818
4. Xu S, Zhang Y, Cho J et al 2013 Stretchable batteries with self-similar serpentine interconnects and integrated wireless recharging systems Nat. Commun.4 1-8
5. Park Y, Lee S, and Park J 2019 Recent progress in wireless sensors for wearable electronics Sensors 19 1-34
6. Huang X, Liu Y and Chen K et al 2014 Stretchable, wireless sensors and functional substrates for epidermal characterization of sweat Small 10 3083-3090
7. Huang Q, Dong L and Wang L 2016 LC Passive wireless sensors toward a wireless sensing platform: status, prospects, and challenges J. Microelectromechanical Syst. 25 822-841
8. Niu S, Matsuhisa N, Beker L et al 2019 A wireless body area sensor network based on stretchable passive tags Nat. Electron. 2 361-368
9. Yang S, Chen Y, Nicolini L et al 2015 "cut-and-Paste" manufacture of multiparametric epidermal sensor systems Adv. Mater. 27 6423-6430
10. Lazarus N, Meyer C, and Bedair S 2015 Stretchable inductor design IEEE Trans. Electron Devices 62 2270-2277
11. Yue C and Wong S 2000 Physical modeling of spiral inductors on silicon IEEE Trans. Electron Devices 47 560-568
12. Kim J, Park S, Nguyen T et al 2016 Highly stretchable wrinkled gold thin film wires Appl. Phys. Lett.108 061901
13. Zhu Y and Moran-Mirabal J 2016 Highly bendable and stretchable electrodes based on micro/nanostructured gold films for flexible sensors and electronics Adv. Electron. Mater. 2 1-6
14. Ding X and Moran-mirabal J 2022 Efficient multi-material structured thin film transfer to elastomers for stretchable electronic devices Micromachines 13 334
15. Golda-Cepa M, Engvall K, Hakkarainen M et al 2020 Recent progress on parylene C polymer for biomedical applications: A review Prog. Org. Coat. 140 105493
16. Gabardo C, Zhu Y, Soleymani L et al 2013 Bench-top fabrication of hierarchically structured high-surface-area electrodes Adv. Funct. Mater. 23 3030-3039
17. Wheeler H 1928 Simple inductance formulas for radio coils Proc. Inst. Radio Eng. 16 1398-1400

Appendix C: Chapter 4 supplementary information

Stretchable thin film inductors for wireless sensing in wearable electronic devices

Xiuping Ding, Ethan Shen, Yujie Zhu and Jose M. Moran-Mirabal

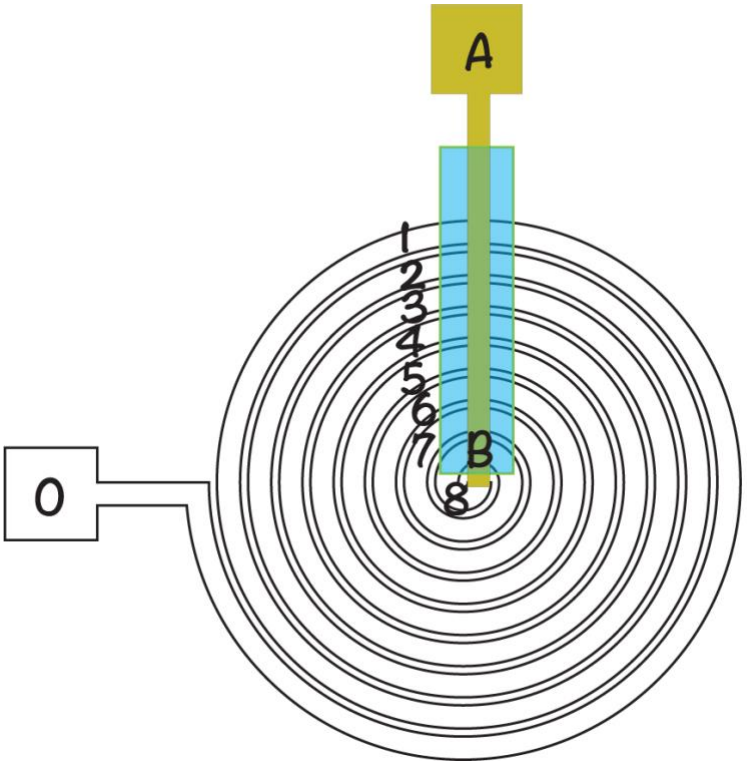

Figure S4.1. Schematic of the positions within the spiral inductor at which the resistance was measured.

Theoretical calculation of the inductance of spiral inductors

For a flat spiral air-core coil, the inductance can be calculated as [1],

$$L = 3133\,\mu_0\ \frac{r^2\,N^2}{8r + 11d}$$

where

L = inductance (nH)

$\mu_0 = 4\pi\ nH/cm$, is the vacuum permeability

r = mean radius of inductor (cm)

N= number of turns

d = the width of coil (outer radius minus inner radius) (cm)

Table S4.1. Parameters of the spiral inductor after shrinking and calculated inductance

	r (cm)	N	d	L (nH)
Trace	0.307	8	0.050	340

The theoretical calculation of the inductance with the parameters in the table:

$$L = 3313\,\mu_0 \frac{r^2 N^2}{8\,r+11\,d} = 3313 \times 4\pi \times \frac{0.307^2\,8^2}{8 \times 0.307 + 11 \times 0.050} \approx 340\ (nH)$$

References

[1] Wheeler H 1928 Simple inductance formulas for radio coils. *Proc. Inst. Radio Eng.* **16** 1398-1400

Chapter 5

Room temperature fabrication of back-contact dye-sensitized solar cells

Xiuping Ding, Jaana Vapaavuori, Jose M. Moran-Mirabal

Abstract: The integration of renewable solar energy power onto portable devices, could significantly advance the development of stretchable and wearable electronics. Specifically, dye-sensitized solar cells (DSSCs) are potentially cheap to build and can be readily tinted according to the color of dye, thus is an ideal choice of wearable self-power device. A challenge to developing stretchable DSSCs with a conventional sandwich structure, is that the electrodes must be electrically conductive and mechanically stretchable, and at least one of the electrodes must be optically transparent. This could be overcome using back-contact DSSCs, which have both electrodes on the same side of the junction and do not require the electrodes to be transparent. Another challenge in the fabrication of stretchable DSSCs is that high temperature (450 ˚C) sintering of the mesoporous TiO_2 semiconductor layer, which is a common practice for building DSSCs, is not compatible with flexible or stretchable polymer substrate and hinders continuous manufacturing. In this work, we present a method to fabricate a back-contact DSSCs containing interdigitated electrodes and a mesoporous TiO_2 layer prepared by room temperature compression. The fabrication of the interdigitated electrodes solely relied on bench-top patterning, alignment, and sputtering deposition, without need for photolithography processes. One electrode of the interdigitated array is a thin film made of layered 5 nm gold and 5 nm indium tin oxide (Au_5/ITO_5), which has the advantage of being conductive with without requiring high temperature annealing of the ITO layer. A relatively high efficiency has been achieved for the back-contact configuration DSSC with room temperature compression TiO_2 and multilayer electrode. The back-contact interdigitated DSSC showed an efficiency of 1.3 ± 0.2 %

and a fill factor of 0.52 ± 0.08, an efficiency comparable to that obtained for cells made with TiO_2 sintering. This work demonstrates a route for the fabrication of a DSSC with simplified methods that meet the needs for a continuous manufacturing process, which could the way for the development of stretchable solar cells.

Keywords: Mesoporous TiO_2, Multilayer electrode, Back-contact configuration DSSC

5.1. Introduction

The development of a flexible and stretchable self-powering system could significantly advance the implementation of wearable electronics. Harvesting solar energy is especially compelling because of the large surface area provided by the human body, which could theoretically act as a large power generator[1]. Thin film dye-sensitized solar cells (DSSCs) have been considered strong candidates for wearable self-powered systems because of the potential of producing them by large-scale roll-to-roll manufacturing[2,3]. The DSSCs are typically built by sandwiching a mesoporous semiconductor TiO_2 layer that has been dyed between two transparent conductive electrodes and injecting electrolyte after sealing. Conventionally, the colloidal TiO_2 paste is printed onto an indium tin oxide (ITO)-coated electrode and sintered at 450 ˚C to remove organic binders and solvent, producing an electrically conductive mesoporous TiO_2 network[4]. A challenge associated with translating conventional DSSC processes to the fabrication of stretchable cells is that the high temperatures needed for the sintering step are not compatible with roll-to-roll production processes and most of the materials used in flexible solar cells cannot withstand them[5]. An additional challenge is the stringent requirement for a stretchable electrode to be optically transparent, electrically conductive, and mechanically robust. The electrodes conventionally used in DSSC fabrication are made of a transparent conductive oxide film, such ITO, which are prone to cracking under strain because of their low fracture toughness. Moreover, the thermal annealing process that is needed for ITO to satisfy the conductivity requirements for solar cells is also incompatible with materials used in flexible and stretchable solar cells[6,7].

Some progress has been reported on addressing the individual issues that hinder the production of flexible DSSCs. To overcome the challenge of the high temperature annealing of TiO_2 paste, Lindström et al[8]. demonstrated a method to produce a mesoporous TiO_2 network by mechanically compressing a mixture of crystalline TiO_2 nanoparticles and ethanol at room temperature. Similarly, a back-contact layout has been developed for solar cells that eliminates the need for a transparent electrode by arranging interdigitated photo- and counter-electrodes in a co-planar fashion[9]. In this arrangement, light can impinge through a non-conductive transparent window and electron transfer happens at the back side of the solar cell. Fu et al.[10] built DSSCs with a planar interdigitated electrode configuration, demonstrating the functionality and viability of the back-contact configuration. These prior works have optimized the fabrication process and configuration of the DSSCs separately, which has laid a path for the development of the stretchable DSSCs. However, a back-contact DSSC with interdigitated electrodes and room temperature fabrication TiO_2 mesoporous layer, has never been demonstrated. In addition, at least one of the electrodes used in these works was commercially available TCO, which needs to be annealed at high temperature and has stretchability. Overcoming this challenge and the integration of all elements in a single DSSC is therefore still an outstanding task to enable the fabrication of a flexible and stretchable DSSC.

In this work, we take steps towards the realization of a process amenable to the manufacture of stretchable DSSCs by fabricating a functional back-contact DSSC that incorporates a TiO_2 mesoporous layer prepared by mechanical compression at room temperature. In this process, an array of Au_5/ITO_5 (5 nm gold layer covered by a 5 nm ITO layer) and Pt_{20} (20 nm platinum layer) interdigitated electrodes were fabricated using a low-cost approach, at room temperature, and with no annealing or photolithography involved. The fabricated DSSCs achieved an efficiency of 1.3 ± 0.2 % and fill factor of 0.52 ± 0.08, which compares favourably to DSSCs in a traditional sandwich configuration with a transparent ITO front electrode and a mesoporous TiO_2 layer prepared through annealing. This work demonstrates the possibility of building the DSSCs with processes that are amenable to the development of stretchable DSSCs.

5.2. Experimental section

Fabrication of interdigitated electrodes

The implemented DSSC design contains two interdigitating comb-shaped electrodes: one is a two-layer electrode (5 nm-thick Au/ 5 nm-thick ITO, referred to as Au_5/ITO_5) and the other is a platinum electrode (20 nm-thick Pt, referred to as Pt_{20}). ITO and Au films were deposited onto a PS substrate masked by comb-shaped stencils, which were created by cutting self-adhesive vinyl (FDC-4300, FDC graphic films, South Bend, IN, USA) with a Robo Pro CE5000-40-CRP cutter (Graphtec America Inc., Irvine, CA, USA). The Au/ITO electrode stencil was peeled off and covered by a second comb-shaped stencil for Pt deposition (see Figure S5.1 for the design and method of registration of the interdigitated electrodes). All films were deposited by sputtering using a Torr Compact Research Coater CRC-600 manual planar magnetron sputtering system (New Windsor, NY, USA). A 99.999% purity Au target (LTS Chemical Inc., Chestnut Ridge, NY, USA), ITO target (LTS Research Laboratories, Inc., Orangeburg, NY, USA), and 99.99% Pt target (LTS Research Laboratories, Inc., Orangeburg, NY, USA) were used to deposit thin films of the respective materials. Au films were sputtered using a DC (direct current) gun, and ITO and Pt films were deposited by RF (radio frequency) gun.

Photoelectrode preparation

Four types of photoelectrodes were used to assemble DSSCs (Supplementary Information Table S1): i) a photoelectrode with two layers of TiO_2 paste (18NR-T, Dyesol, Queanbeyan, NSW, Australia) and one layer of reflector paste (18RT-AO, Dyesol, Queanbeyan, NSW, Australia) screen-printed on fluorine-doped tin oxide (FTO)-coated glass, which was subjected to sintering; ii) a photoelectrode with TiO_2 paste doctor bladed onto the interdigitated electrodes, which was subjected to sintering; iii) a photoelectrode where a TiO_2 nanoparticle suspension in ethanol was doctor bladed onto a FTO electrode, which was subjected to room temperature compression; and iv) a photoelectrode where a TiO_2 suspension in ethanol was doctor bladed onto the interdigitated electrodes, which was subjected to room temperature compression. To

doctor blade the TiO_2 paste or the TiO_2 suspension in ethanol, the interdigitated electrodes on glass (12 mm × 30 mm) and FTO-coated glass (20 mm × 16 mm) were masked with an adhesive tape stencil (Magic Scotch Tape, 12 μm, 3M, London, ON, CA), which exposed a rectangular area of 5 mm × 8 mm for the TiO2 deposition. The masked electrode was then plasma cleaned by a Harrick High Power Plasma Cleaner (PDC, Harrick Plasma Inc., Ithaca, NY, USA) for 1 min at high power (30 W) and the TiO_2 was immediately deposited by doctor blading. For TiO_2 layers prepared for compression, a suspension was made by mixing TiO_2 nanopowder (Degussa p25, 99.9 %, APS: 25 nm, Nanoshell LLC., Wilmington, DE, USA) and anhydrous ethanol in a 1:5 w/w ratio. A Teflon film was placed over the cast films to prevent their removal by the press plate, and the films were compressed with a manual press machine (Carver laboratory press, model C, Fred S. Carver Inc, Menomonee falls, Wis, USA) at 1000 psi. The TiO_2 paste (DSL 18NR-T, Dyesol, Queanbeyan, NSW, Australia) was directly doctor bladed onto the electrodes, which were then put into an oven. The temperature in the oven was ramped up to 450 ˚C and the samples were kept at 450 ˚C for 30 mins. After the thermal treatment was done, the samples were left to cool down for 2 hours. The four types of photoelectrodes were finally sensitized for 24 hours with a 0.5 mM ruthenium dye solution (*cis*-bis (isothiocyanato) bis (2,2-bipyridyl-4,4-dicarboxylato) ruthenium (II) bis-tetrabutylammonium, N719 standard Dye, Solaronix, Aubonne, Switherland). Excess dye was then rinsed with ethanol.

The morphology of the TiO_2 mesoporous films was characterized by scanning electron microscopy (SEM) (JSM-7000F, JEOL Ltd., Tokyo, Japan) with a 3.0 kV acceleration voltage.

Counter electrode preparation for DSSCs with sandwich configuration

The counter electrode used for DSSCs with a sandwich configuration was an FTO-coated glass with two electrolyte access holes, which was platinized with 4 μl of 5 mM chloroplatinic acid (H_2PtCl_6, Sigma Aldrich, St. Louis, MO, USA) in isopropanol and heated at 390 ℃ for 15 min.

Assembly of DSSCs with sandwich and back-contact configurations

The DSSCs with sandwich configuration were constructed using FTO-coated glass for both photo- and counter-electrodes, while back-contact configuration DSSCs were made using interdigitated photo- and counter-electrodes on the same glass substrate. The cell cavity was defined using a 25 μm-thick resin spacer (Surlyn 1702, DuPont, Wilmington, Germany) bonded at 110˚C. For ease of measurement, copper tape was attached to the photo- and counter-electrodes. Fast drying silver paint (Ag in iso-butyl methyl ketone, Ted Pella Inc., Redding, CA, USA) was painted over the interface of copper tape and the electrodes to improve the contact.

DSSC Characterizations

Immediately before testing the cells, they were filled with 5 μl of electrolyte (EL-HSE, Dyesol, Queanbeyan, NSW, Australia) through one of the holes on the counter electrode (sandwich configuration) or on the glass cover (back-contact configuration). The DSSCs were illuminated with a lamp (4711496, Airam, Kerava, Finland) calibrated to simulate AM 1.5 sunlight. I-V curves were measured from the solar cells using a source meter (2450 Source Meter, Keithley, Tektronix Inc., Solon, OH, USA).

5.3. Results and Discussion

DSSC fabrication

As a first step towards the realization of flexible and stretchable solar cell devices, the DSSCs in this work adapted room temperature fabrication processes and a co-planar configuration. Two improvements were made to accommodate the lower tolerance of flexible materials to high temperatures and to overcome the requirement for the photoelectrode to be transparent. Figure 5.1 shows the schematic of the back-contact DSSC configuration (fabrication details are provided in Supplementary Information, Figure S5.2). From bottom to top, the exploded view reveals the components of a back-contact DSSC (Figure 5.1A). Interdigitated Au_5/ITO_5 and Pt_{20} electrodes (photo- and counter-electrodes, respectively) were patterned on a glass substrate and a mesoporous layer of TiO_2 was doctor bladed and compressed at room temperature. The fact that the two electrodes are in a co-planar configuration not only allows the electrode materials

to be opaque, but also greatly aids in the integration of auxiliary wiring and interconnections to other thin film electronic circuits. A considerable amount of dye could be directly bound to the surface of the TiO_2 because of the large surface area provided by the mesoporous layer. In this design, the Surlyn resin spacer works both as a gasket to create a space for the liquid electrolyte and as adhesive to seal the cell. Copper tape was used as an external contact to facilitate the electrical measurements. With the two conductive electrodes both located at the back substrate, the function of the top window, was reduced to sealing the cell and efficiently allowing light to reach the TiO_2 layer, which could be easily fulfilled by glass or a variety of transparent plastics and elastomers.

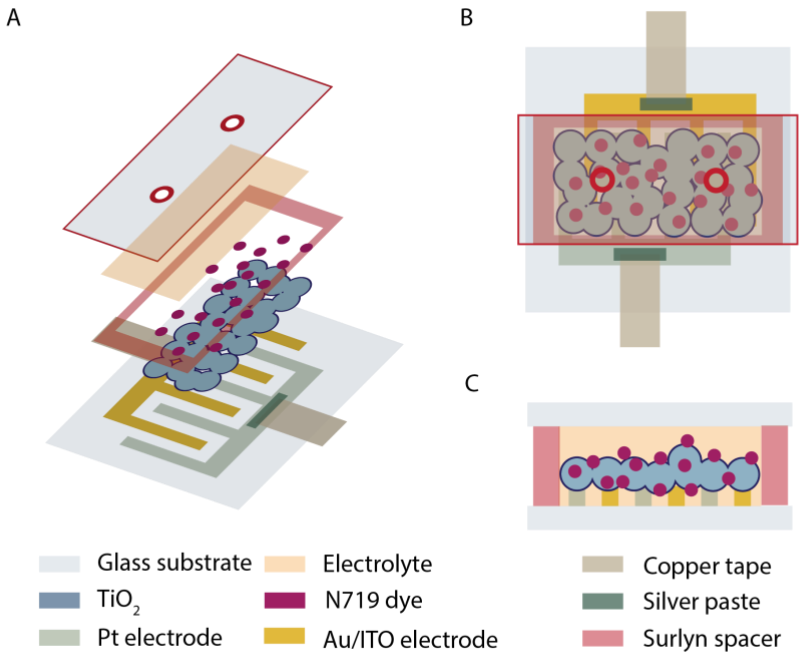

Figure 5.1. Schematic device configuration of interdigitated DSSC fabricated with room temperature compression. (**A**) Exploded view. (**B**) Top view. (**C**) Cross-sectional view. Elements are not drawn to scale.

When measurements were conducted, the DSSC was illuminated from the top (Figure 5.1B). The cross-sectional view illustrates the critical contact between the electrodes, the porous TiO_2 semiconductor, the dye, and the electrolyte. The principle

of operation of the device involves the dye adsorbed on the surface of the mesoporous layer absorbing photons and injecting electrons into the conduction band of the TiO_2 semiconductor. The photoelectrons are then collected by the working electrode (Au/ITO), and electrons from the electrolyte, which works as a mediator and contains the iodide/triiodide redox couple, restore the dye. The triiodide is also efficiently reduced to iodide at the Pt counter electrode. To enable the diffusion of electrons, it is critical that the TiO_2 layer forms a conductive network. This can be accomplished by either thermally annealing or mechanically compressing the layers, as done in this work (Supplementary Information, Figure S5.3). Theoretical models have reported that the maximum diffusion length of electrons is 100 μm[11], which suggests that the spacing between photo- and counter-electrodes should be smaller than this length. However, the resolution of the cutter used to pattern the interdigitated electrode stencils limited the spacing in our devices to 200 μm. Despite this limitation, the fabricated DSSCs were functional and had reasonable efficiencies, which could open the discussion of the maximum diffusion length of electrons.

The effectiveness of the mechanical compression process to form a conductive TiO_2 network, can be partially assessed by comparing the morphology observed by SEM of thermally annealed and mechanically compressed layers. The TiO_2 layers deposited by screen-printing or doctor blading and sintered at 450 ˚C (Figure 5.2A-B) show a compact porous structure that is conductive (no charge accumulation observed). Although the TiO_2 layer deposited by doctor blading is smoother compared to the one deposited by screen-printing, both films are uniform and tightly packed. In contrast, the film obtained by doctor blading a nanocrystalline TiO_2 suspension (Figure 5.2C) is loosely packed and presents very high roughness. The TiO_2 nanoparticles in this film are less evenly distributed and more distinguishable than in the annealed films. However, the morphology of the TiO_2 layers deposited from suspensions after mechanical compression (Figure 5.2D) is comparable to the annealed films.

Key advantages of mechanically compressing the TiO_2 layer at room temperature (after optimization of surface treatments and electrode layer thickness, Supplementary Information, Figures S5.4 and S5.5) over high temperature annealing, are that the

process is energy and time efficient and is compatible with materials that can be used to build flexible and stretchable DSSCs.

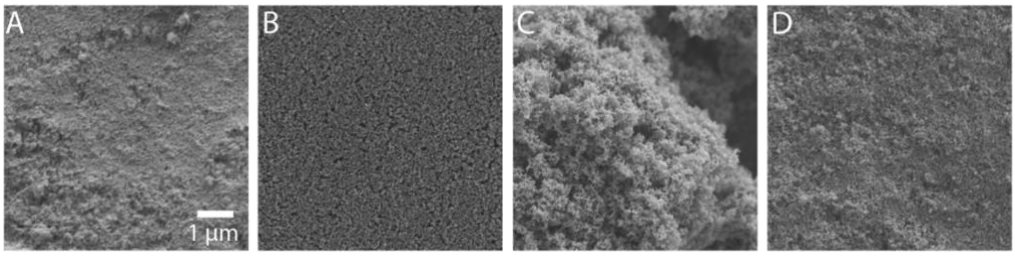

Figure 5.2. Microstructure of mesoporous TiO_2 layers observed through SEM. (**A**) Commercially available TiO_2 layer deposited by screen-printing and thermally annealed. (**B**) Commercially available TiO_2 paste deposited by doctor blading and thermally annealed. (**C**) TiO_2 layer deposited from nanoparticle suspension by doctor blading with no additional treatment. (**D**) Film from panel (C) after mechanical compression at 1000 psi.

DSSC Performance

The photovoltaic properties of the four types of DSSCs fabricated were characterized by I-V measurements, and the results are summarized in Table 5.1 and plotted in Figure 5.3. The sandwich DSSCs that were thermally annealed showed efficiencies that are comparable to those previously reported in the literature[3]. When the TiO_2 layers were mechanically compressed, the efficiency of the DSSCs with sandwich configuration dropped by 47%, which was attributed to less efficient electron transport to the photoelectrode. In contrast, the back-contact DSSCs with interdigitated electrode configuration showed similar efficiencies for annealed and compressed layers. The efficiency of these devices was on average 1.3-1.4%, where the reduction in efficiency was attributed to a lower short circuit current density arising from the interdigitated design and the large spacing between electrodes. Nevertheless, the efficiencies obtained are promising in view of the simplicity of the fabrication approach and could be further optimized in future studies. Compared to previously reported back-contact DSSCs[10], which have achieved maximum efficiencies of 4.2%, our method is simple as it does not use photolithography (results in larger spacing between working and counter electrodes), does not require annealing of TiO_2 or deposition of ZrO_2 as an insulation layer, and does not use a commercial ITO electrode (replaced by Au_5/ITO_5). The

spacing between two electrodes is about 200 µm, which is way beyond the maximum electron diffusion length of 100 µm reported by L. M. Peter[11].

The fabrication approach developed is therefore compatible with materials used to make flexible and stretchable electronics, which could aid in the future development of stretchable solar cells.

Table 5.1. Photovoltaic performance of DSSCs with two configurations and two TiO_2 layer fabrication methods. Sandwich structure/annealing, back-contact structure/annealing, sandwich structure/compression, back-contact/compression. Measurements done under 100% simulated sunlight (AM 1.5, 1000 W/cm^{-2}). J_{sc}, V_{oc}, FF, and η refer to short-circuit current density, open-circuit voltage, fill factor, and efficiency, respectively.

Structure	Materials	J_{sc} (mA/cm²)	V_{oc} (mV)	FF	η (%)
Sandwich	Annealing	17.2 ± 1.9	736 ± 22	0.52 ± 0.01	6.6 ± 0.9
Interdigitated	Annealing	4.2 ± 1.2	627 ± 31	0.55 ± 0.07	1.4 ± 0.3
Sandwich	Compression	7.2 ± 2.0	797 ± 42	0.63 ± 0.10	3.5 ± 0.5
Interdigitated	Compression	3.2 ± 1.0	785 ± 42	0.52 ± 0.08	1.3 ± 0.2

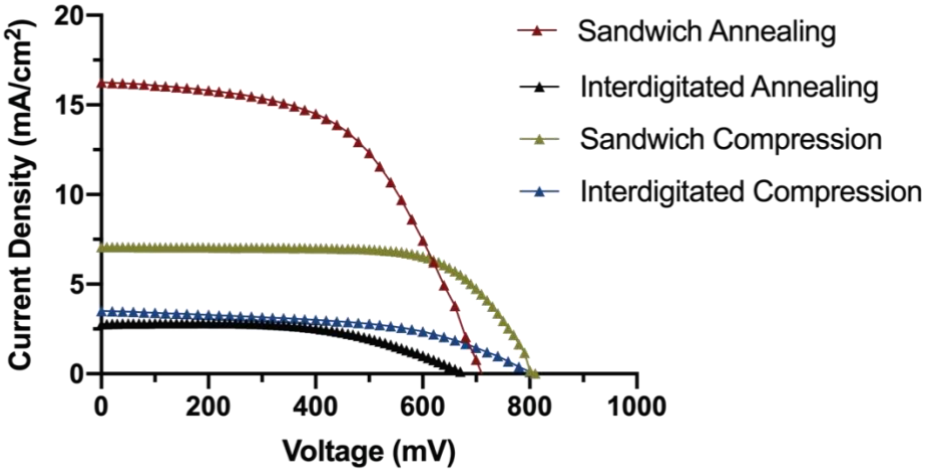

Figure 5.3. Current-voltage characteristic of fabricated DSSCs.

5.4. Conclusions

The possibility of building a back-contact DSSC with an interdigitated electrode by room temperature compression of TiO_2 has been demonstrated in this work. The similar efficiency of back-contact DSSC made with room temperature compression of the TiO_2 layer and with conventional high temperature annealing shows that the room temperature process effectively forms an electrically conductive TiO_2 network. Both of back-contact configuration and mechanical compression fabrication are more in line with roll-to-roll manufacturing and compatible with materials used for the fabrication of flexible and stretchable electronics.

References

1. Hammock, M. L.; Chortos, A.; Tee, B. C. K.; Tok, J. B. H. & Bao, Z. 25th anniversary article: The evolution of electronic skin (E-Skin): A brief history, design considerations, and recent progress. *Adv. Mater.* **2013**, *25*, 5997-6038.
2. Grätzel, M. Dye-sensitized solar cells. *J. Photochem. Photobiol. C Photochem. Rev.* **2003**, *4*, 145–153.
3. Grätzel, M. Photoelectrochemical Cells. *Materials For Sustainable Energy: A Collection of Peer-Reviewed Research and Review Articles from Nature Publishing Group.* **2011**. *414*, 338-344.
4. Grätzel, M. & O'Regan B. A low-cost, high-efficiency solar cell based on dye-sensitized colloidal TiO_2 films. *Nature* **1991**, *353*, 737-739.
5. Lewis, B. G. & Paine, D. C. Applications and processing of transparent conducting oxides. *MRS Bull.* **2011**, *25*, 22-27.
6. Haines, W. G. & Bube, R. H. Effects of heat treatment on the optical and electrical properties of indium-tin oxide films. *J. Appl. Phys.* **1978**, *49*, 304-307.
7. Oh, S. J., Kwon, J. H., Lee, S., Choi, K. C. & Kim, T. S. Unveiling the annealing-dependent mechanical properties of freestanding indium tin oxide thin films. *ACS Appl. Mater. Interfaces* **2021**, *13*, 16650-16659.
8. Lindström, H., Holmberg, A., Magnusson, E., Malmqvist, L. & Hagfeldt, A. A new method to make dye-sensitized nanocrystalline solar cells at room temperature. *J. Photochem. Photobiol. A Chem.* **2001**, *145*, 107-112.
9. Kerschaver, E. V. & Beaucarne, G. Back-contact solar cells: A review. *Prog. Photovoltaics Res. Appl.* **2006**, *14*, 107-123.
10. Fu, D., Zhang, X., Barber, R. L. & Bach, U. Dye-sensitized back-contact solar cells. *Adv. Mater.* **2010**, *22*, 4270-4274.
11. Peter, L. M. Characterization and modeling of dye-sensitized solar cells. *J. Phys. Chem. C* **2007**, *111*, 6601-6612.

Appendix D: Chapter 5 supplementary information

Stretchable thin film inductors for wireless sensing in wearable electronic devices

Xiuping Ding, Jaana Vapaavuori , Jose M. Moran-Mirabal

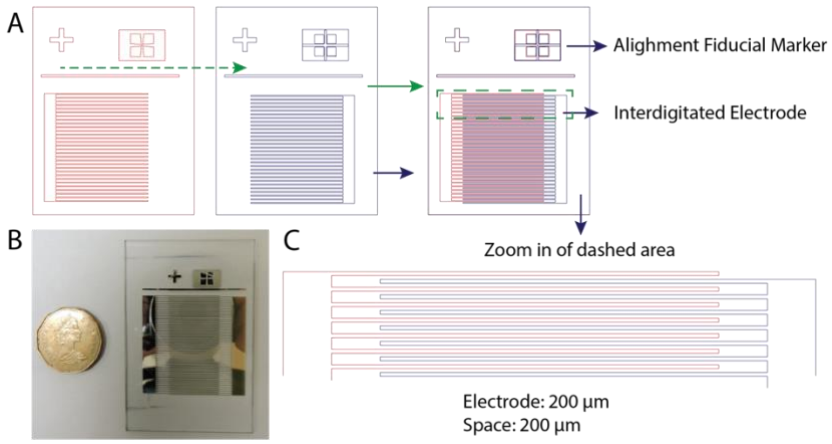

Figure S5.1. Interdigitated electrode design. (A) Design and alignment scheme for the interdigitated electrodes. (B) Digital photo of the fabricated electrode. (C) Zoom in of the dashed square area in (A).

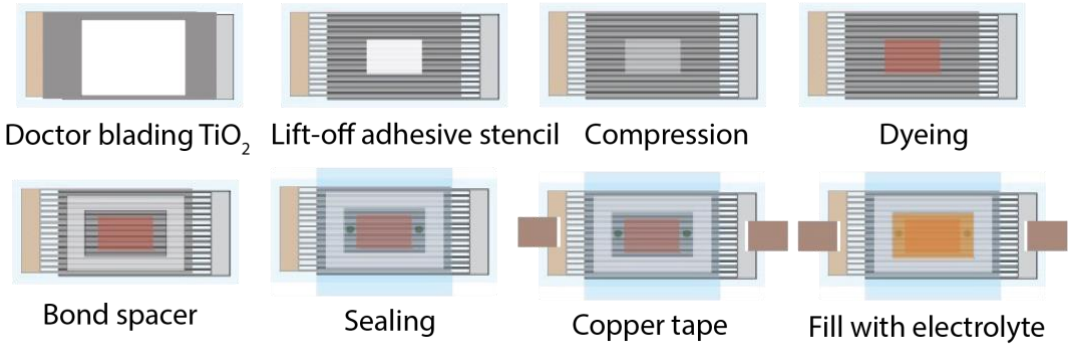

Figure S5.2. Schematic of back-contact DSSC fabrication

Table S5.1 Four types of DSSCs made by combining TiO_2 treatment, electrode type, and solar cell configuration

Structure	TiO_2	Electrode
Sandwich	Annealing	FTO
Back-contact	Annealing	Interdigitated
Sandwich	Compression	FTO
Back-contact	Compression	Interdigitated

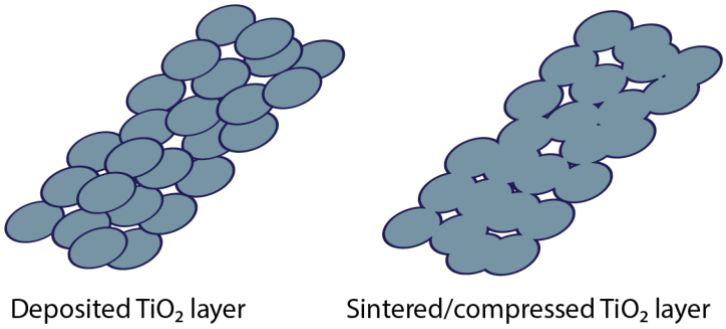

Figure S5.3. Schematic comparison between as deposit TiO_2 film and sintered/compressed TiO_2 (conduction network)

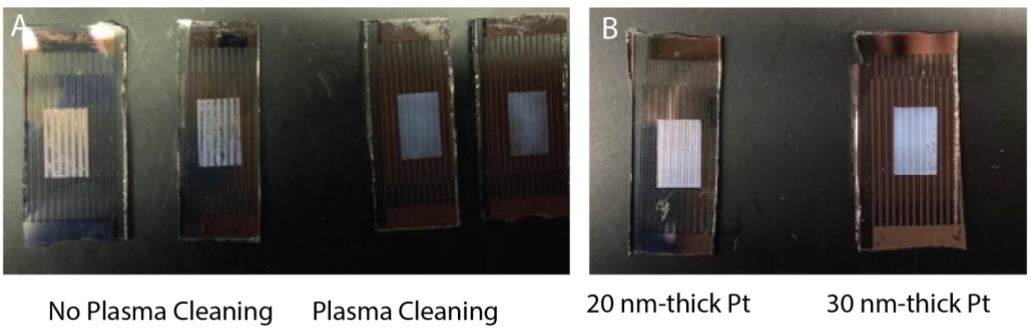

Figure S5.4. The effect of plasma treatment and Pt thickness on the quality of the TiO_2 mesoporous layer. (A) Plasma treatment is necessary to generate uniform TiO_2 layers. (B) The thickness of Pt does not impact the quality of the TiO_2 layer.

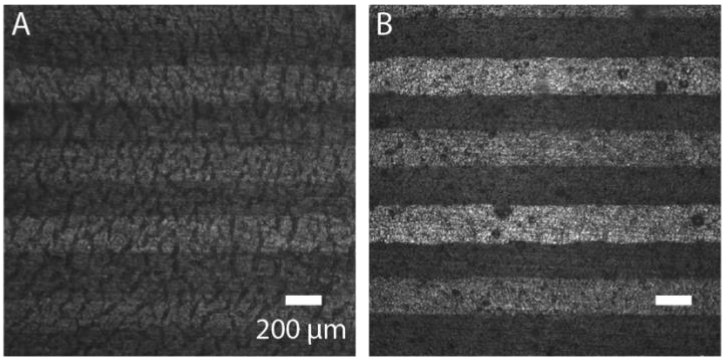

Figure S5.5. The optical microscopy images of the morphology of the layer of TiO_2 shows the impact of the different treatments.

Table S5.2. Photovoltaic performance of DSSCs with two configurations and two fabrication methods: sandwich configuration/annealing, interdigitated back-contact configuration/annealing, sandwich configuration/compression, interdigitated back-contact configuration/compression under 100 % simulated sunlight (AM 1.5, 1000 W/cm^{-2}). J_{sc}, V_{oc}, FF, and η refer to short-circuit current density, open-circuit voltage, fill factor, and efficiency, respectively.

Structure	Materials	J_{sc} (mA/cm^2)	V_{oc} (mV)	FF	η (%)
Sandwich	Annealing	17.2 ± 1.9	736 ± 22	0.52 ± 0.01	6.6 ± 0.9
Interdigitated	Annealing	3.4 ± 0.9	552 ± 11	0.33 ± 0.12	0.6 ± 0.1
Sandwich	Compression	7.2 ± 2.0	797 ± 42	0.63 ± 0.10	3.5 ± 0.5
Interdigitated	Compression	1.1 ± 0.3	553 ± 52	0.34 ± 0.08	0.3 ± 0.0

Chapter 6
Conclusions

This work demonstrates an efficient and bench-top method to fabricate stretchable electronics by wrinkling the thin film and transferring the wrinkled films onto PDMS elastomer, which is the foundation of the thesis. Using this method, a stretchable thin films heater, a corrosion resistant stretchable multilayer electrode and a stretchable spiral inductor were fabricated and characterized, showing high mechanical stretchability while maintaining high level of performance. A DSSC was also built at room temperature by mechanically compressing the mesoporous TiO_2 semiconducting layer to prepare for further stretchable DSSCs development.

The key contributions of this thesis are:

(1) A strategy of fabricating stretchable thin film electronics. The method begins with the fabrication of structured thin films by shrinking thin films deposited onto pre-stressed PS sheets, then involves with modification of the thin films with adhesion promoter (such as, MPTMS (a self-assembled monolayers), SiO_2, plasma treatment) to form chemical bonding with the receiving substrate of PDMS and finishes with transfer the structured films with two solvent-assisted approaches. One approach is using sacrificial layer, the transfer is simpler with only one-time solvent dissolution of the sacrificial layer, but the wrinkles are larger owing to the present of sacrificial layer; the other approach is transferring without sacrificial layer, which required additional rinsing

step, but the wrinkled feature is smaller. They can reliably transfer complex patterns of materials, and different architectures with varied dimensions. The ability to transfer complex multi-material composites can open the door to applications that require stretchable electrodes, dielectric, and semiconductor components. It can also solve interconnect problems, which are one of the key challenges for wearable electronic devices and arrays.

(2) Thin film stretchable heaters. A proof-of-concept application was demonstrated by fabricating and characterizing stretchable thin film Au and ITO/Au/ITO multilayer stretchable heaters. The film heaters display fast thermal response (linearly temperature increases within first 60s), high reproducibility (stable performance with at least 10 on-off cycles), and high stretchability (stable temperature performance at least within 75 % strain).

(3) Corrosion-resistance stretchable multilayer electrode. Based on a multilayer concept of building conductive electrode, ITO and Parylene were introduced and tested as a passivation layer to protect the thin film metal from being corroded while still maintaining a high level of conductivity of the film. By optimizing films thickness and processed approaches, we reached to the conclusion that a stretchable film that made of 200-nm thick wrinkle Au transferred on PDMS and coated with 100-thick Parylene is the ideal candidate. The electrodes display high stretchability and excellent corrosion resistance.

(4) Stretchable thin film inductors. A thin film stretchable inductor mainly consisting of 50-nm thick Au and 1.5 μm Parylene was fabricated. The wrinkled stretchable inductors not only show high stretchability (up to 75% strain) but also lower resistance, which resulted in an increase in the inductance to resistance ratio. Such increase improves the quality factor of wrinkled inductor compared with flat inductor, which is a distinct advantage over existing methods that provide stretchability at the expense of increasing the resistance. The strong adhesion between thin film inductors and PDMS substrate also ensures the long-term stability of devices subjected to strain.

(5) Room temperature fabrication of back-contact dye-sensitized solar cells. The dye-sensitized solar cells were fabricated by preparing the mesoporous TiO_2 film with mechanical compression at room temperature on an interdigitated electrode. The fabrication of the interdigitated electrodes solely relied on bench-top patterning, alignment, and sputtering deposition, without need for photolithography processes. The back-contact interdigitated DSSC showed an efficiency of 1.3 ± 0.2 %, which is comparable to that obtained for cells made with TiO_2 sintering. This work demonstrates a route for the fabrication of a DSSC with simplified methods that meet the needs for a continuous manufacturing process, which could be the way for the development of stretchable solar cells.

Overall, the work presented in this thesis demonstrates an efficient approach of fabricating stretchable electronics that will be contributing the development and

integration of electronics with human body for applications such as advanced diagnostic and therapeutic treatment, health monitoring and brain-machine research.